Depth inversion based on Argus images and accounting for nonlinearities

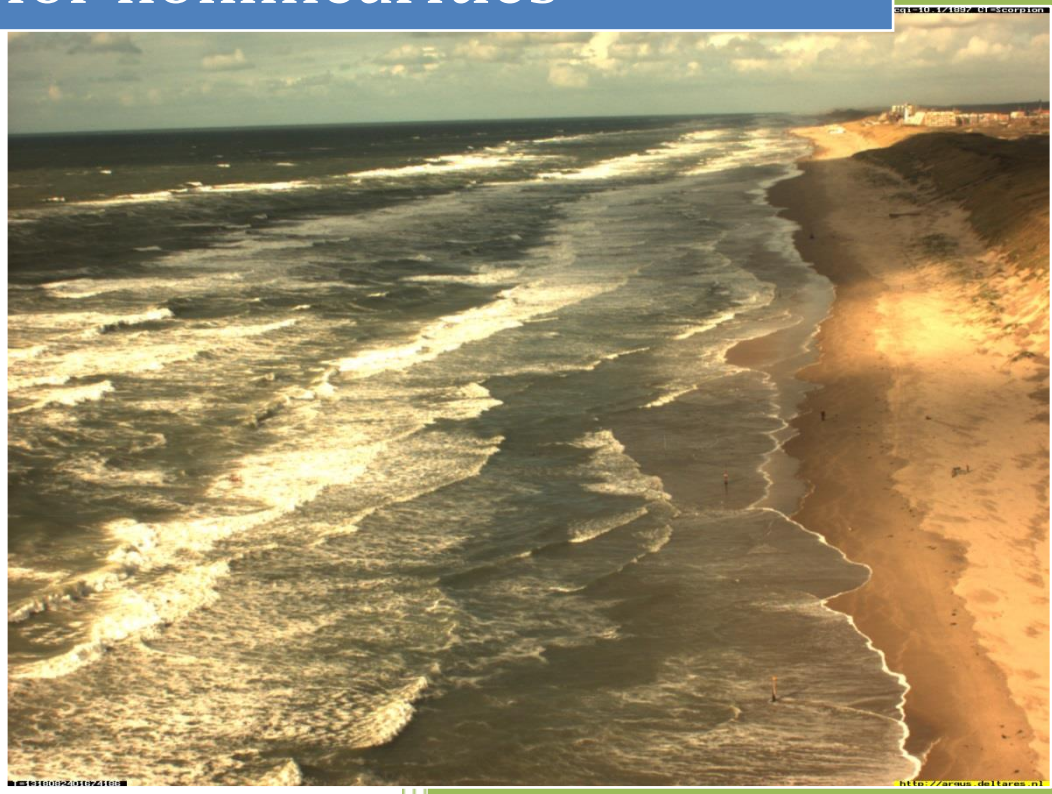

Dimitrios Chatzistratis [3869245]
MSc Thesis
1st Supervisor: Gerben Ruessink
2nd Supervisor: Marion Tissier
Staff Member involved: Jantien Rutten

Department of Physical Geography
Faculty of Geosciences
Utrecht University

Acknowledgements:
I would like to thank my supervisor Marion Tissier for all her support and comments during my thesis. I would like to greatly thank Jantien Rutten for all the constructive feedback concerning my research and to my professor Gerben Ruessink for allowing me to work relatively independently.
Big thank also to Joost Brinkkemper for providing with all the Egmond field data of the 2011 fieldwork.
Furthermore, I would like to thank Rob Holman for sharing his knowledge about cBathy.
Moreover, I would like to thank all the students at Utrecht University that we shared time with during these months. Lastly, all my friends and relatives back in Greece and especially my parents for their endless support.

1. Introduction

Determination of bathymetry in coastal areas is both of societal and scientific interest. Due to the increasing population dwelling near coastal areas, knowledge of temporal bathymetric changes is essential for taking Coastal Zone Management decisions. In addition, navigation and amphibious operations near beaches require extend knowledge of water depth. Commercial entities such as oil companies also rely on bathymetric data. Scientifically, nearshore topography forms the boundary condition for all fluid motions and determines the evolution of wave field. In wave modeling and current prediction, results are often very sensitive to the details of the water depth, and thus, up-to-date, accurate bathymetry constitutes an important boundary condition.

There is a strong and continuous feedback between hydrodynamics and morphodynamics in the nearshore zone. Decreasing depths cause wave to be asymmetric and break while bottom topography is heavily determined by sediment transport during the overlying wave motions. During storms, waves are breaking on sandbar crests driving an offshore current (undertow) which causes erosion on the onshore part of the bar and offshore bar migration. During quiescent periods, waves break further onshore and hence accretion and onshore migration of sandbars occur (*Hoefel & Elgar*, 2003).

Traditionally, bathymetric data are collected with in situ measuring techniques. GPS-equipped Jet Ski or bottom-contacting vehicles such as the CRAB (*Birkemeier et al*, 1984) have eliminated vertical errors in estimation producing quite accurate bathymetry (*Stockdon & Holman, 2000)*. Nevertheless, due to the fact that bathymetric changes must be captured efficiently both in spatial and temporal scales, in situ methods remain expensive and logistically difficult to be applied. Furthermore, the appliance and accuracy of such techniques is limited significantly during the most energetic conditions. However, such conditions cause rapid changes, being thus of the greatest scientific interest.

An alternative to in situ measurements are remote sensing techniques applied at coastal areas. The Argus monitoring system developed by the Oregon State University and consisting of shore-based camera stations is a good example of such techniques (*Holman & Stanley*, 2007). Methods based on video imagery have been developed in order to acquire values of bathymetric features through signals of depth induced variations of wave characteristics on the sea surface such as the wave celerity (*Stockdon & Holman*, 2000) or the dissipation of the wave breaking (*van Dongeren etal,* 2008). Thus, the monitoring of the coastline can provide with a continuous streaming of bathymetric data in high temporal and spatial resolution, appropriate to resolve rip currents.

One approach to bathymetry estimation is based on the dependence of wave kinematics on water depth. As waves propagate into shallower regions they are shortened, while for a certain depth longer waves travel faster. Wave celerity c, or equivalently wavenumber k, can be firstly estimated and then associated with local depth via the inversion of a dispersion relationship. Wave celerity is a continuous characteristic which enables bathymetry estimation ceaselessly in spatial and temporal scale, oppositely to wave dissipation patterns. Accurate prediction of wave parameters and establishment of an appropriate functional relationship with water depth is fundamental for the accuracy of the final estimation.

Recently, *Holman etal* (2013), following the increased interest for the depth inversion techniques, developed a new robust algorithm, cBathy, which takes raw video images as input data and is designed to anticipate efficiently noisy image data due to certain weather and wave conditions through the implementation of a Kalman

filter. The algorithm was found capable to produce reliable estimation of bathymetry for a 2-D region using the easily invertible linear dispersion relationship for the final depth solution, similarly to the majority of depth inversion methods.

However, inside a highly nonlinear environment such as the surf zone where waves are breaking they may propagate faster than linear wave theory predicts. Not modelling amplitude effects in the dispersion relationship has been found to lead to depth overprediction in depth inversion studies (*Holland*, 2001)

The objective of this research study is therefore two-fold: Firstly, it aims in the extraction of an accurate bathymetry in the Argus site of Coast 3D Tower in the Dutch coast of Egmond aan Zee using the cBathy algorithm. Secondly, it aims in the improvement of the depth inversion solution through the implementation of a wave celerity model accounting for nonlinearities in the surf zone.

The structure of the report is as follows: In Section 2, background information from the available literature is reviewed relevant to 1) wave celerity and existing phase speed models and 2) the main principles of cBathy. In the end of Section 2, the research questions are defined. In Section 3 the methodology steps followed in the present research are described, including a description of the study area and the available field data. In Section 4 the results of the research are presented followed by the discussion and recommendations in Section 5. The report ends up with the conclusions.

2. Background literature

2.1. Wave celerity

In a propagating wave, the wavelength L is defined as the horizontal distance between two successive crests and the wave period T as the time taken for the passage of two such points. The wave frequency is defined as $1/T$ and expressed in Hz (or s^{-1}) .
The wave phase speed, or wave celerity, c, is defined as the wavelength divided by the wave period:

$$c = \frac{L}{T} \qquad (2.1)$$

Equivalently, because $L = \frac{2\pi}{k}$ and, $T = \frac{2\pi}{\sigma}$ where k = wavenumber and σ = angular frequency, equation (2.1) can also be written as:

$$c = \frac{\sigma}{k} \qquad (2.2)$$

2.1.1. Linear wave theory

2.1.1.1. Basic principles of linear wave theory

The simplest water wave theory is that of linear waves, which emerges as a simplified solution to the general equations of motion for periodic waves with period T propagating in constant depth. Linear theory is based on the assumptions that the wave height H is small relatively to wave length and water depth h, meaning $H/L<<1$ and $H/h<<1$ respectively. Furthermore, the waves described by linear theory are assumed to propagate independently and not affect one another. Linear wave theory relates the wavenumber and frequency through the dispersion equation:

$$\sigma^2 = gktanh(kh) \qquad (2.3)$$

$$L = \frac{gT^2}{2\pi} tanh(\frac{2\pi h}{L}) \qquad (2.4)$$

where g is the acceleration of gravity and h is the local water depth. Combining (2.2) and (2.3) the wave celerity based on linear theory is given by:

$$c = \sqrt{\frac{g}{k} tanh(kh)} \qquad (2.5)$$

Approximations to the exact solution exist for waves propagating in deep and shallow water. In deep water, where $h/L>0.5$, we can make the approximation $tanh(kh)\sim 1$. Thus a simple deep wavelength L_o can be defined:

$$L_o = \frac{gT^2}{2\pi} \qquad (2.6)$$

Combining (2.5), (2.6) and $k=2\pi/L$, the phase speed becomes:

$$c = \frac{g}{c} = \frac{gT}{2\pi} \qquad (2.7)$$

The dispersion relationship expresses the functional relationship between the wave frequency, the wave length and the gravity acceleration. It indicates that waves in deep water are frequency dispersive, meaning that waves of different frequencies travel with different phase speed. By the frequency dispersion mechanism groups of waves slowly disintegrate over longer distances. Waves generated during a storm travel long distances towards coasts, transforming into regular swell waves characterised by a narrow energy spectrum.

In shallow water ($\frac{h}{L}$<0.05), *tanh(kh)* ~ *kh* and (2.5) simplifies to:

$$c = \sqrt{gh} \qquad (2.8)$$

which shows that wave speed is solely a function of the local depth, indicating that waves in shallow water are not frequency dispersive.
In presence of a current, the dispersion relation is defined as:

$$\sigma = \sqrt{gktanh(kh)} + \boldsymbol{u} * k \qquad (2.9)$$

with $\boldsymbol{u}$ the mean current vector.

2.1.1.2. Comparison with field data

Dugan et al (2001) used the dispersion relationship (2.9) for the retrieval of depth and current magnitude in a field study near Duck on the North Carolina Outer Banks. They used radiance data of temporal sequences of shoaling waves, acquired from an aircraft's digital framing camera.

The results were compared with in situ measurements for depths between 4-12 m having errors between 5-13% for bathymetry and less than 5% for the currents, indicating that linear theory is sufficiently accurate for intermediate water depths.

In spite of the sufficiency of linear theory in deep and intermediate depths, there are deviations from it in shallow water. A field study about wave celerity was conducted by *Thornton & Guza* (1982) in a beach near San Diego. Measurements were done using 11 current meters in a shore normal transect with the most offshore sensor location at 7 m depth, examining the cross shore profile of wave speed. Celerity spectra were calculated by using pairs of adjacent sensors. The phase difference between two measurement points with distance *Δx* equals to:

$$\varphi(\sigma) = k_x \Delta x \qquad (2.10)$$

With $k_x = k\cos(\theta)$ the x component of wave number and θ is the mean angle of wave incidence at angular frequency σ.

Wave velocity in the *x*-direction is given by:

$$c_x = \sigma / k_x \qquad (2.11)$$

Thus, combining equations (2.10) and (2.11), wave celerity was computed as:

$$c_x = \frac{\sigma \, \Delta x}{\varphi(\sigma)} \qquad (2.12)$$

Each velocity spectrum represented 34.1 minutes of data with a spectral resolution of 0.014 Hz. The theoretical value of celerity spectrum was also calculated for each sub-transect based on linear theory and using the mean depth between sensors as input value.

Observed and predicted celerity spectra were well comparable at the deepest locations (Figure 1, upper panel). The only exception was the windiest day, when waves obtained the largest amplitude during the fieldwork and were broad frequency band waves, starting to differ from predictions more offshore than the other days.

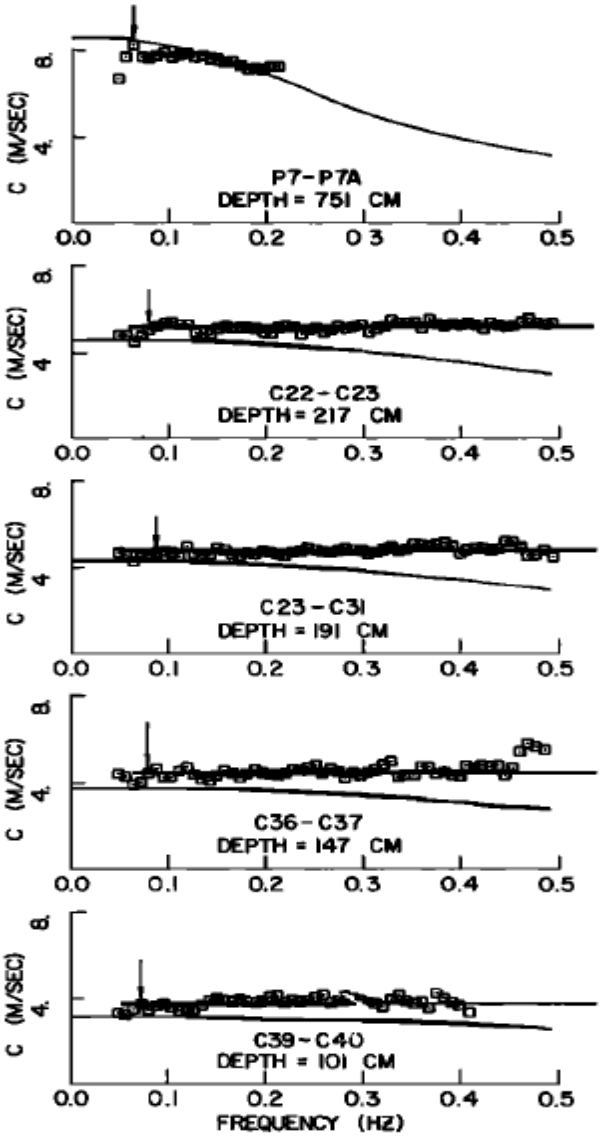

Figure 1. Celerity spectra for moderate, very narrow – band waves on November 20, 1978 (after *Thornton & Guza*, (1982))

However, as approaching the shallower regions where nonlinearities were pronounced, the observed spectra started to deviate from the theoretical predictions (Figure 1, four lower panels). Linear theory predicted celerity to decrease with increasing frequency even in 1-m depths, as high frequency waves did not feel the sea bottom and remained frequency dispersive. On the other hand, the observed phase speed remained constant all over the spectra in shallow water, indicating clearly a nondispersive behavior. Measured phase speeds were essentially higher than the theoretical predictions

Overall, predictions of linear theory were compared with the field measurements (Figure 2) and found to overpredict celerity about 10% for small values of the relative wave height (H_{rms}/h~0.4) that correspond to the inner surf zone.

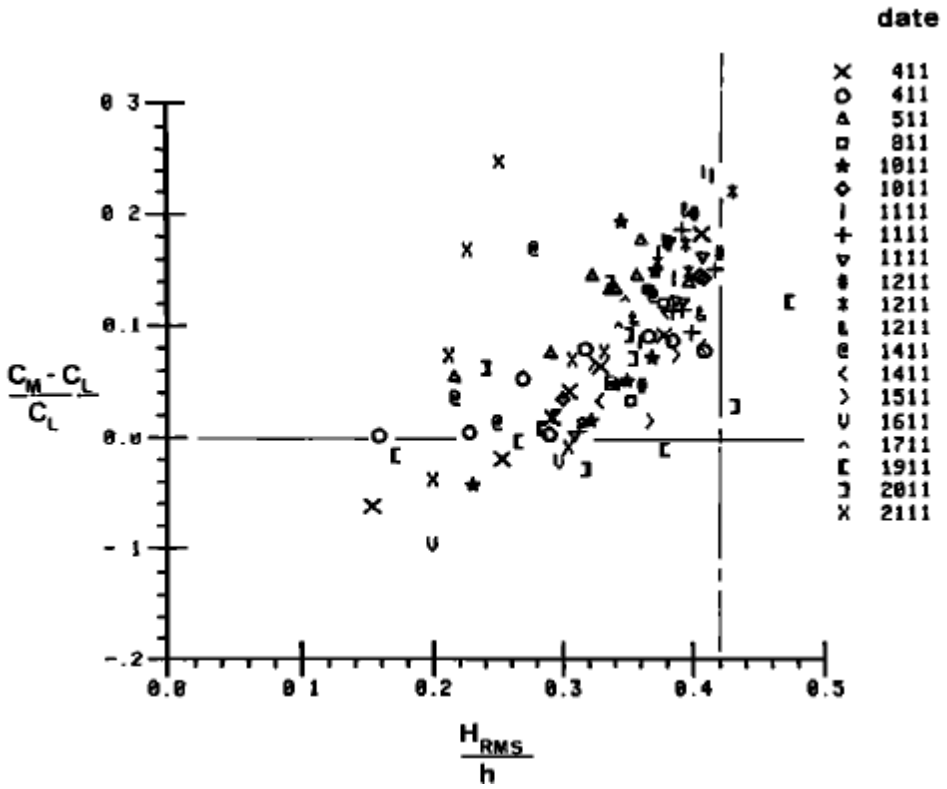

Figure 2. Differences of measured celerity from linear wave theory as a function of wave height suggesting weak amplitude dispersion (after *Thornton & Guza*, 1982)

The authors suggested that this breakdown of the dispersion relationship was due to amplitude-dispersion effects and phase coupling of the fundamental wave due to bound waves. Both mechanisms are briefly explained below.

In the inner surf zone, the relative wave height reaches typical values of 0.4 (*Thornton & Guza*, 1982). As a consequence, the assumption of small relative wave height H/h which the linear theory is based on is not valid anymore. These non linearities induce amplitude dispersion effects in shallow water, meaning wave celerity to be dependent on the wave amplitude. Thus, differences between measurements and linear theory may originate from these amplitude effects. In the study discussed above, this is manifested by the higher differences between measured and predicted celerity with increased H_{rms}/h.

Although linear theory assumes the different component of the wave field to be independent, in the nearshore a wave field consists of both free and bound waves. While free waves obey to the linear theory, bound waves are generated through resonant wave interactions and travel at the speed of the dominant frequency component even for a weakly nonlinear system, resulting in constant celerity spectra. *Crawford etal* (1981) investigated the behavior of such a wave field and found that the relative importance of the two types determines the final behavior of the system. In narrow banded energy density spectra higher harmonics are well developed and dominate the system leading to deviation from the linear theory. In *Thornton & Guza* (1982), energy ratio of the first harmonic to the fundamental was found to increase shoreward for at least one day with very narrow banded spectrum when higher harmonics were evident. That was an indication that bound waves dominated the free wave contribution on the celerity spectrum which was constant (Figure 2), implying nonlinearity due to phase coupling.

Furthermore, this breakdown of linear theory in shallow water is manifested in the depth inversion study of *Holland* (2001). Wavenumber spectra for closely spaced sensors in cross shore arrays were estimated for a depth range from 13m to the shoreline and then linear theory was inversed to produce a depth solution. While depths were accurately predicted out of the breaking region, linear theory led to overestimation even more than 50% for depths shallower than 4 m. Correlation with offshore conditions showed strong dependence with significant wave height.

2.1.2. Nonlinear wave approaches

In relatively shallow regions where the assumptions of linear theory H/L << 1 and H/h << 1 are invalid numerous wave models have been developed for the prediction of phase speed modeling amplitude effects. Non-linear wave models are divided into three categories: For non-breaking waves, for breaking waves and composite models that account for both shallow and deep water wave. A brief overview of each approach is following in the subsections 2.1.2.1 - 2.1.2.3, focusing mainly on wave models that are applicable to depth inversion.

2.1.2.1. Nonlinear models for non - breaking waves

The most broadly used non-linear wave theories for non-breaking waves are described thoroughly in *Svendsen* (2006). Equations in all these theories are controlled by two dimensionless parameters, μ and δ. The parameter μ is equal to the relative magnitude of local water depth to wave length h/L and is called the wave length parameter. Large values of it indicate relatively deep regions where waves do not interact with the bottom and they are frequency dispersive. The parameter δ equals to the relative magnitude of wave amplitude to water depth, H/h and is called the wave amplitude parameter. It represents the effects of finite amplitude on the wave phase speed, which are more significant in shallow water. The relative importance of the two terms which determines the different wave models is given by the Ursell number:

$$Ur = \frac{\delta}{\mu^2} = \frac{HL^2}{h^3} \qquad (2.13)$$

2.1.2.1.1. Cnoidal waves

An analytical solution has been developed for long waves that move in one horizontal direction and constant depth with $\delta = O(\mu^2)$ and δ relatively small (weakly nonlinear waves). Similarly to linear waves whose profile is described by a sinusoidal

function, weakly nonlinear long waves' profile is described by the elliptic cn-function. Therefore, these waves are termed Cnoidal waves.
One basic relation in Cnoidal waves is the following:

$$\frac{HL^2}{h^3}=\frac{16}{3}mK^2 \qquad (2.14)$$

which gives the value of Ursell number.
Wave celerity is calculated as:

$$c=\sqrt{gh[1+\frac{H}{mh}\left(2-m-3\frac{E}{K}\right)]} \qquad (2.15)$$

K and E are complete elliptic integrals of the first and second kind, respectively. The parameter m is the modulus of the elliptic functions and can be calculated through the Ursell number. Generally, solutions of Cnoidal waves are valid when wave length is at least 10 times the water depth. For values of m approaching zero the Ursell number gets to zero, corresponding to infinite deep water relatively to wave amplitude. For such conditions, Cnoidal waves turn out to be equal to sinusoidal waves. Hence, while the wave speed is clearly affected by amplitude dispersion effects, the m term indicates also frequency dispersion effects. Cnoidal theory is limited to water depths of $h/L_o<3/8\pi$.

The wave celerity relationship of Cnoidal theory was implemented in depth inversion studies for monochromatic waves (*Catalan & Haller*, 2008), and swell waves (*Holland,* 2001) to account for amplitude effects in the functional relationship between celerity and water depth. Wave celerity was overestimated in both studies with errors smaller of 10%. *Catalan & Haller* (2008) found errors to be uniformly distributed across the region onshore of a bar crest, with a weak dependency on Ursell number. *Holland* (2001) found predictions for h<4 m with a parameterization of Cnoidal theory to be approximately as accurate as linear theory's for deep water.

2.1.2.1.2. Solitary waves

When μ approaches 0 the Ursell number goes to infinity, corresponding to infinite long waves relatively to water depth. This leads to waves formed of just one crest as the next one is infinitely far away. This simpler form of Cnoidal waves is called solitary waves and is often used to describe non-linear behavior in the shallow water. The wave speed is given by:

$$c=\sqrt{gh(1+\frac{H}{h})} \qquad (2.16)$$

indicating no dispersion effects.

Thornton & Guza (1982) showed that application of Solitary wave theory in the saturated surf zone, for $\frac{H}{h}$ equal to 0.42, would predict wave celerity about 20% better than linear theory. Solitary theory performed well for high nonlinear environments in laboratory (*Catalan & Haller*, 2008) and field (*Tissier etal*, 2011) with celerity overestimation of about 10%. However, for trough regions where frequency dispersion effects are important, predictions deteriorated significantly (*Catalan & Haller,* 2008).

2.1.2.2. Models for breaking waves

In the surf zone a celerity model derived for breaking waves may be more appropriate. Some models have been developed that exploit the fact that broken waves can be considered analogous to a hydraulic jump or a moving bore (*Svendsen etal*, 1978). Another approach, alternative to the bore model, models the wave front as a discontinuity that satisfies shock conditions using the Saint Venant shock wave theory (*Bonneton*, 2004). Both models have been found to approximate wave celerity in the surf zone quite precisely both with laboratory (*Svendsen etal*, 1978, *Stive*, 1984, *Svendsen et al*, 2003, *Catalan & Haller*, 2008) and field data (*Tissier et al*, 2011). However, they both require water depth under the wave crest and trough as an input, constituting their application in depth inversion rather complicated. A simpler approach, described below, is a modification of the linear theory for the surf zone.

Svendsen et al (1978) found breaking wave celerity to be typically proportional to the linear prediction $\sqrt{gh}$ (Figure 3). Therefore, a simple approach is to model the wave celerity in the surf zone with a simple modification in the form of $c = a\sqrt{gh}$.

Schaffer etal (1993), based on lab experiments of *Stive* (1980) where the front of a broken wave was found to travel ~30% faster than the linear shallow water celerity, made the approximation:

$$c = 1.3\sqrt{gh} \qquad (2.17)$$

Schaffer et al (1993) used this empirical modification of the linear theory in a wave model for both inside and outside the surf zone. Wave height and surface elevation prediction of the model were generally good except on the onset of breaking.

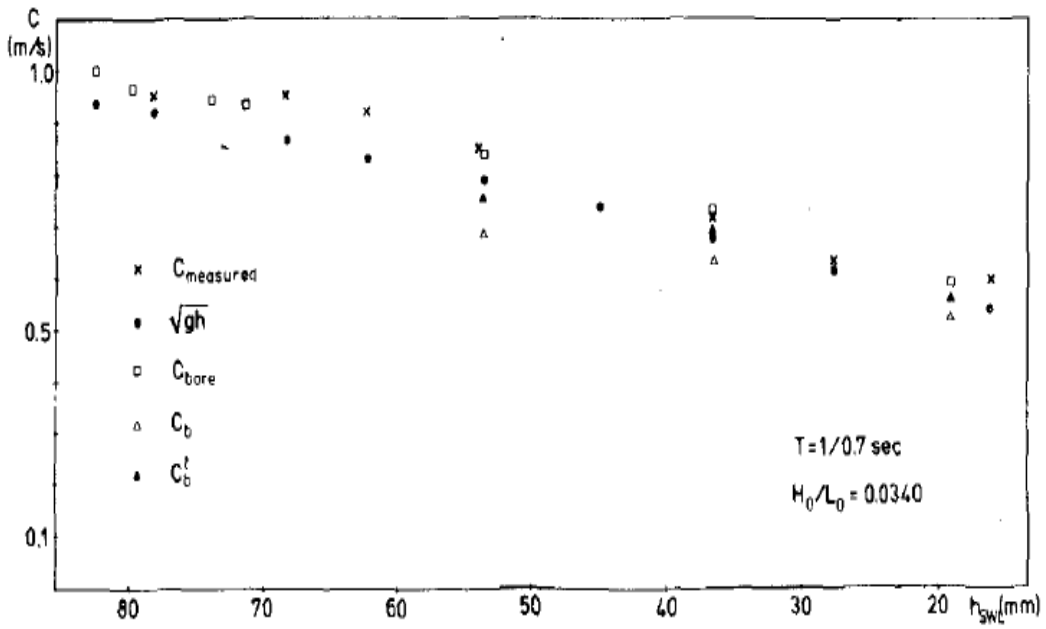

Figure 3. Measured and computed values of wave phase speed. It seems that measurements are slightly higher but still proportional to the linear prediction (after *Svendsen et al* (1978)).

However, the studies of *Bonneton* (2004) and *Catalan & Haller* (2008) showed that this parameterization often overestimated the wave front celerity. This was confirmed by *Tissier et al* (2011) who modified the above equation to

$$c = 1.14\sqrt{gh} \qquad (2.18)$$

as they found it in better agreement with observations available from sensors inside the surf zone. However, it was found that measured celerity of broken waves in the inner surf zone and for high values of δ (>0.4) were up to 2.5 higher than the predictions of linear theory for shallow water (Eq. 2.8). This demonstrates that an approximation such as $a\sqrt{gh}$ is inappropriate for high nonlinearities.

2.1.2.3. Composite models

The models described in sections 2.1.2.1 – 2.1.2.2 concern waves in shallow water. However, nonlinear effects can also be of importance in the intermediate depths of the shoaling zone (*Catalan & Haller*, 2008). In particular, the onset of breaking which is included in this region can cause large discrepancies to phase speed predictions.

2.1.2.3.1. KD86 model

A composite model was proposed by *Kirby & Dalrymple* (1986) giving a single expression for the phase speed. The model combined the Stokes theory for deep and intermediate depths with an approximate shallow water dispersion relationship for the shallow water (*Hedges*, 1976) shown below:

$\omega^2 = gktanh(k[h+H])$

The authors suggested the equation:

$$\omega^2 = gk(1 + f_1(kh)\delta^2 D)tanh(kh + f_2(kh)\delta) \qquad (2.19)$$

with

$$D = \frac{\cosh(4kh)+8-2tanh^2(kh)}{8sinh^4(kh)}$$

and

$f_1(kh) = tanh^5(kh)$

$f_2(kh) = [kh/sinh(kh)]^4$

The model enables a smooth transition from Stokes theory to the shallow water approximation of *Hedges* (1976).

When $kh \to \infty$

$f_1(kh) = 1 \quad and\ f_2(kh) = 0$

and the model collapses to Stokes theory.

When $kh \to 0$

$f_1(kh) = O(Kh^5) \quad and\ f_2(kh) = 1$

the model collapses to Hedges model.

Therefore, the problem that arises from the invalidity of Stokes theory in shallow water and the inadequacy of approximate shallow water relation to model nonlinearities in intermediate depths is alleviated.

The derived dispersion relationship was implemented by the authors in a wave model used in laboratory experiments to calculate amplitudes of monochromatic waves propagating into an elliptic shoal. The predictions were in very good

accordance with the corresponding laboratory measurements in both shallow and deep water.

Furthermore, the model had the best performance amongst the models used in *Catalan & Haller* (2008) inside the surf zone and was chosen to be applied for depth inversion (Figure 4). Depth estimations included errors of about 10% improving significantly predictions acquired by the linear theory (errors~30%).

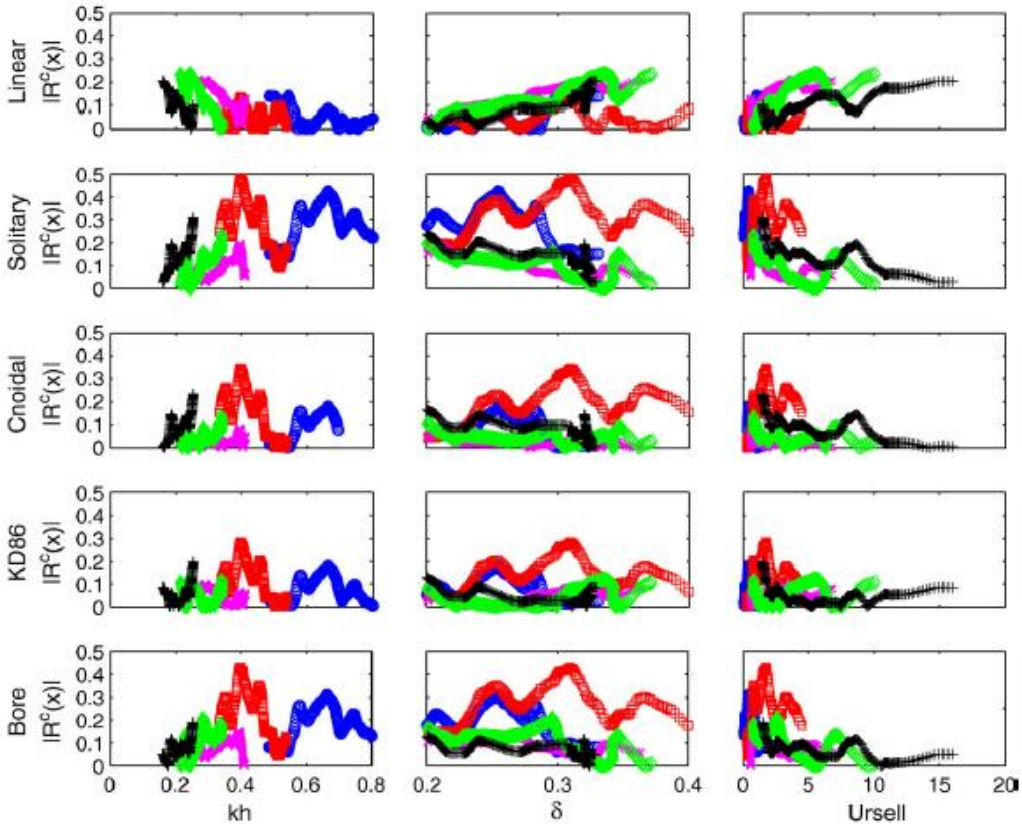

Figure 4. Distribution of the absolute error for different wave models against dispersiveness (kh), non-linearity δ and Ursell number for 5 different wave conditions in the laboratory experiments of *Catalan & Haller* (2008).

2.1.3.2.2. Booij model

Booij (1981) suggested a composite model which models the amplitude dispersion in shallow water and becomes asymptotic to the linear dispeprsion relation in deep water. The model has the form:

$$c = \sqrt{\frac{g}{k} tanh(k * \left(h + \frac{H}{2}\right))} \qquad (2.20)$$

and it can be inverted directly.

The model showed the same trend as the KD86 model in the phase speed observations of *Catalan & Haller* (2008) inside the surf zone. Because *Booij* (1981) model can be inverted directly, oppositely to the KD86 model which has to be solved iteratively requiring much computational effort, the authors suggested it as an alternative for depth inversion.

2.2. Monitoring the sea with video cameras

Measuring characteristics of waves remotely to retrieve water depth is not a new idea. First attempts were back in the World War II when scientists were interested in beach gradients for safe military landing and approaching of coasts (*Williams, 1946*). Time-lapse aerial pictures of sea surface were taken. The travelling distance of a fixed point was estimated and then divided by the time between successive images giving the wave phase speed. Short crested wind waves traveling with the long-crested, high amplitude waves hindered the clear identification of the dominant wave resulting in poor results. Nowadays, most advanced systems enable the monitoring of nearshore processes continually.

The Argus program, created in 1986 by the Oregon Imaging Lab, has fulfilled the requirements for sampling the nearshore frequently and over extended spatial scales through shore based stations equipped with video cameras. Features and processes such as submerged sandbars (*Lippmann & Holman*, 1989), bathymetry (*Stockdon & Holman*, 2000, *Plant et al*, 2008, *Holman et al*, 2013) and wave runup (*Holland and Holman*, 1999) can be derived from video intensity data. For a description of the technical capabilities of Argus and its historical evolution the reader is referred to *Holman & Stanley* (2007).

The estimation of the phase speed of a propagating wave using remote sensing techniques is feasible since the waves have a measurable optical signature. The relationship between the true wave signal and a remotely sensed video signal can be described by the modulation transfer function (MFT) $M(f)$, a spectral representation of the relative amplitudes and phases. MTF depends on the mechanism through which waves are imaged by the camera.

Seaward of the breaking point, sea surface is visible primarily by specular reflection of the incident light. Variations in the surface cause reflection from different elevations in the sky, with the seaward and landward face of a wave to be bright and dark respectively (*Stockdon & Holman*, 2000). However, in regions that wave slope changes rapidly, brightness variations can be induced hindering the identification of a wave (*Catalan & Haller*, 2008). In the non-breaking region, the phase of MTF is steady except in the final stages of shoaling.

When breaking begins, the white foam associated with the turbulence causes scattering reflection which acts as the main recognizing mechanism (*Stockdon & Holman*, 2000). Signal of wave is now a white face and the phase relationship between the true and imaged signal differs but it is still coherent.

2.3. cBathy

2.3.1. Depth Inversions – Towards cBathy

Depth inversion refers to numerical or experimental methods by which the ocean bottom bathymetry in coastal areas is predicted using properties of waves measured on the ocean surface (*Grilli etal*, 1998). A number of authors have tested methods where the wave kinematics are extracted from remote sensing data and linked to water depth through a functional relationship. Usually, this relationship is mathematically expressed by the dispersion relationship (2.3) for linear waves. For given values of k and σ, the analytical solution for h can be achieved after inverting the dispersion relationship:

$$h = \frac{1}{k} tanh^{-1}\left(\frac{\sigma^2}{gk}\right) \qquad (2.21)$$

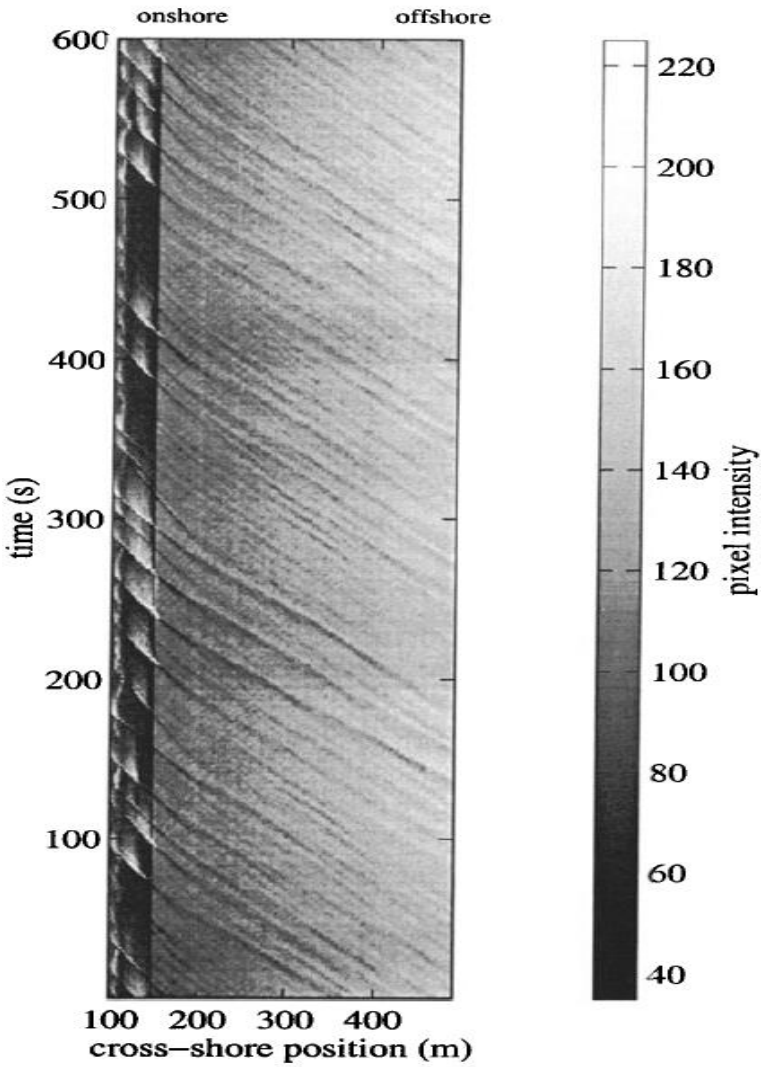

Figure 5. Cross shore timestack from Duck, USA. Bright regions indicate wave breaking over shallow features. The diagonal traces of the wave crests define the shoreward progression of the waves (after *Stockdon* & *Holman*, 2000)

The depth inversion algorithm cBathy (*Holman etal*, 2013) extends the basic principles of the methods developed during the past years by *Stockdon & Holman* (2000), *Dugan et al* (2001) and *Plant et al* (2008). *Stockdon & Holman* (2000) used 1-D arrays of pixel intensity time series (timestack, Figure 5) and applied Fourier transformations on the signal. They calculated the wavenumber at each pixel location as the slope of the phase of the first EOF (Empirical Orthogonal Function) of the cross-spectral matrix and for a dominant frequency. Inversion of the linear theory for the depth solution yielded reasonable estimates. *Dugan et al* (2001) expanded the analysis in 2-D using images from an airborne-adapted camera for a large domain and for intermediate depths. Results were good but the spatial resolution enabled by the method was limited. *Plant etal* (2008) developed a cross-spectral correlation approach. A set of analysis locations was defined and Fourier transformation of 1-D pixel arrays was applied to calculate the cross-spectral matrix. In each location and for a set of candidate frequencies, the wavenumber was estimated as the value that maximized the coherence of the cross-spectral matrix and using a nonlinear least squares method. Results were found to be quite in agreement with field data while error bars for each wavenumber estimate were also returned.

cBathy enables the analysis of the wave field in full 2-D arrays and with much finer resolution than in *Dugan et al* (2001). Analysis is taken place in a set of analysis

points (x_m, y_m) (Figure 6) predefined by the user, similarly to *Plant et al* (2008). Moreover, after each hourly prediction a Kalman filter is implemented based on confidence intervals and a process error. The filter deals with bad images caused by weather conditions such as fog, rain drops or sun glare that reduce the signal to noise ratio. In that case, the filter produces a smooth running average bathymetry. The algorithm is run into three different steps, described below.

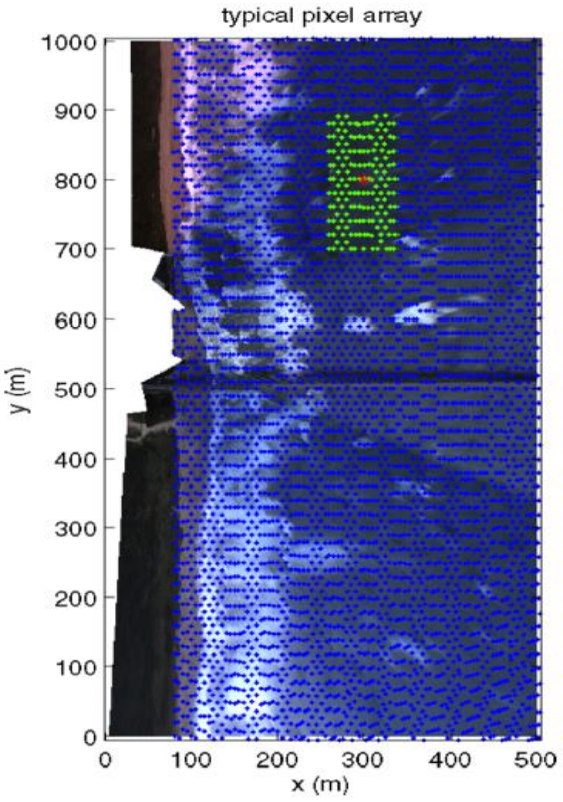

Figure 6. Example pixel array used for cBathy analysis. For each analysis location (red point) depth is estimated based on cross-spectral phase within a nearby region (tile, green pixels) (after *Holman et al*, 2013)

2.3.2. Frequency dependent analysis

The input to the algorithm is time series of pixel intensity collected in a user defined grid of sampling locations. Time series are Fourier transformed such that:

$$G(x_p, y_p, f) = FT\left(I(x_p, y_p, t)\right) \qquad (2.22)$$

I is the pixel intensity at each pixel location and G is the Fourier component at frequency f.

The whole sample is then subdivided into smaller tiles of interest which span the region ($x_m \pm L_x$, $y_m \pm L_y$).

After that step, for each tile and for each 17-minutes run, the cross-spectral matrix C is computed correlating all possible pixel pairs for each of the candidate frequencies f:

$$C_{i,j}(f) = \langle \hat{G}(x_{pi}, y_{pi}, f)^* \hat{G}(x_{pj}, y_{pj}, f) \rangle \qquad (2.23)$$

where superscript * indicates the complex conjugate and the expected value is averaged across each frequency band.

For natural seas, the effects of multiple wave trains are usually mixed in the cross-spectral matrix. To extract only coherent motions from this mix, the dominant eigenvector, $v(x_P, y_p, f)$ and its associated eigenvalue λ are estimated using EOF analysis. EOF analysis is a method for analysing propagating signals from data collected over spatially separated sensors and involves eigenvector analysis of the cross spectral matrix for a frequency of interest (*Wallace & Dickinson*, 1972). For each frequency, a best match between the observed spatial phase structure of v

$$v' = \tan^{-1}\left(\frac{imag(v)}{real(v)}\right) \qquad (2.24)$$

and the predicted, modeled as

$$\boldsymbol{v'} = exp(i[kcos(a)x_p + ksin(a)y_p] + \varphi) \qquad (2.25)$$

is solved nonlinearly using the Levenberg-Marquardt method (see *Gavin* (2013) for a brief description) and yields a first estimate of wavenumber k and wave direction α for a single frequency.

The contribution of each pixel to the estimation of k and a is weighted using the spatially variable magnitude of the eigenvector v, $|v(x_P, y_p)|$ and the distance from the analysis point. The latter is smoothed by half the tile size so that it is expressed by a Hanning filter as $\Gamma\left(\frac{x_p - x_m}{L_x}, \frac{y_p - y_m}{L_y}\right)$. Γ has magnitude 0.5 at $\left(\frac{x_p - x_m}{L_x}, \frac{y_p - y_m}{L_y}\right)$ = 0.5 and Γ = 0 for $\left(\frac{x_p - x_m}{L_x}, \frac{y_p - y_m}{L_y}\right) = 1$. Thus, the nonlinear search for optimum wavenumber and angle at each point is performed by minimizing the error between the predicted values of $v'(x_P, y_p)$ and the observed values of $v'(x_P, y_p)\, w\,(x_p, y_p)$, with $w\,(x_p, y_p) = |u(x_P, y_p)|\,\Gamma\,(x_p, y_p)$.

For each pair of candidate frequency and wavenumber, the water depth of the considered location ($\tilde{h}$) is calculated using the linear dispersion relation. To minimize the calculation effort, water depth estimations at each tile are retained only for the four most coherent frequencies. In addition, 95% confidence intervals, skill fit s, normalized eigenvalue $\hat{\lambda}$ and the degrees of freedom are returned. Lastly, threshold values are set to reject water depths that seem to be abnormally shallow or deep.

2.3.3. Frequency Independent Analysis

The objective of the second phase of cBathy is to extract single frequency-independent depth estimation for each tile using the results from the previous phase. The final depth $\hat{h}$ equals to the value that yields the best fit between the wavenumbers calculated during the phase 1 and the wavenumbers predicted by linear theory for each frequency. The depth estimates of phase 1 are used as a seed for the initiation of the nonlinear fitting. The nonlinear search for the best fit is accomplished again using the Levenberg-Marquardt method. Because bathymetry is expected to vary with a typical scale of L_x, estimations from adjacent analysis locations are used in the best fit through a weight function w_2. This function depends on the distance of the adjacent location, expressed through Γ, the importance of the first EOF, expressed through $\hat{\lambda}$ and the skill of each fit, s. Since low skill and low eigenvalue fits have already been removed, w_2 is more dependent on the distance of adjacent location. Estimates are returned again with confidence intervals. Finally, water depths from phase 1 and 2 are tidally corrected to yield bathymetries.

2.3.4. Running Average Bathymetry

The product of phase 3 is a running average bathymetry $\bar{h}$ through a Kalman filtering process (*Kalman*, 1960) applied on the time domain. For a given time k, after an hourly cBathy run, in each tile the bathymetry is updated weighting statistically the confidence in the computed bathymetry with the confidence for time k-1 and accounting for a process error Q which represents the unmodelled morphologic variability between the two sampling times. The process error varies in space and time and has to be calculated through field data if available or otherwise guessed.

Thus, for a time k, after Q is calculated the variance error of the running average P_k^- is calculated prior to update:

$$P_{\boldsymbol{k}}^- = P_{k-1} + Q\Delta t \qquad (2.26)$$

Δt is the time interval in days between estimates.

Then, the trustworthiness of the new estimate $\hat{h}$ is compared with the running average $\bar{h}$ through a Kalman gain K_k:

$$K_k = \frac{P_{\boldsymbol{k}}^-}{P_{\boldsymbol{k}}^- + R} \qquad (2.27)$$

where R is the variance error of the current estimate calculated as $\hat{\sigma}^2$.
Afterwards, the Kalman gain is implemented in the final estimate-update of the running average by:

$$\bar{h}_k = \bar{h}_{k-1} + K_k(\hat{h}_k - \bar{h}_{k-1}) \qquad (2.28)$$

Therefore, for small values of R, $K_k = 1$ and the prior estimate is ignored while for large variance errors of the current estimate $K_k = 0$ and the current estimate does not contribute to the running average.
Finally, the estimated error variance is updated depending on the Kalman gain by:

$$P_{\boldsymbol{k}} = (1 - K_k)P_{\boldsymbol{k}}^- \qquad (2.29)$$

2.3.5. cBathy settings

In order for cBathy to achieve accurate and robust final estimates, the user has to predefine a number of parameters that are used in the different steps of the algorithm.

Firstly, the spacing distance between analysis locations (x_m, y_m) is defined depending on the spatial scales of bathymetric features that will be resolved. Secondly, user should define the spatial extent of the analysis grid, depending on the size of pixel arrays. Thirdly, for each Argus station tidal level data are available which are used after phase 1 and 2 for the correction of the depth estimate.

Furthermore, since cBathy incorporates weighting processes and error estimations, a second group of parameters that are used in these processes have to be set. Analysis tile dimensions and smoothing scales used in Hanning filter L_x, L_y are determined by the desired resolution. They should ensure the inclusion of an adequate number of pixels in every estimation. To do so, tile size should be smaller than the expected deep water wavelength. The smoothing scales depend on the cross shore position. While near to the shore variability scale is small and thus the

smoothing scale has also to be small, more offshore the variability scale is longer and more smoothing is allowed. The smoothing scale is linearly increased towards the offshore boundary by factor k which is also to be defined. When the tile size is maximized, the computational time is substantially raised. To avoid this, the number of pixel at each tile is decimated to a maximum value which still allows the wave phase structure to be sampled adequately for the estimation of its spatial gradient.

The range of examined frequencies should match the wave frequencies that are encountered at the site. To minimize the calculation effort, only a user-defined number of frequencies with the largest coherence over each tile is retained for further analysis after phase 1. Usually this number is set to four.

Lastly, threshold values have to be defined for checking of unrealistic estimates of phase 1. Returned values of depth lying in the vicinity of swash zone (($\tilde{h}$) <0.25) where linear wave celerity is not valid or in the relative deep water where waves do not feel the bottom are rejected. Estimates with a skill or λ lower than a threshold value (usually < 0.5 and <10 respectively) are also rejected.

2.3.6. cBathy results

The method was tested on the barred beach of Duck and the dissipative low sloping coast of Agate by *Holman et al* (2013) and the site of Sand Engine on the Dutch coast (*Wengrove et al*, 2013). It should be mentioned that the wave climate is different among the three sites and thus different settings were used for each one.

In all three cases cBathy managed to resolve bathymetric features quite accurately including sandbars and rip channels. The highest offshore waves resulted to depth overprediction (*Holman* et al, 2013), consistent with finite amplitude effects not modeled by the dispersion relationship, while *Wengrove et al* (2013) found the largest discrepancies to lie at camera intersections.

The Kalman filtering anticipated signal failures due to weather condition and filters the low coherence of signal on the onset of breaking, being a key in the performance of the cBathy (*Holman etal*, 2013).The largest deviations of hourly depth estimations $\hat{h}$ from the running average occurred on the onset of breaking. They were attributed to failure of linear theory for breaking waves and wrong estimations of wavenumber during phase 1 due to mixing of optical signals for breaking and non-breaking waves, both consistent with previous studies (*Holland*, 2001, *Stockdon & Holman*, 2000). However, they passed through Kalman filtering with little impact.

2.4. Research focus

The depth inversion algorithm cBathy has been tested in a number of Argus sites performing fairly well. The performance of the algorithm in other sites is still under question, depending on the wave climate and morphology of each coast. Furthermore, errors in depth inversion studies have been found to be correlated with offshore wave height, indicating that amplitude effects not modeled by the linear dispersion relationship during depth inversion led to depth overestimation.

The present study aims at the extraction of nearshore bathymetry using cBathy at the Argus site of Coast3D in Egmond aan Zee, in the Netherlands, focusing mainly in the intertidal area where nonlinearities are more pronounced. This research goal is achieved by answering the following research questions:

1) Which are the required settings in order to achieve the best performance of cBathy at Egmond?
2) Can wave nonlinear effects be detected in cBathy celerity output and how do they affect the final depth estimation?
3) Can the use of a nonlinear predictor improve the final depth estimation?

3. Methodology

3.1. Dataset

3.1.1. Introduction to the study area

The study area is located at the Dutch coast near Egmond aan Zee, 3 kilometers southwest of the village and in front of the Coast 3D Tower Argus station. The research is mainly focusing on the intertidal bar, which extends from the high water line to about 100 m offshore in a water depth of about 2 m.

The bathymetric profile consists of 3 sandbars. One outer subtidal bar with a crest with a mean water depth of -2.5 to -4 m, an inner subtidal bar with mean water depth -1 to -3 m and an intertidal bar which is smaller than the subtidal bars. The two subtidal bars migrate onshore during low energy conditions and offshore during energetic conditions, while the intertidal bar is highly variable and can be disappeared during highly energetic conditions.

The spatial coordinates of the site, used in the rest of the report, are defined according to the Argus coordinate system (*Aarninkhof etal*, 2007). The x and y axes are perpendicular and the rotation from the x-axis to the y-axis indicates the counter clockwise or positive turning direction. Thus, the cross shore coordinate increases positively in the offshore direction and the longshore coordinate increases left of the Argus tower when looking offshore, thus south of it for the Egmond site.

3.1.2. Argus data

Video images from cameras 1 and 2 of the Argus tower are available for analysis, covering a period from 3 to 15 and 23 of October 2011. Camera 1 views at the northwest direction while camera 2 looks to the west with its view reaching more offshore. The images were collected hourly with a sampling frequency of 2 Hz, usually from 06.00 am to 17.00 pm. Furthermore, snapshot and time exposure (timex) image products are also available for visual qualitative assessment of image quality and weather conditions (see example in Figure 7). Timex images are the averaged intensity of all frames collected over a 10 – minute period for each hour. White bands correspond to areas of wave breaking such as submerged sandbars.

3.1.3. Available field measurements

Field data for the same time period are also available from a fieldwork study (*Brinkkemper*, 2013), covering the intertidal area. Measurements of wave height and water depth exist for a cross shore transect of 9 pressure gauges (OSSI, Ocean Sensor Systems Inc.) with the most offshore sensor lying at 80 meters offshore, at the longshore location $y = -272$ m. Wave height measurements correspond to the significant wave height H_{m0} for the high frequency waves (0.05-1 Hz).

Bathymetric profiles for a cross shore transect along the intertidal bar were acquired by interpolation of measurements taken by a DGPS (Differential Global Positional System) device every day during low tide. The measurements extend from the shoreline up to 80 m offshore and their longshore position correspond to y = -272 m. In addition, bottom topography of the intertidal area for a region spanning 250 m to the south and 250 m to the north of the transect was measured by the DGPS adjusted to a quad for some days. The cross shore range of those measurements reaches typically up to 80 m offshore but varies on the longshore direction and also between the days.

Offshore wave conditions are also available for the entire study period. The offshore wave height H_{m0}, offshore wave period T_{mean}, and mean angle of incidence θ_o were measured every 30 minutes 15 km southwards at 26 meters water depth, in front of the city of IJmuiden. Wave conditions were found to vary during the study period (Figure 8). The offshore wave height varied from a minimum value of 0.24 m to a maximum of 3.3 m with an average value of 1.4 m. T_{off} varied from 3.6 sec up to 8.4 sec with a mean value of 5.7 seconds, typical for the Dutch coast. Most of the days, waves were found to approach the shore from the southwest with an average direction of -35^{O}, while for three days waves were reaching from the north with an angle of incidence up to 80^{O}, corresponding also to the three days with the highest period (8th, 13th and 14th of October).

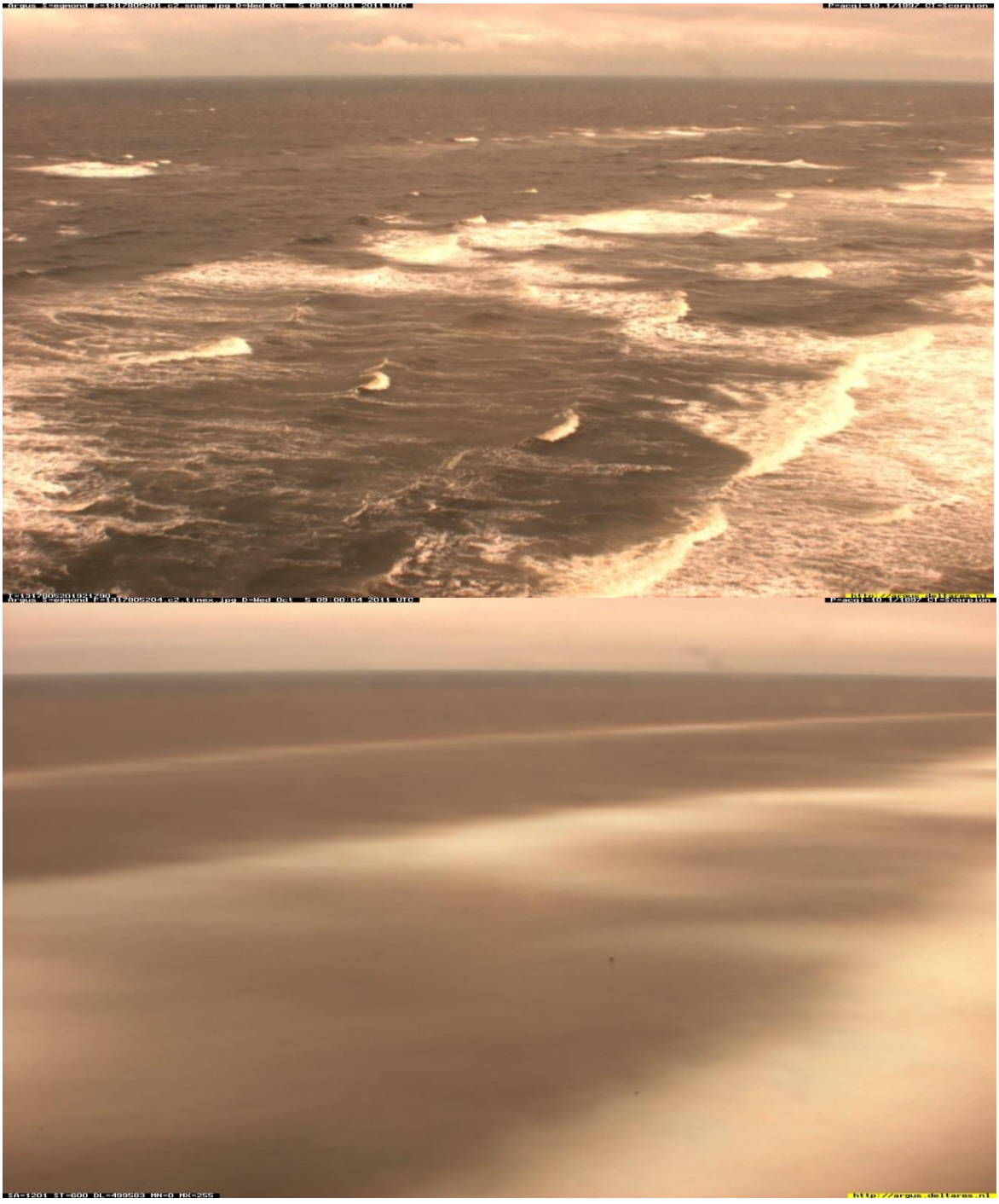

Figure 7. Examples of snapshot (above) and timex (below) images at COAST3D, Egmond, camera 2 for 5 October 09:00:00 GMT.

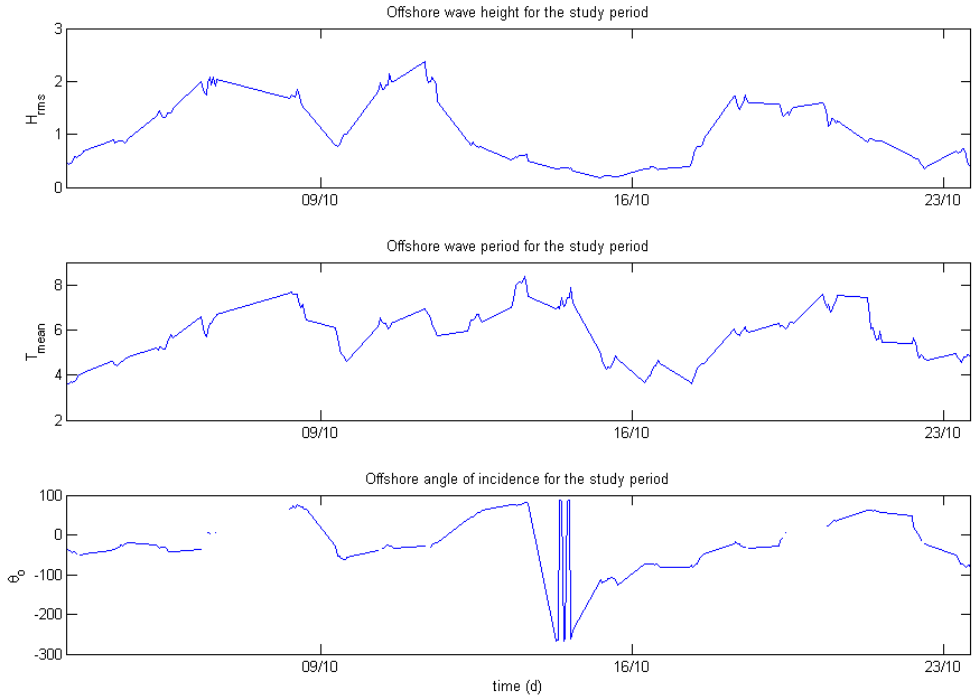

Figure 8. Offshore wave conditions of the study period, 03/10 – 23/10, 2011.

Besides the DGPS measurements of bed elevation for the intertidal zone, bathymetrical data from a measurement campaign conducted by Rijkswaterstaat the first week of November are also available. The data extend up to 1700 offshore while they span the coast in the longshore direction from 1800 to -2300 m. They consist of multiple cross shore transects spaced every 250 m along the coast. An interpolated bathymetric profile was acquired by the Loess method (*Plant etal*, 2009), with smoothing scales Lx and Ly equal to 10 and 400 m respectively.

3.2. Pixel sampling

The input data to cBathy are pixel intensity time series collected at a grid whose coordinates are predefined by the user. The spatial distance between two pixels in the cross and longshore direction Δx_p and Δy_p respectively, is determined by the requirement to have a sufficient number of pixels per expected wavelength in order to resolve waves.

According to *Plant etal* (2008), waves longer than two times the Nyquist wavelength are well resolved. The Nyquist wavelength is the shortest resolvable wavelength and it equals two times the sampling distance. Thus, in the cross shore direction waves are well resolved if the wavelength L equals at least four times the sampling distance Δx_p.

At Egmond, with a typical Dutch wave climate, the mean wave period is about 5.5 seconds. Using the linear theory approximation in shallow water $c = \sqrt{gh}$ and solving for L in water depth of 1 m yields:

$$L = 17.2 \text{ m}$$

which is the minimum resolvable wavelength for $\Delta x_p = \frac{17.2}{4} = 4.3$ m. As shorter waves will be encountered in shallower water, the pixel spacing should allow smaller wavelengths to be resolved. With a pixel spacing distance of 3.5 m, waves of wave

length $4 * \Delta x_p = 14\,m$ are well resolved. With such a sample design, 5.5 s waves are well resolved up to a depth of:

$$h = (\frac{14}{5.5})^2/g = 0.65 \text{ m}$$

Thus, the distance between two pixels in the cross shore direction was chosen equal to 3.5 m. Because scales of bathymetric variability are longer in the longshore direction, Δy_p was set to 10 m. Therefore, the collection scheme was 3.5x10 m, spanning a region from 10 to 650 m offshore in the cross shore direction and -600 to -40 in the longshore direction.

Concerning the temporal resolution, data were collected with a sampling frequency of 2 Hz for 1024 seconds every hour, resulting in 2048 measurements of intensity for each sampled pixel.

3.3. Image processing

3.3.1. Conversion between world and image coordinates

In order to quantify the information provided by an image, the 3-D world coordinates (*x, y, z*) of any point must be transformed into 2-D image coordinates (u, v) (*Lippmann and Holman*, 1989). The (*x, y*) coordinates are given by the collection scheme (section 3.2. Pixel sampling) while the vertical *z* is constraint to the actual tidal level. Transforming from world to image coordinates (camera calibration) and vice versa (camera rectification) is based on the photogrammetric relationships between the world and image coordinates of each point and it is determined by the intrinsic and extrinsic parameters of the camera. All the relationships that allow conversion are described in detail in *Holland et al*, (1997) along with a camera calibration technique used to estimate the intrinsic parameters, e.g. the camera field of view, details about the sensors and the distortion parameters of the lens.

The extrinsic parameters describe the geometrical orientation and position of the camera relatively to a reference coordinate system and they consist of the world coordinates of the camera center (x_c, y_c, z_c) and the rotation angles of azimuth (φ), tilt (τ) and roll (σ). While the former can be surveyed in the field, the latter remain unknown. Nevertheless, using a number of Ground Control Points (GCP), objects with known world and image coordinates, yields a solution for the three angles via an iteration technique. Thus, the first step for calibrating the camera was to estimate the three angles, a process called 'solving for the image geometry' by *Holman & Stanley*, 2007.

For each camera, a set of measuring poles was used as GCP, together with the horizon line. Geometry solutions were updated almost for each day, usually defined during low tide for when the poles were easily visible and then set to be valid for the whole day. While determining the geometry solution is more crucial during the stormiest conditions as the camera orientation is highly susceptible to changes due to wind, it is also more difficult to acquire one because the GCP cannot be clearly observed even at low tide. One such day (7 October) was excluded from the subsequent analysis.

Once geometry solutions were defined, the image coordinates that correspond to the pixel sampling scheme were calculated (Figure 9), accounting for distortion. For pixels that were contained in the field of view of both cameras, a priority in the collection was given to camera 1, as that overlapping occurred for locations where resolution of camera 1 was finer. Subsequently, the undistorted image coordinates

were converted to the corresponding world coordinates for the creation of timestacks, input to cBathy. After the image was rectified, data from both cameras were merged resulting in a planar map with the real world coordinates (always with reference to the Argus coordinate system) of each sampled pixel array.

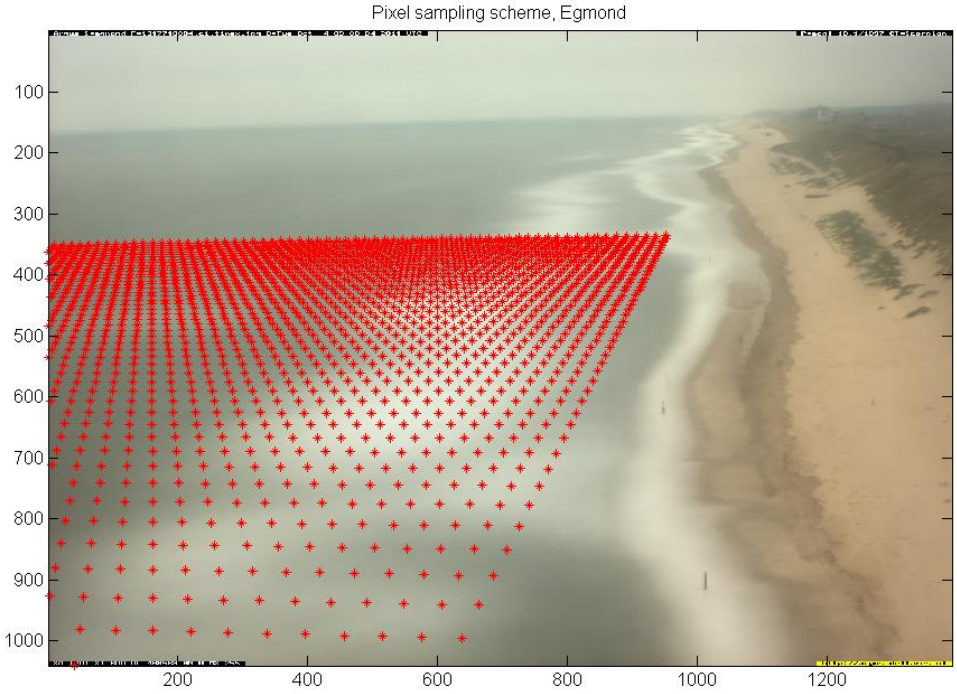

Figure 9. Pixel sampling scheme at COAST3D for camera 1, Egmond, 4 October 09:00:00 GMT.

3.3.2. Spatial Resolution

In digital images, the spatial resolution of each pixel is determined by the projection from the camera pinhole lens through the pixel onto its ground footprint. This resolution has components Δ_r and Δ_c in the range (radially away from the camera) and the cross-range (azimuthal) directions, respectively. Generally, resolution worsens with the slant range distance from the camera as pixels stretch out, with the range component being more sensitive (*Holman & Stanley*, 2007).

A sensitivity analysis conducted for the pixel resolution of the defined sample region. The resolution components were estimated by the equations given in *Holman & Stanley* (2007):

$$\Delta_c = R\frac{\delta}{NU}$$
$$\Delta_r = \Delta_c R/z_c$$

where R, the slant range distance
δ, the angular field of view
NU, the width of the image
z_c , the camera height above the surface of interest (usually the mean sea level)

Subsequently, they were converted to resolution in the cross shore and longshore direction, to be comparable to the local world coordinates. The transformation equations are:

$$\Delta_x = \max(|\Delta_c \cos a|, |\Delta_r \sin a|)$$
$$\Delta_y = \max(|\Delta_r \cos a|, |\Delta_c \sin a|)$$

If the resolution component in one direction is larger than the pixel spacing in the same direction, then intensity samples for the same pixels will be collected, degrading the subsequent cBathy analysis. Generally, resolution was found to be finer than both Δx_p and Δy_p except for the most distant points covered by camera 2 and only for the cross shore component. These points are lying mainly in the northwest corner of the domain, between x = 400 m and x = -650 m and y = -600 m and y = -300 m (Figure 10).

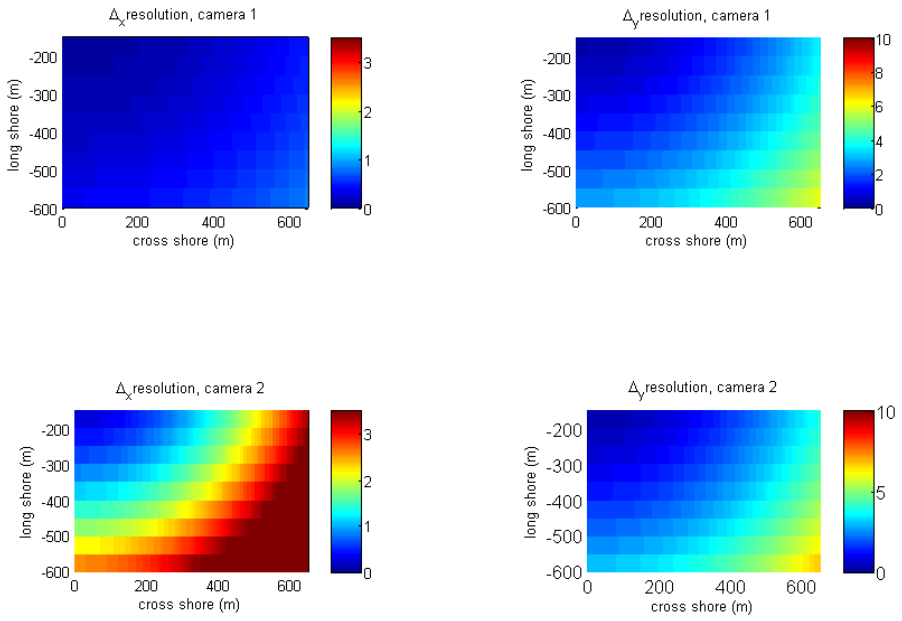

Figure 10. Cross shore and longshore components of resolution for cameras 1 & 2.

3.4. Set up cBathy

3.4.1. Settings

Applying cBathy to a new location requires some of the initial parameters to be adjusted to the waves and morphological characteristics of the site. The spacing between analysis locations was initially set to 10 and 20 meters in the cross shore and longshore direction, respectively. The range of the candidate frequencies was set to 0.1 – 0.3 Hz to host the low period waves of the Dutch coast. Based on the surveyed bottom topography the maximum depth was set to 10 m. For the rest of the parameters, the values used in the Duck study case were used (*Holman et al*, 2013). All the cBathy settings are listed in Table 1.

Table 1. cBathy settings, Egmond study case

Parameter	Value	Purpose
Δx_m	10	Cross shore distance between analysis locations
Δy_m	20	Long shore distance between analysis locations
$xMinMax$	0, 650	Cross shore limits of the analysis
yMinMax	-600, -40	Long shore limits
h_{min}	0.25	Minimum acceptable depth
h_{max}	10	Maximum acceptable depth
q_{tol}	0.5	Minimum acceptable skill of phase 1 nonlinear fitting
λ_{min}	10	Minimum acceptable normalized eigenvalue, phase 1
L_x	20	Smoothing scale in the cross shore direction
L_y	40	Smoothing scale in the long shore direction
κ	2	Smoothing scale expansion at the offshore boundary
$maxNpix$	80	Maximum number of pixels used in each tile analysis
f	$\frac{1}{10}:\frac{1}{50}:\frac{1}{3}$	Analysis frequency bins
$nKeep$	4	Number of frequency bands retained for analysis, phase 1
$offshore\ angle$	0	Offshore wave angle, used for seed in phase 1

3.4.2. Process Error

Before running the phase 3 of cBathy, it is necessary to approximate a model for the estimation for the process error Q. *Holman et al* (2013), based on a dataset of bathymetric surveys for 36 days, modeled Q as:

$$Q = C_Q H_{mo}^2 exp\left\{-\left[\frac{x - x_o}{\sigma_x}\right]^2\right\}$$

where C_Q represents the maximum in the cross shore variability, measured in units/day, x_o is the cross shore position of maximum variability, σ_x expresses the spread of the variability and H_{m0} is the measured offshore wave height.

In absence of such an extended dataset, the parameters have to be guessed. Based on *Ruessink et al* (2007), the location of the inner subtidal bar at x = 200 was chosen as x_o while σ_x was set to 70 m. For the value of C_Q, the value 0.067 which was calculated for Duck was used.

4. Results

The analysis of the results is separated into four parts. The first part focusses on the validation of cBathy for the site of Egmond by comparing the cBathy estimates with the Rijkswaterstaat bathymetric measurements for the whole analysis domain (30<x<650 m and -600<y<-150 m). As the current study is focusing on the surf zone, the second part examines the cBathy performance inside the intertidal zone where wave dynamics can be highly nonlinear and possibly influence the accuracy of depth inversion. Subsequently, celerity outputs of cBathy are examined in detailed and compared with celerity predictors available in literature. Finally, these predictors are applied in the depth inversion solution of cBathy and compared with the default version.

In the rest of the report, two error statistics are used to assess the cBathy predictions: The rms error, calculated as $rmse = \sqrt{\sum_i^N \frac{(pred-obs)^2}{N}}$ and the bias, computed as the mean of the vertical difference between predictions and observations.

4.1. cBathy validation

2-Hz video data were available until the 23rd of October while the Rijkswaterstaat bathymetry measurements were made at the beginning of November. As no storms occurred in between (maximum H_{rms} measured offshore was 1.2 m), it is assumed that no big morphological changes occurred at the offshore part. The cBathy hourly result of October 23, 15:00:00 GMT, as the most recent relatively to the field measurements, is chosen for comparison with the field data. The offshore wave height and period for that day was 0.58 m and 5 sec respectively and waves were approaching the shore from the north with an angle of incidence 12°.

The cBathy predictions compare well with the ground truth data (Figure 11) with the location of the inner and outer subtidal bars accurately reproduced. Depth overestimation on the southern offshore edge results from wavenumber estimation in tiles with few pixels and high returned uncertainty. The large smoothing scale for the longshore direction used for interpolation of the field data does not enable a more detailed qualitative assessment concerning the shape of smaller bathymetric features. Overall, cBathy predicts the bathymetry with an rms error equal to 0.54 m, while the bias is equal to 0.15 m.

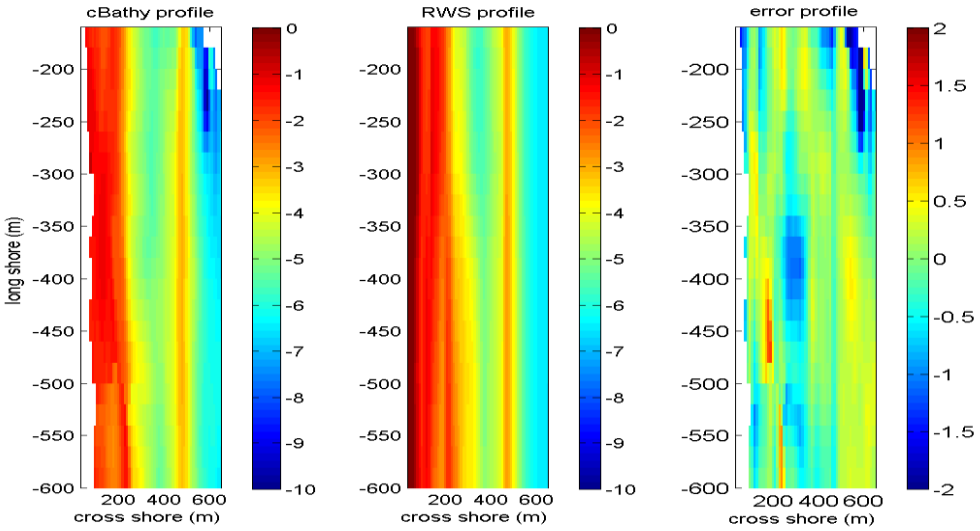

Figure 11. Comparison of cBathy hourly run of the 23rd October, 15:00:00 GMT (left panel) with the RWS measurements (middle panel) and the vertical difference map (right panel). Blue colors in the right panel stand for depth overestimation.

Figure 12 compares cBathy with the measured bathymetry at two longshore locations (y = -272 and y =-502 m) where only measured and not interpolated values are contained. The high accuracy of cBathy in the subtidal part is apparent for both transects. However, onshore of the inner subtidal bar the cBathy estimates start to deteriorate as the predicted bathymetric profile seems to obtain an anomalously flat pattern. Estimation of the skill returned during the nonlinear fitting process of phase 1 for the two longshore location at y=-270 and y =-500 m and for the cross shore range that estimated profile is flat, x≤120 and x≤160 m, results in mean values of 0.14 and 0.04 respectively. Further offshore the averaged skill increases to 0.64 and 0.3 respectively. Therefore, the very low skill indicates that predictions are not reliable; however, it is unclear what caused this error. Furthermore, the intertidal part is more susceptible to morphological changes due to wave action and thus comparison with measured bathymetry using a time window of ten days may be unreliable. However, recalculation of the error statistics excluding estimates onshore of 200 m does not significantly change the results.

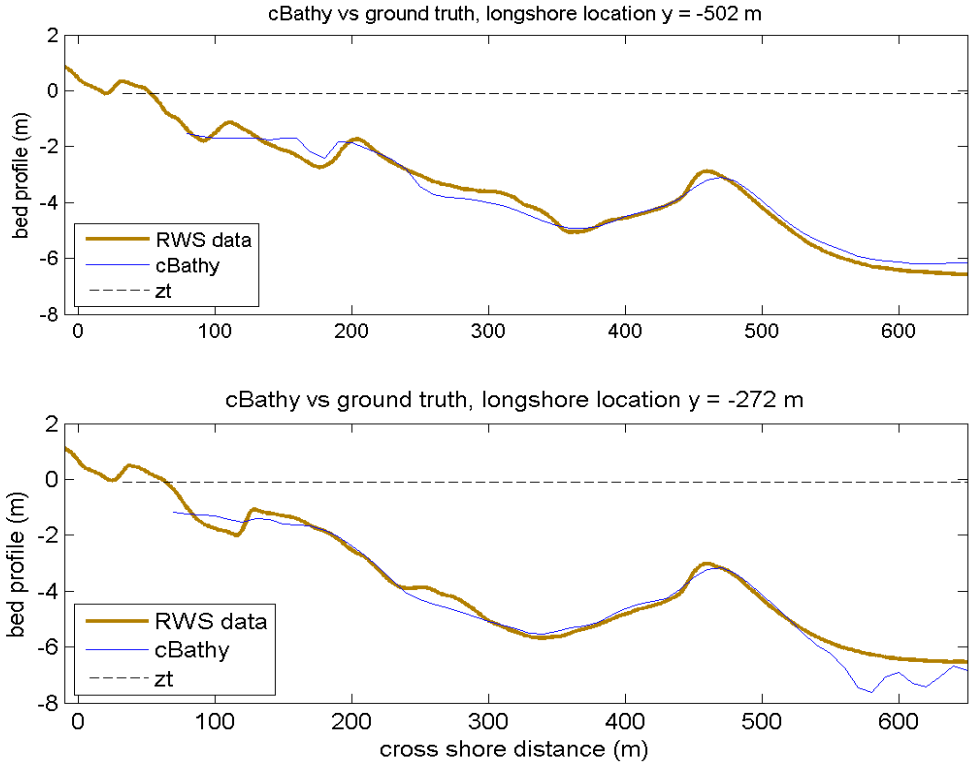

Figure 12. Comparison of cBathy (in blue) and RWS measurements (in brown) for two longshore positions. The dashed line shows the actual tidal level.

Subsequently, the cross shore and longshore distance between two analysis locations are varied between 8-25 m and 20-40 m, respectively. The smoothing scales Lx and Ly are again estimated as two times the analysis distance. No special dependence on varying analysis distance is revealed by the sensitivity analysis. This is illustrated in Figure 13. The rmse for varying dx_m but constant value for dy_m (dy_m=20 m, top panel) and varying dy_m but constant dx_m (dx_m =10 m, bottom panel) is in both cases between 0.6 and 0.8 m for x≥200 m. The shallower depth in the area considered is 1.7 m and hence a difference of twenty centimeters is rather insignificant. Because very large spacing causes a substantial decrease in the number of bathymetric estimates and the rest of the analysis is concentrated in the intertidal

zone where the spatial extend of measurements is limited, dx_m and dy_m were kept at their initial values.

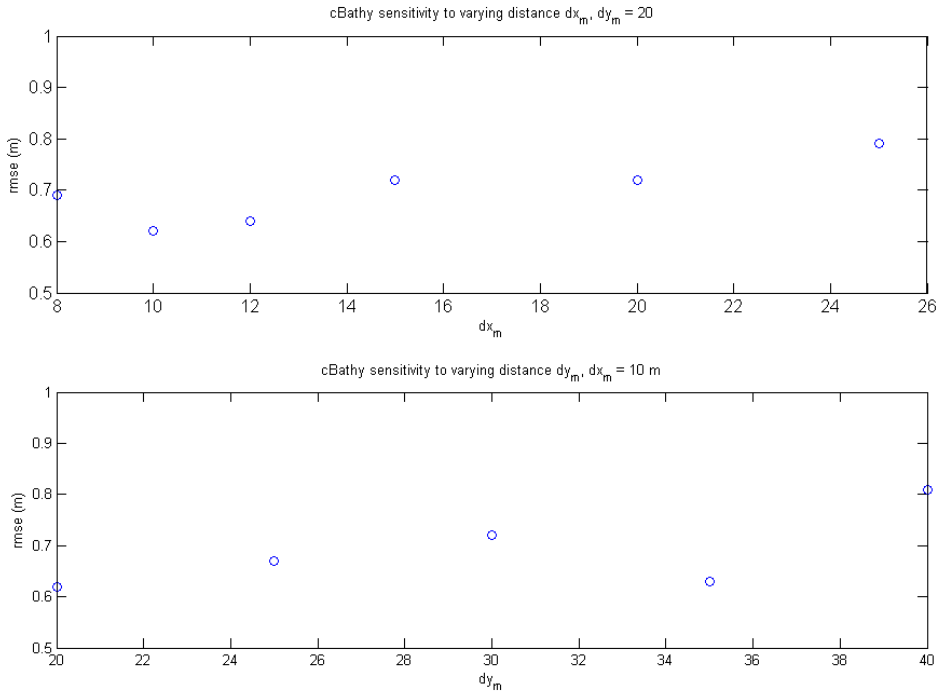

Figure 13. Root mean square error as a function of the distance between analysis locations in the cross shore (top panel) and longshore (bottom panel) direction.

4.2. Intertidal area

Due to the sparseness of the quad data both in time and space, the analysis focuses on the transect at the longshore location y = -272 m where measurements are available for every day and for the cross shore range 30 – 80 m. The cBathy results that correspond to y = -280 m are used for comparison as this is the nearest longshore location. It is assumed that an 8 m difference will not affect the accuracy of the comparisons. Error statistics are calculated using only cBathy hourly runs for when waves were resolvable over all the analysis locations ($30 \leq x_m \leq 80$ m), Therefore, the prerequisite to include an hourly run in the analysis is that the minimum measured water depth during the actual time was equal or higher than the cutoff value of 0.65 m (see Section 3.2). Out of entire dataset, thirty hourly cBathy runs, always during high tide, were found to satisfy this criterion and they were considered in the subsequent analysis.

4.2.1. Preliminary calculations

Comparison with the ground truth data for the 30 runs dataset yields rms error and bias equal to 1.14 m and -0.88 m respectively. The negative bias indicates depth overestimation. Figure 14 shows comparison between predictions and measurements for two hourly cBathy runs, 4 October 09:00:00 GMT and 5 October 09:00:00 GMT. Offshore H_{rms} was 0.83 m and 1.44 m respectively and waves could be seen to break in the considered area from the timex images. In both cases the water depth is overestimated by cBathy; the highest deviation occurs at the most offshore locations and is larger than 1 m. Further onshore, predictions are 30 – 40 cm deeper than the measurements. These errors are related with the onset of breaking and amplitude effects. This will be further elaborated in Section 4.3.

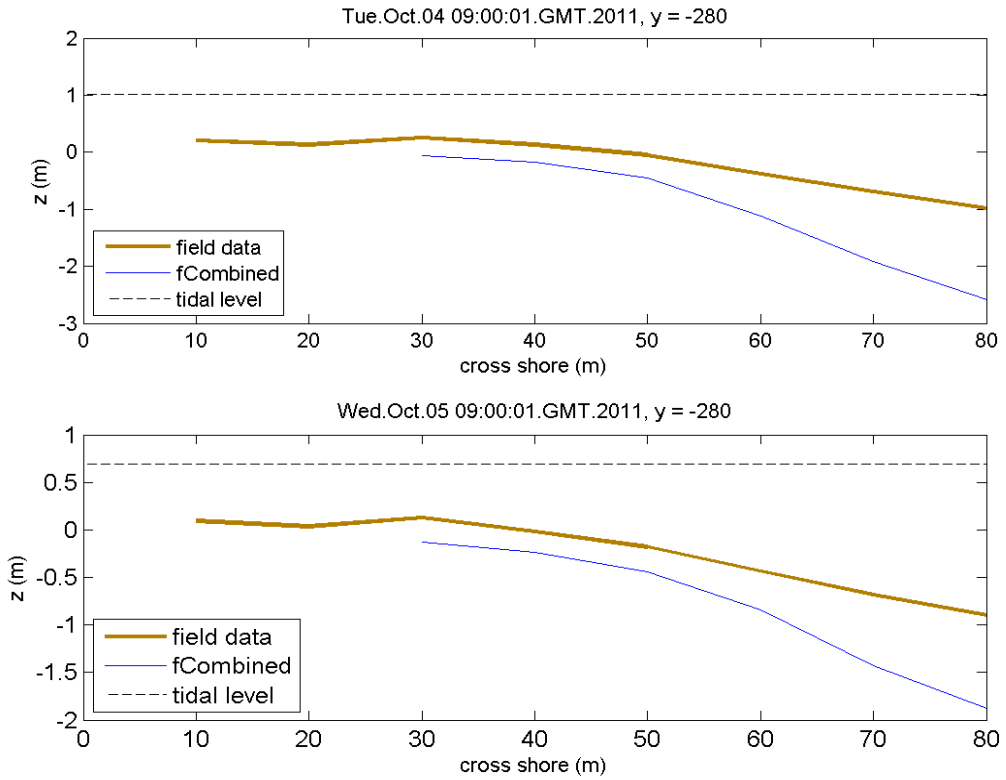

Figure 14. Measured and predicted bathymetries, 4 October, 09:00:00 GMT and 5 October 09:00:00 GMT.

4.2.2 Technical issues and data selection

Camera issues can result in poor quality of the image input data and lead to wavenumber and depth estimation errors. In this section such errors and their impact on the performance of cBathy hourly runs inside the intertidal zone are analyzed. The aim is to select cBathy runs which will be of relative merit for the celerity analysis.

Image quality depends on the weather conditions and can influence substantially the wavenumber estimation of phase 1. Raindrops in the camera and fog were apparent during the study period, mainly during stormy days. In addition, during such days foamy conditions due to extended wave breaking all over the intertidal zone also seem to cause a failure on the wavenumber and subsequent depth estimation during phase 1 due to low coherence in the signal. Another possible source of error under stormy conditions is the strong wind. While geometry solutions were always updated for these days, the 17 minutes duration of the pixel intensity time series is long enough to allow sharp changes of the camera orientation due to wind that would constitute the geometry solution not correct anymore.

The quality of the wavenumber and depth estimations can be assessed by looking at the error statistics. The confidence intervals $hErr$ that represent the uncertainty around each depth estimate appear to be consistently higher for days with offshore wave height around 2 m. Therefore, they may be used as an indicator of hourly runs with poor image quality. A threshold value of 1 m for the confidence interval was set as a criterion for rejecting hourly runs. The mean value of $hErr$ along the transect is found to exceed 1 m for fifteen cases that will be removed from celerity analysis. These large values correspond generally to offshore wave heights H_{rms} exceeding 1.7 m. Rms error and bias after the removal of those runs are 0.48 and 0.33 m.

Variance λ and skill s can also be used as indicators of reliable wavenumber estimation. λ expresses the amount of variance in the data explained by the first EOF over each tile and the skill indicates the goodness in the nonlinear fitting of the local phase data to the forward model (Eq. 2.25). Also, the percentage of phase 1 estimates that were not withdrawn from the subsequent cBathy analysis (s > 0.5 or λ > 10) is used for assessing the data quality. This last parameter will be called notNaN in the following. The mean values of skill, lamda and notNaN for the tiles over the transect are calculated and the characteristics of the six cases with the highest percentage of notNaN are shown in Table 2. Even with energetic conditions when waves of different frequencies and directions are mixed, reliable wavenumber estimates can be obtained. For example, the cBathy runs at 5 October 09:00:00 and 8 October 14:00:00, despite an offshore wave height of about 1.5 m returned a percentage of reliable frequency dependent estimates equal to 83% and 67% respectively. For the 5th of October, the skill and variance are also markedly high. The number of notNaN is maximized under lower waves, approaching almost 100% the 4 and 13 of October. The variance explained by the first EOF is maximal the 14th of October. It corresponds to near glassy sea conditions with long period propagating waves offering a coherent signal.

Table 2. Wave conditions and quality statistics for the 6 cBathy runs with the best statistics.

	Hrms (m)	Tmean (sec)	θ (°)	s	λ	notNaN %
4 Oct 09:00	0.84	4.5	-37.5	0.67	16.9	96
5 Oct 09:00	1.45	5.3	-32.8	0.74	20.7	83
8 Oct 14:00	1.54	7.1	69.5	0.6	16	67
13 Oct 15:00	0.63	7.9	80.8	0.76	21.5	83
13 Oct 16:00	0.50	7.5	78.2	0.78	25.52	96
14 Oct 16:00	0.30	7.2	-61.5	0.72	31.1	83

The runs depicted on Table 2 are the best candidates amongst the whole dataset for a more detailed celerity analysis mainly due to the high percentage of notNaN that maximizes the number of estimations that can be used. Because the main interest of the current study is on the impact of wave non linearities on the celerity estimation, it is preferable to consider hourly runs when the surf zone was well formed. From the six hourly runs of Table 2, the last three runs are characterised by very low waves and the one at the 8th of October has the lowest number of notNaN among all. Therefore, the two representative cases chosen for closer examination of the celerity spectra are the 4th of October 09:00:00 GMT and 5th of October 09:00:00 GMT.

4.2.3. Dependence on offshore wave conditions

The dependency of cBathy hourly results on the offshore wave conditions H_{rms}, T_{mean} and θ is analyzed in this section. cBathy rmse and bias are plotted against each of the parameters. The relationships are investigated before and after the removal of hourly runs with high *hErr*.

No clear dependence is found on the wave height for both cases (Figure 15). Rmse is very high for the stormiest days reaching up to 4.5 m revealing very poor performance of cBathy and very low for the calmest conditions with rmse equal to 0.11 m for very low waves (Hrms=0.2 m). However, no clear trend can be observed for wave heights between 0.4 and 2 m, for which rmse varies mostly between 0.3 and 1 m. This is mainly because error statistics for most of the days are estimated for surf zone conditions where the wave characteristics are locally controlled (*Thornton & Guza*, 1982) and independent of the offshore wave height.

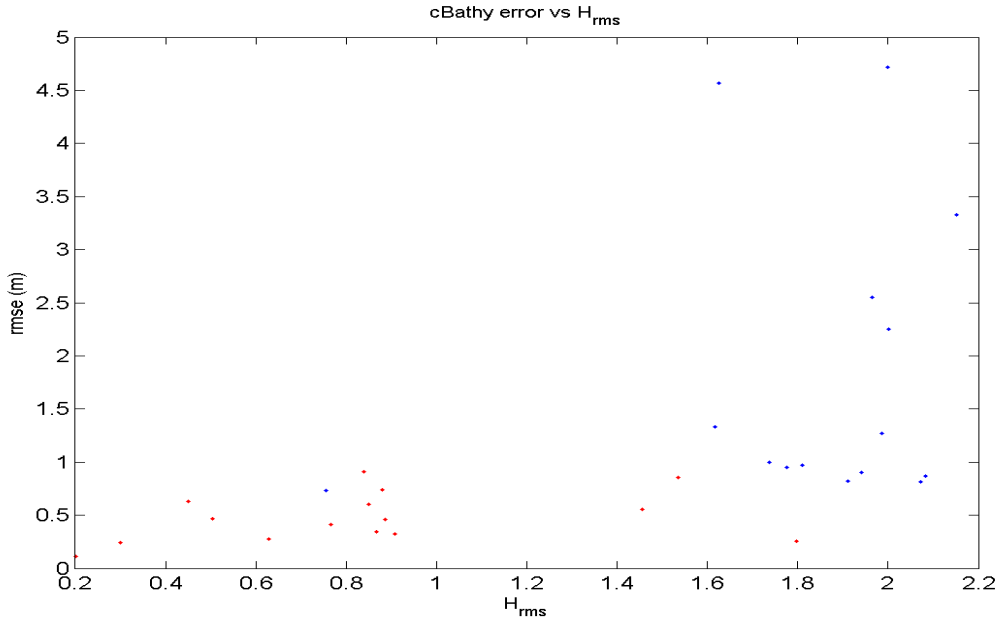

Figure 15. Offshore wave height versus cBathy rmse for the study period. Red colors correspond to the hourly runs with the low hErr.

Similarly no dependence is found for wave period suggesting that short waves can be resolved adequately by the collection scheme and give good estimates. About the angle of incidence, no relationship is found. It is expected that due to refraction waves inside the intertidal zone will always approach the coastline with direction close to shore normal and independently of the offshore wave angle. This is further manifested by the predictions of cBathy that give an average value of 14° for the angle of incidence onshore of 100 m.

4.3. Celerity analysis

This section is looking into the wave celerity estimations of cBathy inside the intertidal zone where wave nonlinearity can be pronounced. The aim is to test if the modeled values of celerity deviate from the linear wave theory and agree better with other predictors available in the literature (see Section 2.1.2). The 15 hourly cBathy runs that did not return wide confidence intervals are used for preliminary calculation of error statistics and using only the cBathy celerity estimations that originate from estimates with strong skill and eigenvector (λ). Analysis then is focusing on the two hourly runs chosen at Section 4.2.2. There are two main reasons for choosing some (two in this case) individual runs for closer examination: Firstly, it allows to study more in detail the spatial distribution of errors in both celerity and depth estimation with the possibility to refer back to the whole dataset to check if observed errors are systematic. Secondly, it enables to examine the evolution of wave celerity over the different frequencies in different locations in order to determine the importance of frequency and amplitude dispersion effects in cBathy hourly runs.

Calculations are performed for the longshore position that corresponds to the location of the instrument array (y = -280 m), where water depths and wave heights were measured. This array extends to 80 m offshore. The most offshore locations of the transect, between 60 and 80 m correspond to the toe of the intertidal bar. Further onshore, there is the crest of the sandbar with the seaward side at about x= 50 m and the shoreward side at around x = 30 m. The exact position in the nearshore zone depends on the wave conditions and the tidal level and thus it varies through time. Typically, the waves started to shoal and break at the toe of the bar and the

inner surf zone was formed on the bar crest. However, for the very quiet period 13 – 15 October waves started to break more onshore or did not break at all. During the two hourly runs that are further considered the wave height to water depth ratio for both cases was equal to 0.4 or higher, typical values of the surf zone (*Thornton & Guza*, 1982), for all the locations along the array except of the three most offshore locations on the first day. The local wave height is estimated as $Hrms$. The tidal level during the two runs is 1.02 m and 0.69 m respectively.

4.3.1. cBathy celerity

Celerity spectra were calculated with $c = \frac{2\pi f}{k}$ using the four pairs of $f - k$ returned by cBathy phase 1. Celerity using linear theory was also estimated for the whole range of frequency bins using the measured water depths. Wavenumber corresponding to each frequency is calculated using the approximations of *Guo* (2002). Furthermore, celerity was estimated with one wave model accounting for non-breaking waves (Solitary model), one for breaking waves (modified shallow water parameterization, $c = 1.3\sqrt{gh}$), and two composite models (KD86 and Booij model). The latter used the same wavenumber as linear theory for input. The wave heights used on the nonlinear predictors were derived with interpolation of the measured values of the local wave height H_{rms}. Inaccuracies of wave height resulted from interpolation have been found to have minor impact on depth inversion (*Catalan et al*, 2008).

There is some discrepancy between the cBathy modeled values and the predictions of linear theory. Overall, the mean rms error on celerity equals to 0.49 m/s while the mean bias is equal to -0.40 m/s suggesting that wave phase speed is underpredicted by linear theory. Although there is a considerable scatter, it can be seen that cBathy deviates from linear theory with increasing wave height (Figure 16).

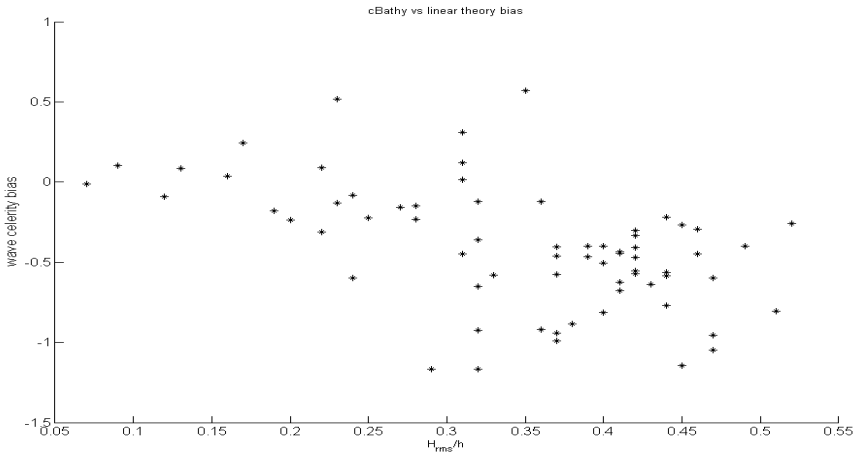

Figure 16. Bias between linear theory and cBathy celerity predictions as a function of the locally estimated relative wave height. Each point corresponds to the mean celerity bias for each tile and for each hourly run. The mean celerity bias for each tile equals to the deviation of linear theory predictions from the cBathy phase speeds averaged over the number of coherent frequencies that return notNaN for this tile.

Furthermore, wave energy spectra were calculated from the measured sea surface elevation time series enabling a more in depth examination. In all locations and for both days, peaks in the energy spectra correspond to the frequencies with the highest coherence. A nice example is illustrated in Figure 21 (upper panel) which shows the spectrum for the 5th of October at the most offshore location. In this figure, the well-defined peak is in perfect agreement with the cBathy coherent frequencies (Figure 20, lower panel) which are also characterised by a strong skill. Only exception with the

highest energy peaks not being correlated with the most coherent frequencies occurs at x = 30 m for the same day, when most of the wave energy was contained in frequencies lower than the cutoff value 0.1 Hz, around the infragravity band (f≈0.05, 0.07 Hz, see Figure 21, lower panel). Nevertheless, for the frequency band considered the third wave energy peak at around 0.11 Hz is in agreement with the two most coherent frequencies of cBathy (f = 0.1 & 0.12 Hz, see Figure 19, upper panel), so still consistent with the field observations.

Celerity predicted by linear theory at the most offshore locations decreases over the higher frequencies (> 0.2 Hz), consistent with dispersion effects. Dispersiveness is more pronounced at x = 70 and 80 m on the 4 October 09:00:00 when the water depth was bigger due to higher tidal level. More onshore, where the water depth is almost the same for x = 30-50 m, linear theory predictions do not change markedly over the frequencies. cBathy phase speed estimates seem to remain constant over the different frequencies in the majority of the locations where wave height to water depth ratio is higher than 0.4, indicating frequency non-dispersive waves. The fact that no estimates lie in frequencies higher than 0.22 Hz does not allow to conclude if cBathy celerity obtains a clear non-dispersive behavior or not. However, in both days modeled celerity deviates obviously from the linear theory predictions in all positions. Deviation of cBathy predictions from linear theory for these two runs is found to be weakly (5 October, 09:00:00 GMT) or even negatively correlated (4 October, 09:00:00 GMT) with increasing local wave height to water depth ratio (Figure 23). The largest deviations are observed at the most offshore locations for both days. cBathy wave phase speed is for instance about 1.3 times larger than the linear theory predictions at x=80 m on the 4th of October, despite the moderate value of H_{rms}/h (≈0.3). This results in large depth overprediction at the most offshore analysis tiles (Table 3). This can partly explain the scatter in Figure where the most negative values of bias do not correspond to the highest relative wave heights but to values of about 0.3 m.

Table 3. Bathymetric error (prediction – ground truth) for each location for the two hourly runs

Day/tile	30 m	40 m	50 m	60 m	70 m	80 m
4 Oct 09:00	-0.31 m	-0,30 m	-0.40 m	-0.75 m	-1.22 m	-1.60 m
5 Oct 09:00	-0.26 m	-0.22 m	-0.26 m	-0.41 m	-0.75 m	-0.97 m

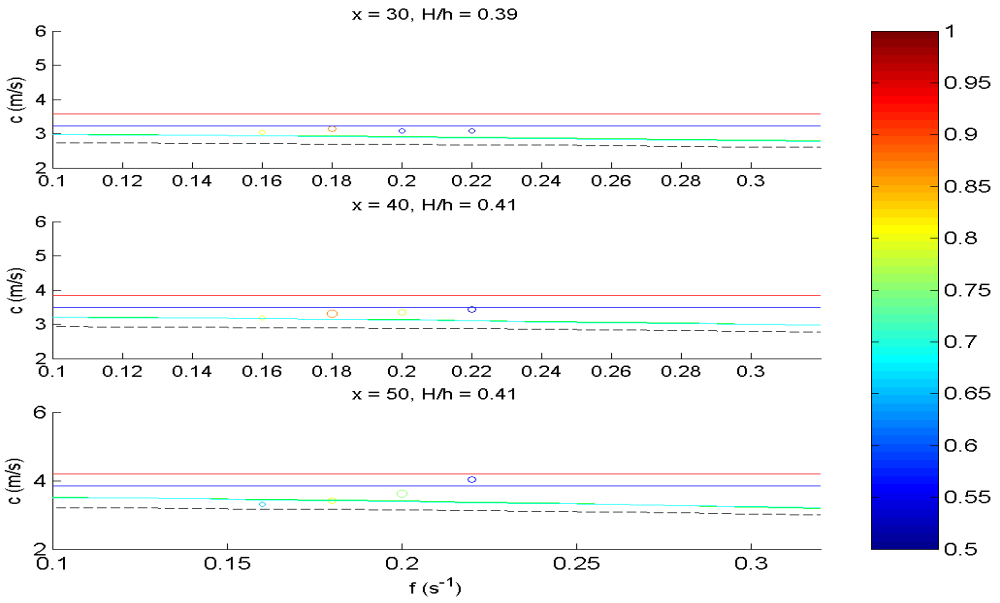

Figure 17. Wave celerity spectra for different cross shore locations 30-50 m, 4 October 09:00:00 GMT. The circles corresponds to cBathy predictions that passed phase 1, with the size of the circle to represent the λ and the color the skill (see colorbar). The black dashed line represent linear theory prediction, the green and cyan lines the Booij and KD86 models respectively, the red line the modified shallow water approximation and the blue line the solitary model. The same applies to figures Figure -20.

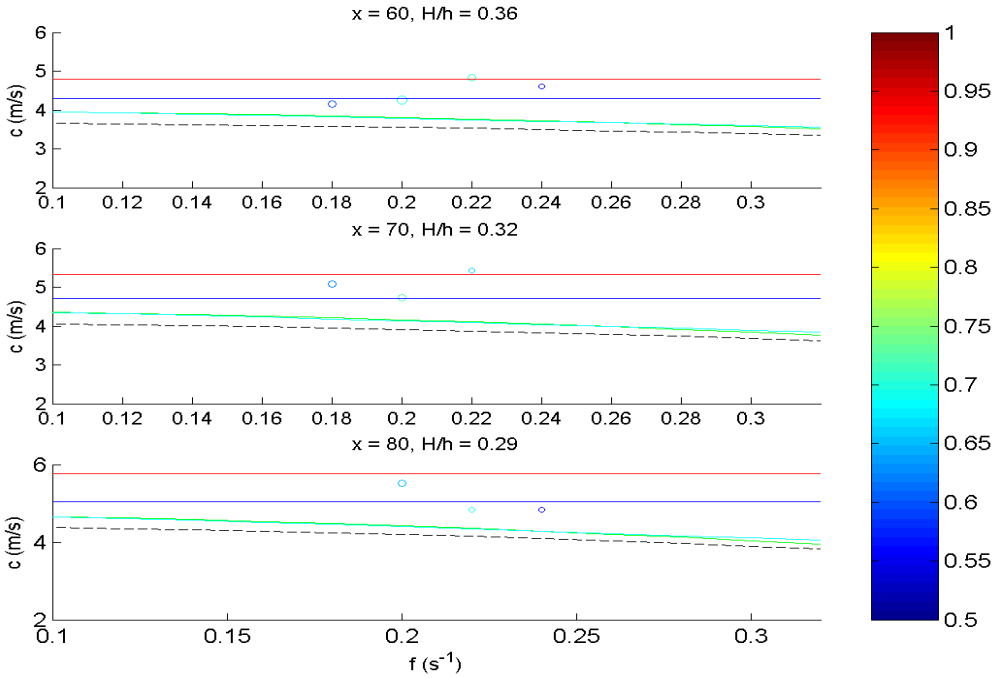

Figure 18. Wave celerity spectra for different cross shore locations 60-80 m 04 October 09:00:00.

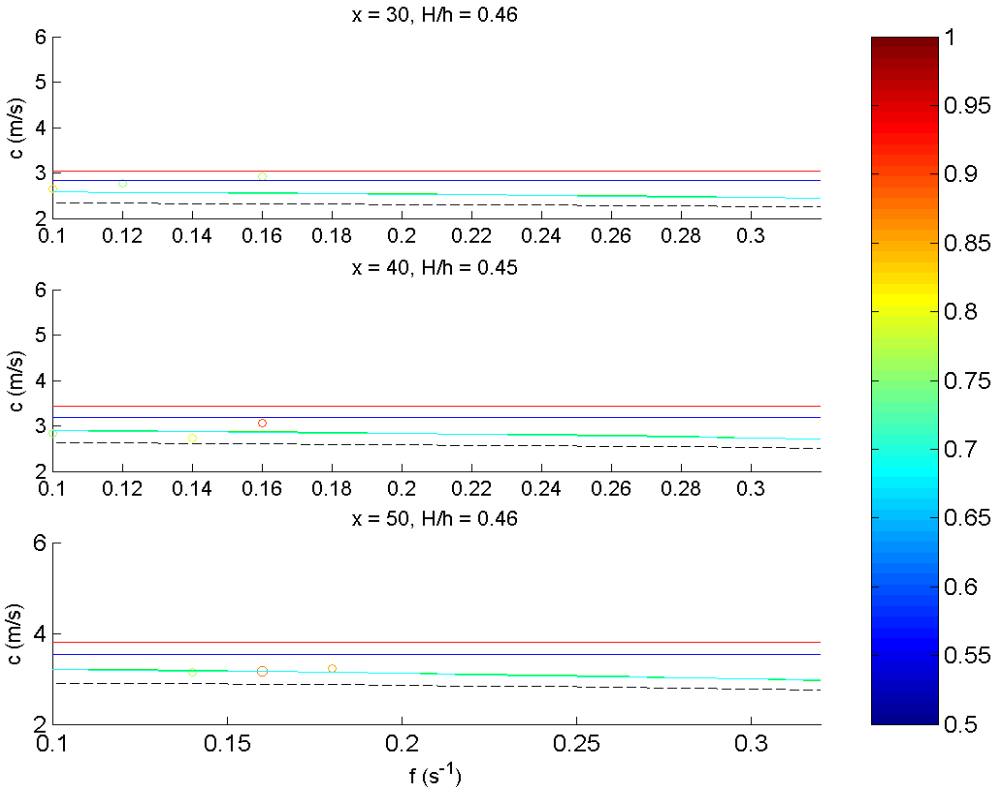

Figure 19. Wave celerity spectra for different cross shore locations 30 – 50 m, 05 October 09:00:00.

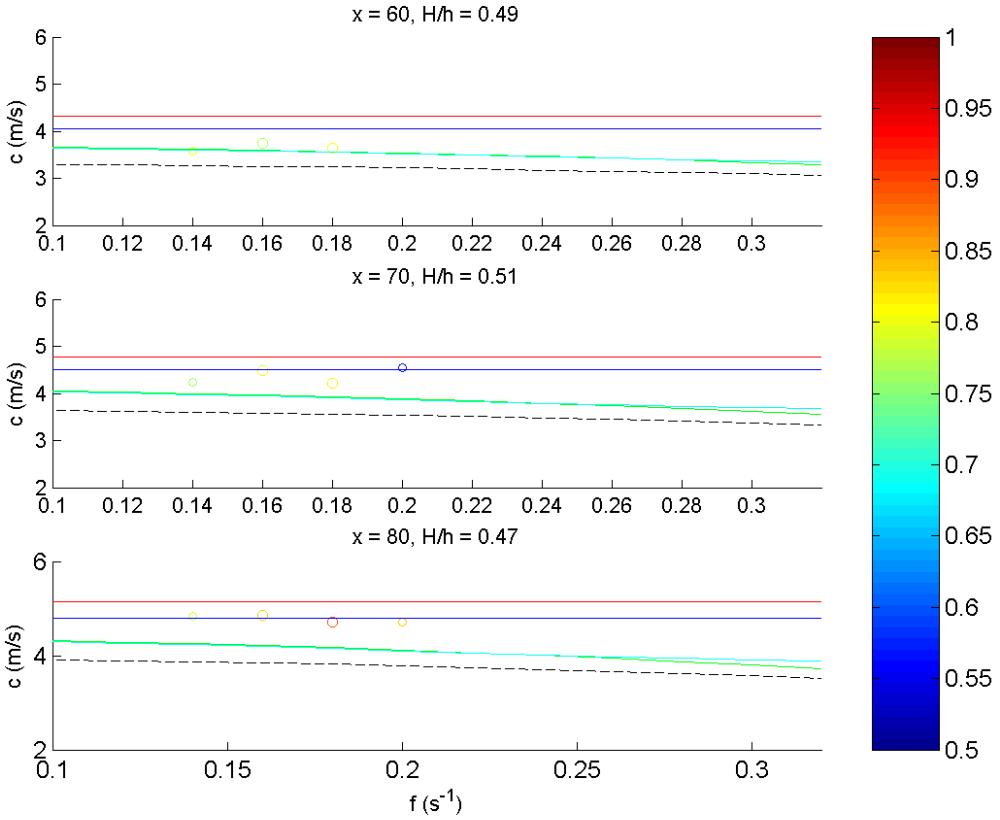

Figure 20. Wave celerity spectra for different cross shore locations 60-80 m 05 October 09:00:00.

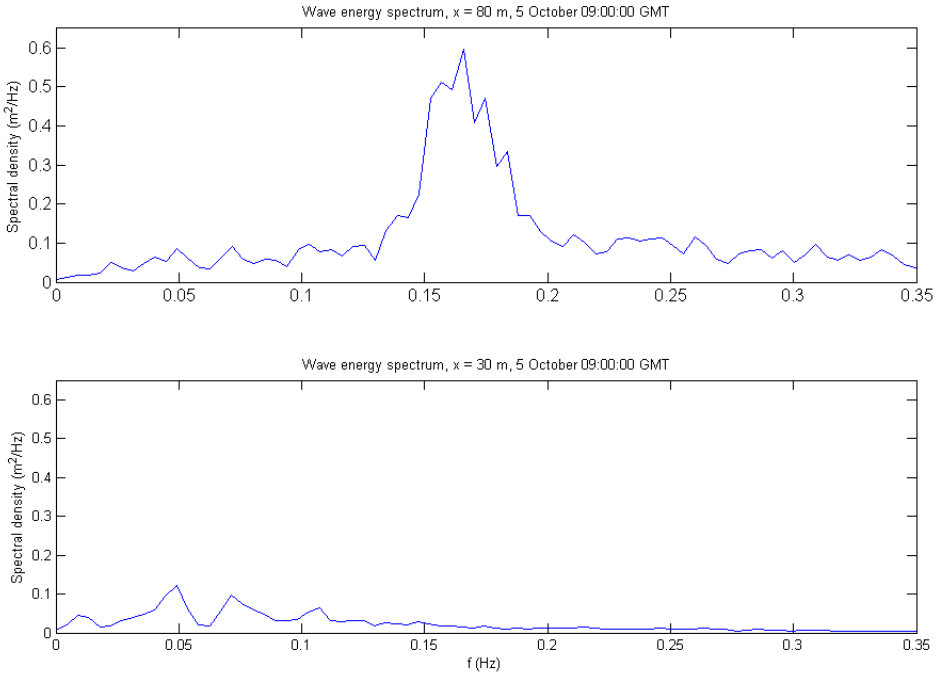

Figure 21. Wave energy spectra at x = 80 m (above) and x = 30 m (below) calculated from the measured sea-surface elevation time-series, 5 October 09:00:00 GMT.

Figure 22 shows that, in both cBathy runs, a localized peak of wave celerity around 80 m can be observed. It corresponds to the location where the pixel intensity starts increasing sharply. In general, higher pixel intensity corresponds to foamy conditions due to wave breaking. Looking at the time exposure images for both days (Figure 24-Figure 25), it can be seen that those tiles with the biggest depth overestimation (x = 60-80 m for the first run and x = 70-80 for the second, see Table 3) span the transition zone from wave non-breaking to wave breaking. The transition zone is identified at the intersection of the relatively dark colors of the non-breakers with the white colors of breaking waves. Similar discrepancies in celerity and depth estimations are found also in both other longshore positions and other hourly runs (shown in Appendix, A.1.1 – A.1.2), revealing hence a systematic error on the onset of breaking. At this point, wave celerity is difficult to be modeled by cBathy because of two reasons.

Firstly, at the moment of wave breaking the wave crest front surface is overturned causing a large shift in the phase of the crest. As a consequence, waves experience celerities higher than the linear theory (*Yoo*, 2007). Secondly, when optical signals from breaking and nonbreaking waves are mixed strong gradients in the MTF are caused (*Stockdon & Holman*, 2000) and the coherence of the signal is decreased. Intensity maxima shifts from the mildly slope back faces of waves to the steep front faces. This can result in erroneously low estimations of the wavenumber (*Almar et al*, 2008) and subsequent depth overprediction.

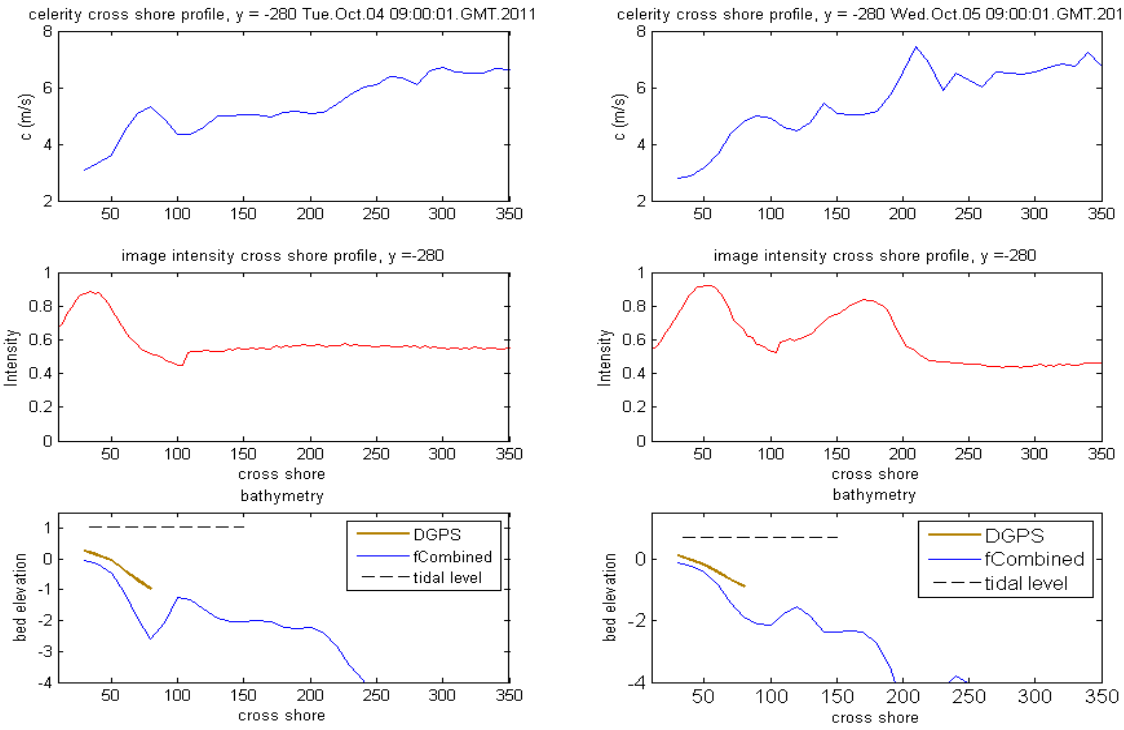

Figure 22. Cross shore profiles of celerity (top panels), pixel intensity (middle panels) and bathymetry (bottom panels) for 4 October 09:00 (left) and 5 October 09:00 (right). The values of celerity correspond to the mean value of celerity for each analysis tile (average of the estimates with skill and lamda above the threshold values). The pixel intensity is extracted from the time exposure images for y = -280 m.

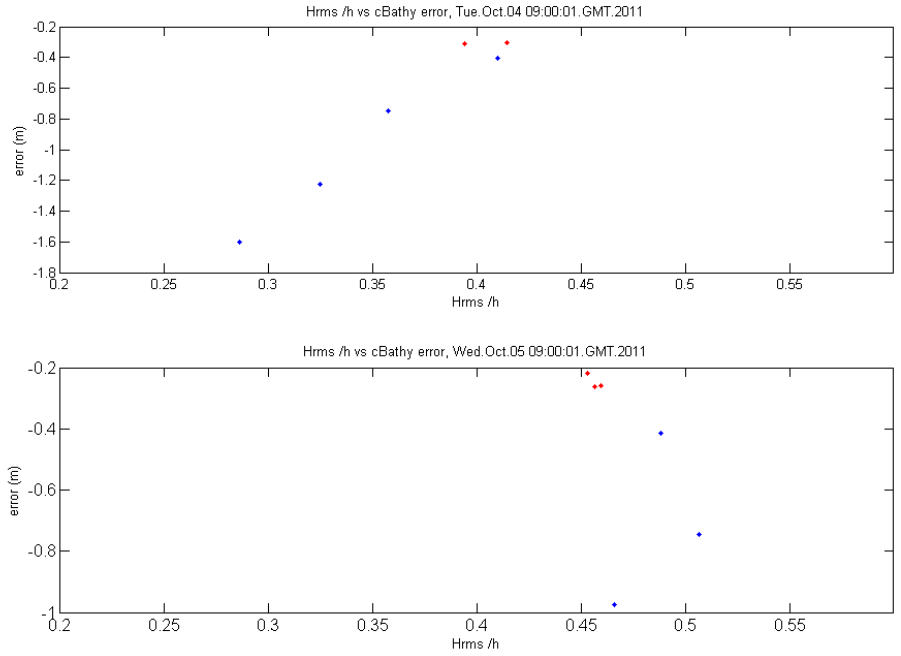

Figure 23. Bathymetric error at each tile, calculated as the vertical difference between prediction and ground truth, plotted against the local relative wave height for the 4 and 5 of October 09:00:00 GMT. The red points correspond to the cross shore locations that belong to the inner surf zone.

In order to investigate the influence of amplitude effects on the celerity estimation, it is necessary to identify the locations that belong to the inner surf zone and are not

influenced by the anomalies associated with the onset of breaking. The offshore edge of the inner surf zone is set as the intersection of dark and white pixels, as described above. Estimating the exact location of this limit may be possible with the application of existing color detection models (e.g. *Aarninkhof et al*, 2003); however this is far beyond the scope of the current research. As an alternative, visual inspection was used to determine the edge of the inner surf zone for each hourly run. Analysis tiles were considered to belong inside the inner surf zone only when their offshore edges lie totally inside the foamy part in the time exposure images. For both days, one analysis tile (at x = 50 and 60 m respectively) was found to have its major part inside the inner surf zone but its offshore boundaries were still outside. To be consistent with the method of how to define inner surf zone tiles, it was decided to exclude those two tiles.

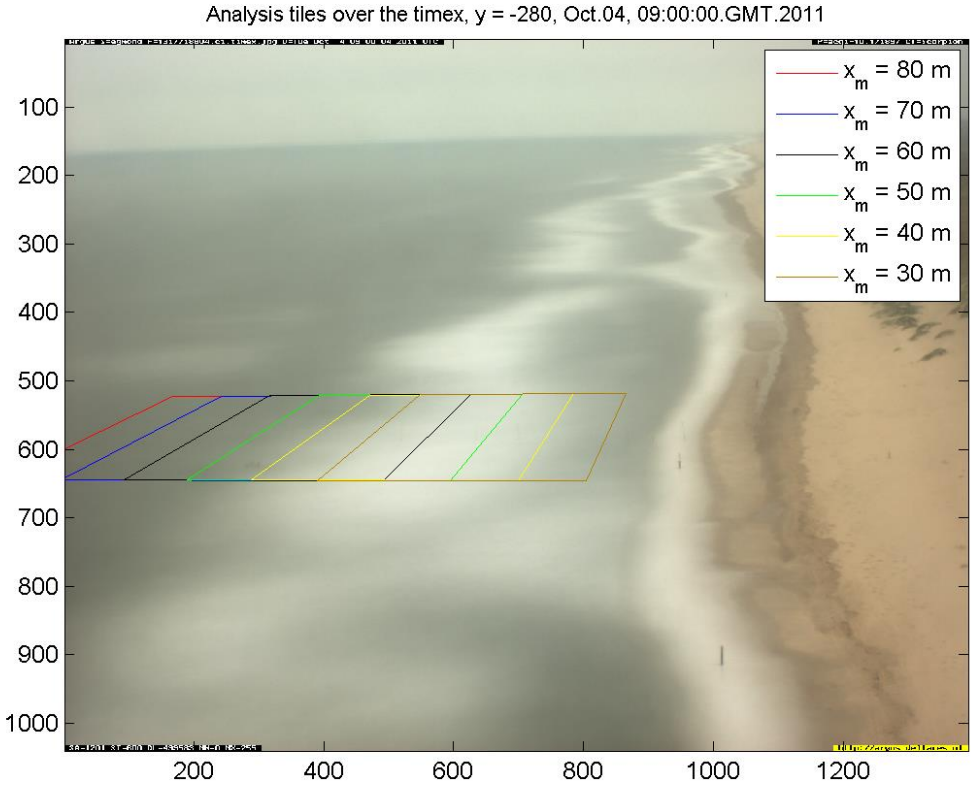

Figure 24. Analysis tiles at y = -280 m, plotted over the timex image (4 October 09:00:00 GMT) in order to identify the ones that lie inside the saturated surf zone. The entries in the legend correspond to the center (x_m) of each tile. The tiles are overlapped and cross shore spacing between two lines is 10 m, thus each tile in the figure includes five lines (L_x = 20 m). The same applies to Figure 25. The position of the tile corresponding to x_m = 50 m (green) is difficult to be determined, because while its major part is spanning the white band (broken waves) its offshore edges are still outside of it. It was determined to consider it outside the inner surf zone.

In the tiles that lie inside the inner surf zone cBathy predicts celerity 13% higher than linear theory. Figure plots the errors in the bathymetric prediction against the relative wave height. For the analysis points inside the inner surf zone (shown with red dots), some dependence is found for the second day; the small range of considered relative wave height does not allow such a relationship to be shown for the first day. Magnitude of errors in the two analysis tiles that they were excluded from the inner surf zone although their major part was spanning it, was found to be closer

to inner surf zone errors (~ 0.4 m) than to the ones on the onset of breaking. Overall, although no strong relationship between celerity and depth errors and increasing relative wave height was found, the fact that for both days predicted celerity is constantly higher than linear theory's predictions in locations with pronounced nonlinearities may be attributed to amplitude effects not modeled by linear theory.

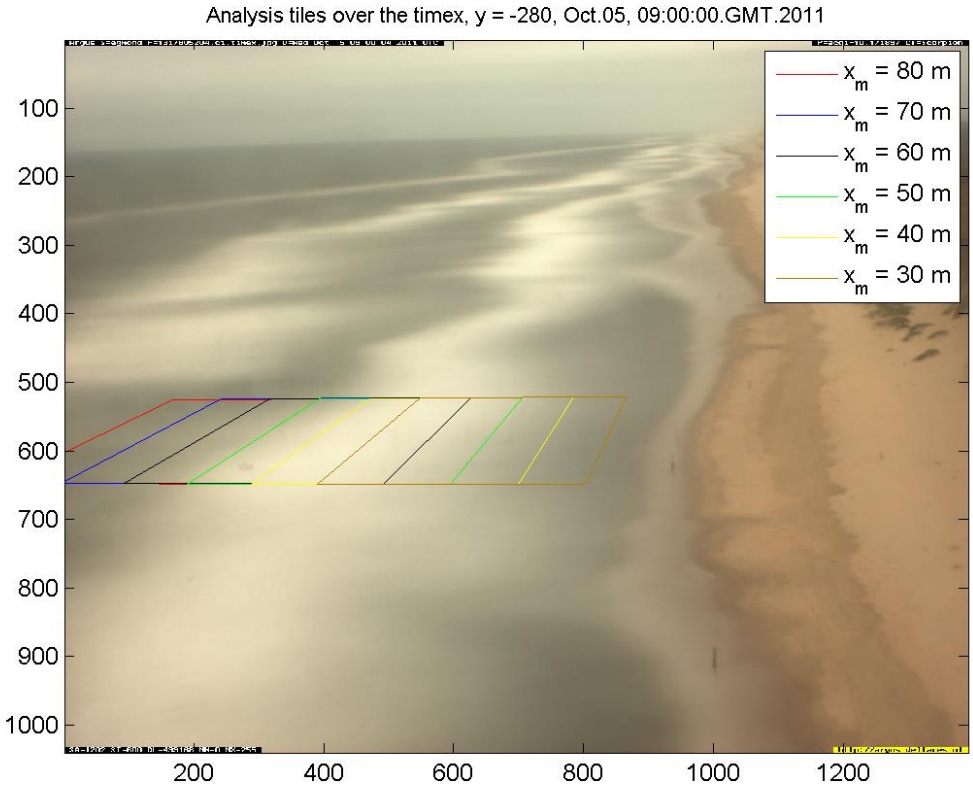

Figure 25. Analysis tiles at y = -280 m, plotted over the timex image (5 October 09:00:00 GMT) in order to identify the ones that lie inside the saturated surf zone. Similarly to Figure 25, difficulty in determining the exact position of the tile is encountered for xm = 60 (black) which is finally considered outside the inner surf zone.

4.3.2. Celerity predictors

Error statistics for the 15 hourly runs with low *hErr* were calculated also for the different nonlinear predictors and they are shown in Table 4. The Booij model is almost indistinguishable from the KD86 model and thus it is not shown in the following. The solitary and the composite model have an equal rms error and the same magnitude of bias; however the negative bias of KD86 states that it predicts celerity lower than the cBathy estimate. The modified shallow water parameterization highly overestimates the wave celerity.

Table 5 shows the two hourly runs at 4 and 5 of October 09:00:00 GMT. The solitary model performs better among the different predictors with a mean rms error and bias of 0.30 m/s and 0.12 m/s respectively. Concerning the behavior of each predictor in the spatial scale, it can be seen that the solitary model matches almost perfectly the cBathy predictions at the onset of breaking for both days (Figure 18 and Figure 20).

Table 4. Celerity predictors compared with cBathy celerity. Error statistics are calculated for the 15 hourly runs. The most right column shows the ratio between the cBathy and celerity predictor phase speed.

Model/statistics	Rms error (m/s)	Bias (m/s)	c_{Cb}/c_{pred}
Linear theory	0.49	-0.41	1.13
Solitary model	0.34	0.20	0.95
KD86	0.34	-0.19	1.05
Modified shallow water	0.72	0.68	0.84

For the same locations, the modified shallow water model mostly results in higher values while the composite model is even 25% lower than the modeled values. Inside the saturated surf zone, the composite model matches better with the cBathy celerities, especially for the second day when at some locations is found to be in perfect agreement with them (Figure 19, x = 50). Solitary model tends to slightly overpredict the wave phase speed in the same locations and the modified shallow water model results in systematically much higher values. In the two locations where it was difficult to determine their exact position in the nearshore zone the composite model is also in better agreement with cBathy especially for frequencies with high returned skill, matching perfectly at x = 60 m for the second day (Figure 20).

Table 5. Celerity predictors compared with cBathy for 4 and 5 October 09:00:00 GMT.

/time	4 October 09:00:00 GMT		5 October 09:00:00 GMT	
Model/statistics	Rms (m/s)	Bias (m/s)	Rms (m/s)	Bias (m/s)
Linear	0.80	-0.74	0.54	-0.53
Solitary	0.36	-0.04	0.24	0.20
KD86	0.60	-0.53	0.27	-0.23
Modified shallow	0.53	0.43	0.48	0.49

4.4. Depth inversion based on non-linear celerity predictors

Following *Holland* (2001), accounting for amplitude effects in locations where nonlinearities were predominant is expected to improve water depth estimates. The solitary and the KD86 composite models are implemented in the depth inversion solution of cBathy. The modified shallow water approximation is omitted as it resulted in celerity errors comparable in magnitude with linear theory.

For the 15 runs selected in 4.2.2, the solitary model performs the best; it results in an rms error of 0.31 m and bias of 0.12 m, with the latter to be a 20 cm improvement compared to linear theory. The composite model gives slightly less accurate results: it overestimates the water depth with an rms error of 0.39 m and a bias of -0.20 m.

A closer examination of the depth inversion results is again performed for the two hourly runs of 4 and 5 October 09:00:00 GMT (Figure 26 - Figure 27). As expected, each celerity predictor performs better in the locations where it was found to be closer to the celerity as estimated by cBathy. It was determined to include in the inner surf zone also the two tiles that their offshore edges were lying just outside the foamy part of wave breaking, as their celerity and bathymetric errors were more similar to those of the inner surf zone.

Inversion with the solitary model decreases substantially the error at the most offshore locations; inclusion of nonlinear effects in the depth inversion results in lower values of water depth yielding predictions almost identical to measurements at some locations (for example Figure 27 at x = 80 m). However, at these locations, the wave celerity is most probably overestimated by cBathy due to increasing gradients of pixel intensity originated from the onset of wave breaking. Further onshore, the use of the solitary model leads to a small underprediction of water depth. The highest inaccuracy in depth estimation is 22 cm for a measured water depth of 1.12 m, equivalent to a

19% underestimation (see Figure 27, x = 60 m). The mean bias inside the inner surf zone is 0.17 m.

The composite model gives also accurate depth estimates; predicted bathymetry deviates even less than 10 cm from the measurements. On average, KD86 inside the inner surf zone has a bias of -0.16 m, an improvement of 15 cm in the vertical compared to linear theory for considered water depths between 0.56 and 1.12 m. At the most offshore locations, however, magnitude of errors is similar to linear theory. Overall, the magnitude of bias of solitary and composite models inside the inner surf zone is equal, mainly because solitary model predicts the water depth very accurately at the most onshore location for both days.

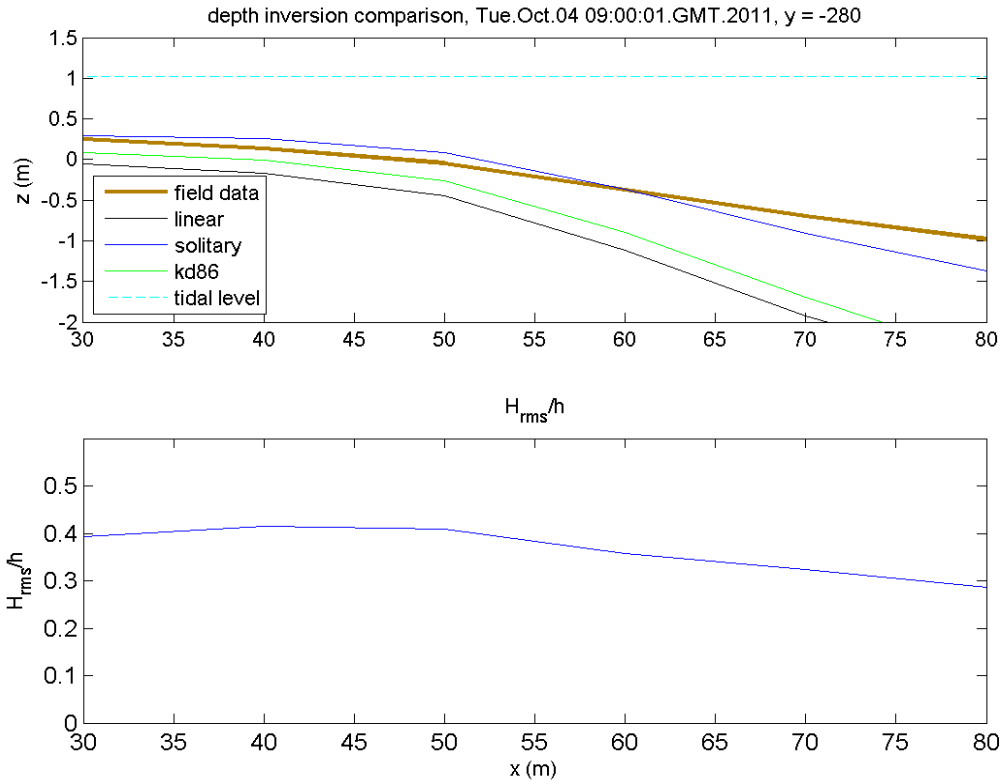

Figure 26. Depth inversion with linear theory and nonlinear predictors, 4 October, 09:00:00 GMT (upper panel) and cross shore profile of the relative wave height for the same locations. The legend in the upper panel indicates the colour which corresponds to each predictor.

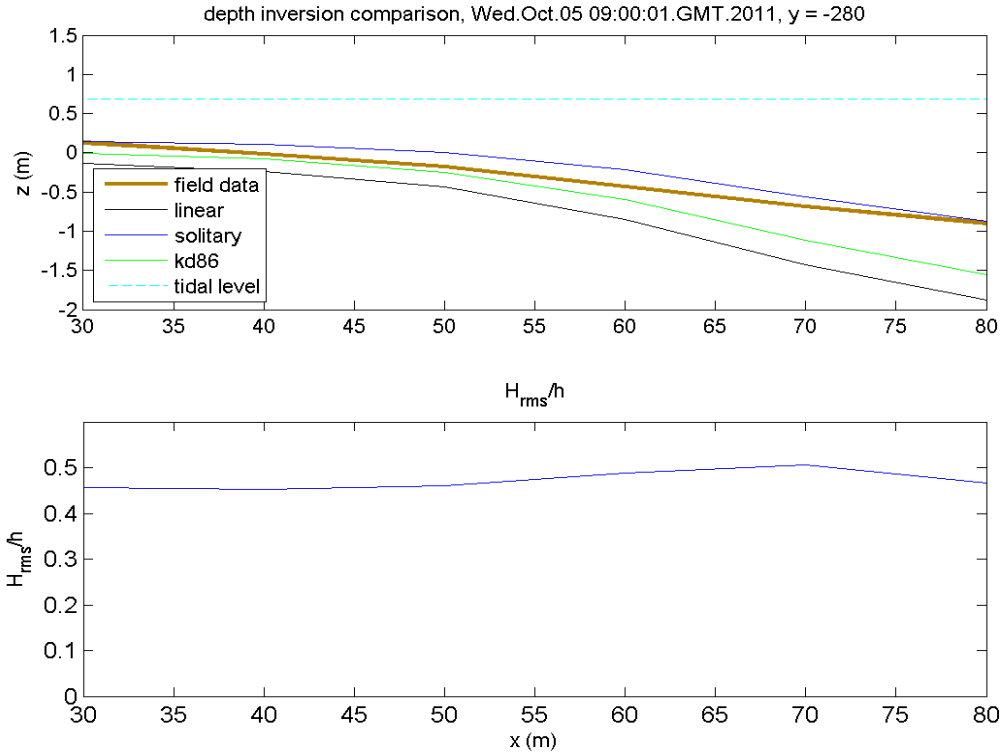

Figure 27. Depth inversion with linear theory and nonlinear predictors, 5 October, 09:00:00 GMT (upper panel) and cross shore profile of the relative wave height for the same locations. The legend in the upper panel indicates the colour which corresponds to each predictor.

5. Discussion

The performance of cBathy in Egmond is very good in the subtidal part and for relatively calm conditions (H_{rms} = 0.83 m). The pixel collection scheme, designed similarly to (*Wengrove et al*, 2013) is appropriate for resolving short waves with period even shorter than 4 seconds. Big errors in the wavenumber estimation occurred in the southern edge of the domain, because the analysis tiles there contained a small number of pixels that could not show a clear wave phase structure. However, they passed with little impact on the final depth estimation due to the multiple weighting processes during each cBathy hourly run.

An obstacle to the current study is that while the main interest is in stormy days when nonlinearities are pronounced, cBathy hourly results highly deteriorate during these conditions and the sensitivity to the exclusion of amplitude effects in the dispersion relationship cannot be studied. While previous studies about the importance of nonlinear effects in depth inversion were based on field measurements of wavenumbers (*Holland*, 2001) or on monochromatic waves where wavenumber is easily estimated from video data with the wave tracking technique (*Catalan & Haller*, 2008), the current work uses the video - derived wavenumbers of a real wave field with mutiple wave trains. Hence, the wave phase speed estimation may not be always accurate due to technical problems (e.g., low image quality). Camera issues associated with bad weather conditions make the wavenumber estimation of phase 1 difficult resulting in anomalously low wavenumbers (wavelengths as long as 70 m in 1 m water depth) and also a lot of gaps (low percentage of notNaN). As a consequence, water depth is highly overestimated with vertical differences of O(>1 m). By visual inspection it could be seen that cBathy is affected by these problems both in the whole domain (not shown here), however due to lack of field data quantitative analysis is not feasible for the offshore part. The error bars returned during phase 1 are found to be systematically high for such days. As they constitute reliable indicators of data quality (*Plant et al*, 2008, *Holman et al*, 2013) they can be used to detect those bad hourly runs and remove them from the subsequent analysis that is focusing on the celerity estimation.

Excluding bad hourly runs and focusing on the shallower and more dynamic environment of the intertidal area, the water depth in the intertidal area is found to be systematically overpredicted by the algorithm. Sources of error are found to differ spatially depending on the position in the nearshore zone – shoaling, outer or inner surf zone.The errors are grouped using visual inspection in time exposure images in order to determine the position of each analysis location in the nearshore. As each tile spanned a distance of at least 40 m in the cross shore, it is quite possible that signals from breaking and not breaking waves would be mixed. The main difficulty in classifying the tiles was encountered with tiles that their major part was spanning the white band of breaking waves but their offshore edges were still seaward of it. Although they were initially considered to be outside the inner surf zone, bathymetric and celerity errors have an order of magnitude similar to the errors inside the inner surf zone. This may be an indicator that such tiles are not affected by the problems on the onset of breaking.

Inside the inner (saturated) surf zone where nonlinearities are pronounced water depth was overestimated. No clear relationship is found with increasing relative wave height, maybe because of the small range of values of it. However, wave celerity was found to be systematically higher than linear theory in those locations, indicating that depth overestimation may come from the nonmodeling of amplitude effects in the dispersion relationship. Error statistics were recalculated only for the tiles that lie in the inner surf zone for the 15 hourly runs-dataset. The bathymetric bias is found to

be 0.22 m, 20 cm lower than the findings of *Holland* (2001). If the tiles that the major part of the signal is dominated by the wave breaking are also included, the bias is 0.42 m. A closer examination of two hourly runs with a high number of phase 1 reliable estimates shows that the KD86 model can lead to depth predictions very close to ground truth inside the inner surf zone if used in the depth inversion. The fact that it behaves similarly to the linear theory in deep water makes it more appropriate for being used in an analysis domain that will extend offshore of the surf zone.

The largest depth overpredictions occurs in tiles that span the breaker line (Figure 28). For the two hourly runs that offers sufficient number of celerity estimates, these overestimations are not correlated with increasing $Hrms/h$. Wave phase speed of cBathy is 25% higher than predicted by linear theory, leading to local depth overestimation of about two times the local water depth. In field studies, measured wave celerity on the onset of breaking has been found to be up to 68% higher than linear theory (*Yoo*, 2007). In addition, mixing of breakers and non breakers results in sharp gradients of the pixel intensity and decreases the coherence of the signal leading in celerity overprediction. Correlation between a localised peak in celerity estimation and a sharp increase in intensity was found also for most of the days (see Appendix A.1) and for other longshore locations (see Appendix A.2). It can be seen that the bathymetric profiles deepen unrealistically at the same locations; however, the deficiency of bathymetric data does not allow a quantitative analysis. This kind of errors is not uncommon in depth inversion studies (*Stockdon & Holman*, 2000, *Holman et al*, 2013).

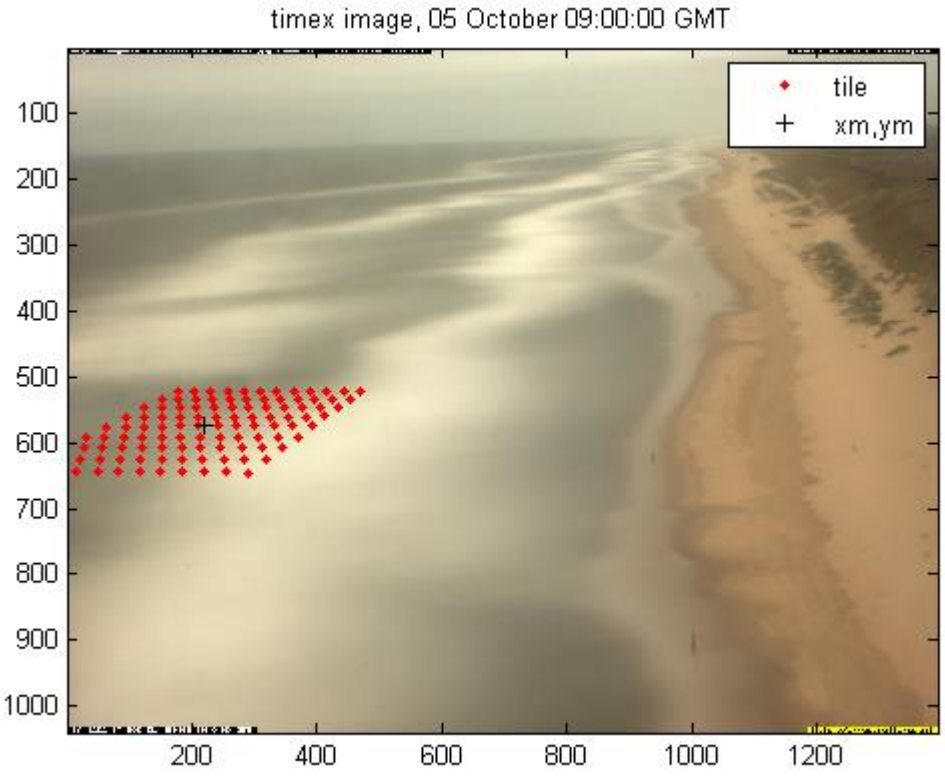

Figure 28. Analysis tile at x = 80 m and y=-280 m shown on top of the timex image for 5 October, 09:00:00 GMT. The rest of the tile's pixels in the upper left (if looking offshore from the beach) corner of the tile belong to the field of view of camera 2.

The solitary model prediction is found to be closer to cBathy values on the onset of breaking. This is in agreement with the findings of *Yoo* (2007), who already suggested that solitary theory predicts more accurately wave celerity at the onset of

breaking. Depth inversion using the solitary model also leads to predictions very close to ground truth values; however, the dependence of the solitary equation simply on the wave height and water depth hinders its application in depth inversion in locations where frequency dispersion is of importance.

The analysis tile at x = 80 is crossed by the boundary of the two cameras (red dots in Figure 28), something that can also lead to depth overprediction due to problems in the merging of the two cameras arisen from the geometry solutions. The depth overprediction seems to start more offshore at both days (Figure 22), at 100 m and 120 m respectively where the tiles are divided almost in two parts by the camera intersection. However, repetition of depth overprediction on the breaker line for more longshore positions indicates that the camera seam problem is of secondary importance, at least for the tile at y =-280 m where very few pixels lie on camera 2.

Although returned skill and explained variance are high on the onset of breaking for the two hourly runs considered, it is not certain that the algorithm has predicted the wave phase speed precisely due to the sharp gradients of the pixel intensity. Excluding these locations, linear theory underpredicts celerity with a bias of 0.39 m/s, i.e. predicts wave celerity about 20% lower than the cBathy values. The composite models predict wave celerity inside the surf zone more precisely, in agreement with previous celerity studies (*Catalan & Haller*, 2008). Overall, it gives an rmse of 0.19 m/s and bias -0.12 m/s, equivalent to a 6% underestimation. The simple forms of the solitary and modified shallow water model overpredict the wave celerity with rmse of 0.27 m/s and 0.55 m/s respectively. Celerity overprediction by the solitary and modified shallow water model is consistent with results of previous studies (*Catalan & Haller* (2008), *Tissier et al* (2011)).

cBathy was also run with a larger range of candidate frequencies (up to 0.5 Hz) and keeping 8 frequencies in order to check if wave celerity remains constant over the higher frequencies that correspond to deep water waves even inside the surf zone, similarly to the study of *Thornton & Guza* (1982). However, because high frequencies returned very weak skill and corresponded to anomalously high values of phase speed (>5 m/s) no clear conclusion could be made. On the other hand, the measured energy spectra at the most onshore locations revealed significant peaks at frequencies lower than the low frequency limit of the current settings and independently of the offshore period. This is an indication that lower wave frequencies can be hosted in the candidate frequencies and independently of the local wave climate. Running the algorithm with the low frequency limit set at 0.067 Hz resulted in the detection of such frequencies as the most coherent and with strong skill; however the bathymetric result did not change substantially. Similar results has been found also by *Plant et al* (2008) who suggested that low frequency wave motions offer well structured phase patterns and can be well resolved by the sampling design, oppositely to high frequencies.

It is important to assess the influence of each source of error in the final result. Image quality errors associated with stormy weather conditions generally lead to deterioration of the algorithm with vertical errors often higher than 1 m and maximum values around 7 m. In addition, depth overestimation with a typical order of magnitude of around 1 m occurs systematically on the onset of breaking. In the inner surf zone, vertical difference between predictions and ground truth is usually lower than 0.5 m. Overall, what appears from the analysis of the current dataset is that although accounting for amplitude effects can improve the hourly predictions in the shallow water, technical isssues affect hourly estimates more strongly.

The Kalman filter was run for the whole period and its performance is assessed through comparison with field data for three different days, the 5th, 9th and 14th of October. Concerning predictions with the linear theory, the Kalman filter generally

smoothes the bathymetry as it averages the estimates through different tidal cycles and wave conditions; however, in all three days, predictions are still deeper than measurements (Figure 29). The agreement with the in situ data at the most offshore part in the final day results from the last two relatively calm days when waves were not breaking during high tide enabling accurate wavenumber and depth estimation with low uncertainty. In total, mean values of rmse and bias for the three days are 0.42 m and -0.35 m, respectively. Running the Kalman filter with the solitary model results in an improvement of the predicted bathymetry. At the most onshore locations the model is in very good agreement for the first day (upper panel, Figure 29) and results in an improvement of even 23 cm for the other two days when compared with linear theory. Nevertheless, the predictions remain deeper than the measurements (middle and lower panel, Figure 29). In addition, the solitary model leads to better bathymetry estimates compared to linear theory at the most offshore locations that correspond to the onset of breaking. The composite model gives similar results with the solitary model for the onshore locations ($x \leq 60$ m) but highly deteriorates on the most offshore locations on the last day giving worse predictions than linear theory. This depth overestimation is caused by erroneously deep estimates that return very low uncertainty having an impact on the Kalman filter. However, it is not clear why returned confidence intervals with the kd86 model were narrower than with linear theory. The error statistics for the three runs are shown in Table 6. Overall, the Kalman filter is proved to be capable of alleviating the errors associated with the onset of breaking, although an eleven days period was required for stable estimates due to stormy conditions.

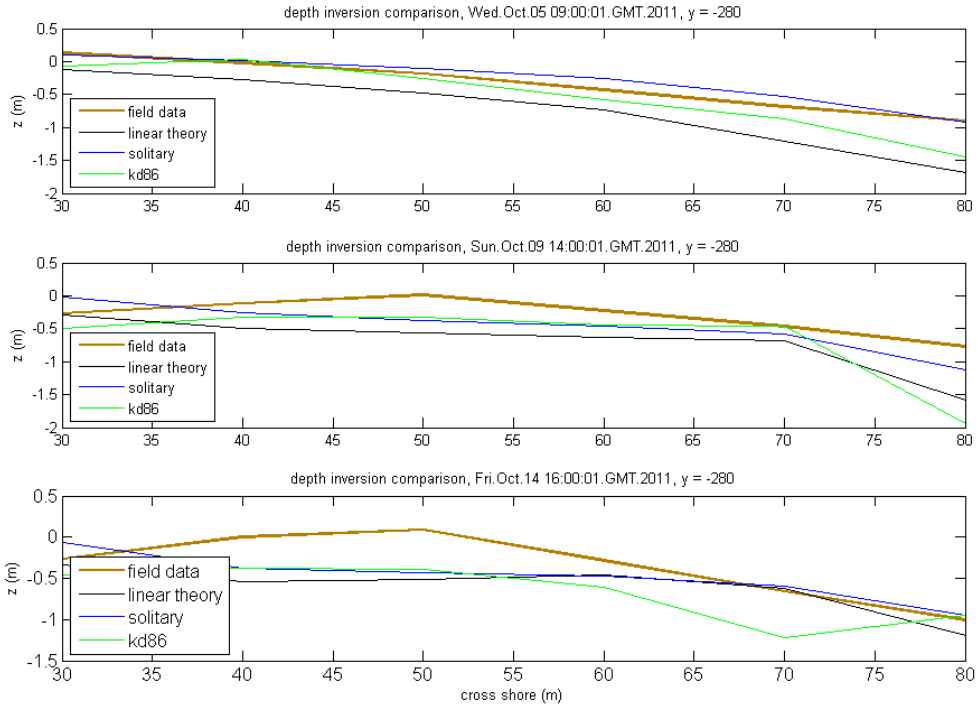

Figure 29. Kalman filter bathymetry using linear theory (black), solitary (blue) and kd86 (green) model compared with field data (brown) for three different days.

Table 6. Error statistics of running Average bathymetry for three different celerity predictors and when compared with field data of three different survey days.

Model / Day	05 October		09 October		14 October	
	rmse	bias	rmse	bias	rmse	bias
Solitary	0.10 m	0.06 m	0.26m	-0.16 m	0.34 m	-0.12 m
KD86	0.26 m	-0.18 m	0.52 m	-0.36 m	0.37 m	-0. 31 m
Linear Theory	0.44 m	-0.40 m	0.47 m	-0.40 m	0.34 m	-0.26 m

A major limitation of the current work is the lack of field data for validation both in the cross shore and long shore direction. Bathymetric estimations on the onset of breaking appear a sudden drop usually offshore of 80 m, thus an extended cross shore profile will offer a better insight on how the cBathy estimates are affected by the initiation of wave breaking. In addition, offshore of 80 m and for the considered longshore position the camera seam problem is also expected to be higher. The sensitivity of the algorithm to this possible source of errors could also be tested. Measurements of bathymetry that extend more offshore in more than one longshore positions would also allow to check if errors inside the intertidal zone are systematic enabling a more detailed assessment of the cBathy outputs.

Concerning the celerity analysis, the main limitation is that there are not any ground truth data of wave phase speed but the cBathy modeled values are used instead. *Plant et al* (2008) compared modeled values of wavenumber with measured values and found them to be in very good agreement. However, the onset of breaking remains a point where wave phase speed is often overestimated by video techniques and thus a direct comparison with field data would enable to quantify more accurately the errors in this location.

A future study in which a more extensive bathymetric dataset will be available is recommended. Once a bathymetric map is available, it can be used as a boundary to numerical models (for example, *van Ormondt et al* (2012)) to produce a wave height grid for applying depth inversion with nonlinear effects also in the offshore part. It is expected that the composite model KD86 will be appropriate for deep water regimes as it can model both frequency and amplitude dispersion effects.

6. Conclusions

The recently developed cBathy depth inversion algorithm, which is capable of predicting the nearshore bathymetry using video data, was applied to the Dutch beach of Egmond aan Zee. Bathymetric predictions compared well with measurements for the subtidal zone (200≤x≤650 m, h>2 m) with an rms error 0f 0.54 m and a bias of 0.15 m, that is to say a slight underprediction of water depth. The designed pixel sampling scheme was capable of resolving the short period waves of the Dutch coast. A sensitivity analysis showed no special trend for varying distances between analysis locations.

The performance of the algorithm was more closely examined inside the intertidal part where for the majority of the days considered typical surf zone conditions were apparent. The algorithm was found to highly degrade during stormy days with errors O (>1 m). The confidence intervals returned by the algorithm for each estimated property were used to identify the runs with unreliable cBathy estimates, which were removed from the subsequent analysis. For the remaining fifteen hourly runs, cBathy overpredicted the measured intertidal bathymetry yielding an rms error of 0.48 m and a bias of 0.33 m.

A study of the celerity outputs of the algorithm for two individual runs showed that errors came from two sources. In the inner surf zone where waves were well breaking as indicated by the timex images the predictions of cBathy is always higher than the ones of linear theory, manifesting hence that exclusion of amplitude effects in the dispersion relationship affects the accuracy of depth inversion. Errors in the predicted bathymetry inside the inner surf zone for the whole dataset had a bias of 0.22 m. The second source of error is associated with the onset of breaking, where waves have been found to travel faster than linear predictions and they are difficult to be modeled. In addition, in this location signals from breaking and nonbreaking waves are mixed and cause abrupt changes in the pixel intensity profile hindering the wavenumber estimation. Errors are found to be of greater significance compared to amplitude effects as vertical differences were found to be even higher than 1 m, almost two times the real bathymetry. The Kalman filter of the algorithm needed a relatively long period (11 days) to smooth the bathymetry at the breaking point, primarily because wave breaking was apparent at this location for most of the days.

Different nonlinear predictors were tested and compared with the modeled values of celerity. Overall, the two composite models KD86 and *Booij* (1981) that model both amplitude and frequency dispersion showed the best agreement inside the inner surf zone. The two models were almost indistinguishable, with predictions 6% lower than the cBathy wave phase speed for two hourly cBathy runs with reliable wavenumber estimates. The composite models degraded on the onset of breaking. There, solitary model was found to match better with the modeled phase speeds. The modification of the linear theory shallow water approximation $c = 1.3\sqrt{gh}$ and the solitary model overpredicted the wave celerity in the inner surf zone 18% and 9% respectively.

In the subsequent depth inversion the solitary and the KD86 model were tested. In total of fifteen hourly runs the solitary model resulted in rms error of 0.31 m and bias of 0.12 m. Predictions with the KD86 model overpredicted the water depth with an rms error of 0.39 m and a bias of -0.2 m. A closer examination performed for two hourly runs revealed that the solitary model improved substantially the predictions on the onset of breaking matching very well with ground truth data and underpredicted the water depth in the inner surf zone with a bias of 0.17 m. For the composite model, the bias inside the surf zone was -0.16 m with hourly results to be at times very close to ground truth (O(<10 cm)). It is expected that a composite model is

more suitable for future applications as it can model both frequency and amplitude dispersion effects.

7. References

Aarninkhof, S., Morelissen, R., Cohen, A. "The Argus Runtime Environment: Guidelines on installation and use." 2007.

Almar, R., Bonneton, P., Senechal., N., Roelvink., D. "Wave celerity from video imaging: A new method." *ICCE 2008*. n.d.

Birkemeier, W. A., Mason, A. "The crab: a unique nearshore surveying vehicle." *Sur. Eng, vol 110* (1984): 1-7.

Bonneton, P. "Wave celerity in the surf zone." *29th Conference on Coastal Enginnering*. 2004. 392-401.

Booij, N. "Gravity waves on water with non-uniform bed and current." 1981.

Brinkkemper, J. *Modeling the cross shore evolution of asymmetry and skewness of surface propagating waves over a natural intertidal bar*. MSc thesis. Utrecht University, 2013.

Catalan, P., Haller, M.,. "Remote sensing of breaking wave phase speeds with application to non-linear depth inversion." *Coastal Enginnering 55* (2008): 93-111.

Crawford, D.R., Lake, B.M, Saffmann, P.G., Yuen, H.C. "Effects of nonlinearity and spectral bandwidth on the dispersion relation and component phase speeds of surface gravity waves." *Fluid Mechanics, 112* (1981): 1-32.

Dugan, J.P., Piotrowski, C.C., Williams, J.Z.,. "Water depth and surface current retrievals from airborne optical measurements of surface gravity wave dispersion." *Journal of Geophysical research* (2001): 903-915.

Gavin, H.,. "The Levenberg - Marquardt method for nonlinear least squares curving problems." 2013.

Grilli, S.T., Skourup, J. "Depth Inversion for nonlinear waves shoaling over a barred beach." *26th Conference on Coatsal Engineering*. 1998. 603-616.

Guo, J. "Simple and explicit solution of wave dispersion equation." *Coastal Engineering (45)* (2002): 71-74.

Hedges, T.S.,. "An empirical modification to linear theory." *Institution of Civil Enginners, 51* (1976): 575-579.

Hoefel, F., Elgar, S. "Wave - induced sediment transport and sandbar migration." *Science* (2003): 1855-1856.

Holland, K.T., Holman, R. "Wavenumber - frequency structure of infragravity swash motions." *Journal of Geophysical Research 104* (1999): 13479 - 13488.

Holland, K.T., Holman, R., Lippmann, T,C., Stanley, J., Plant, N. "Practical use of video imagery in nearshore oceanographic field studies." *IEEE, Journal of oceanic engineering* (1997): 81-92.

Holland, T.,. "Application of the linear dispersion relationship with respect todepth inversion and remotely sensed imagery." *IEEE, transactions on geosciense and remote sensing, vol 39* (2001): 2060-2072.

Holman, R., Holland, T., Haller, M.,. "cBathy: a robust algorithm for estimation of nearshore bathymetry." *Journal of geophysical research: Oceans* (2013): 1-15.

Holman, R., Stanley, J. "The technical capabilities of Argus." (n.d.).

Kalman, R. "A new approach to linear filtering and prediction problems." *Basic Enginnering, 82* (1960): 35-45.

Kirby, J.T., Dalrymple, R.A.,. "An approximate model for nonlinear dispersion in monochromatic wave propagation models." *Coastal Engineering, vol 9* (545-561).

Lippmann, T.C., Holman, R. "Quantification of sand bar morphology: A video technique based on wave dissipation." *Geophysical Research, vol 94* (1989): 995-1011.

Plant N.G., Holland, K.T., Puleo, J.A.,. "Analysis of the scale of errors in nearhore bathymetric data." *Marine Geology, 191* (2002): 71 - 86.

Plant, G.N., Edwards, K.L., Kaihatu, J.M., Veeramony, J., Hsu, L., Holland, T. "The effect of bathymetric filtering on nearshore process model results." *Coastal Enginnering, 54* (2009): 484-493.

Plant, N.,G., Holland, T., Haller, M.,. "Ocean wavenumber estimations from wave-resolving time series imagery." *IEEE, Transcaction on geosciense and remote sensing, vol. 46* (2008): 2644-2658.

Ruessink, B.G., Kuriyama, Y., Reniers, A.J.H.M., Roelvink, J.A., Walstra, D.J.R. "Modeling cross shore sandbar behavior on the timescale of weeks." *Journal of Geophysical Research, vol 112* (2007): 1-15.

Schaffer, H.A., Madsen, P.A., Deigaard, R.,. "A Boussinesq wave model for waves breaking in the shallow water." *Coastal Engineering 20* (1993): 185 - 202.

Stive, M.J.F.,. "Energy dissipation in wave breaking on gentle slopes." *17th International Conference on Coastal Engineering*. 1980. 99-127.

Stockdon, H.,F., Holman, R.,. "Estimation of wave phase speed and nearshore bathymetry from video imagery." *Journal of Geophysical Research, vol 105* (2000): 22,015 - 22,033 .

Svendsen, I.A. *Introduction to nearshore hydrodynamics*. N. J.: World Sci., 2006. Advanced series of Ocean Enginnering, 24.

Svendsen, I.A., Madesen, P.A., Hansen, B. "Wave characteristics in the surf zone." *16th International Conference on Coastal Engineering*. 1978. 520-539.

Svendsen, I.A., Qin, W., Ebersole, B.A. "Modeling waves at the LSTF and other laboratories facilities." *Coastal Engineering, vol 50* (2003): 19-45.

Thornton, E.B., Guza, R.,T.,. "Energy saturation and phase speeds measured on a natural beach." *Journal of Geophysical Research* (1982): 9499-9508.

Tissier, M., Bonneton, P., Almar, R., Castelle, B., Bonneton, N., Nahon, N. "Field measurements and non-linear prediction of wave celerity in the surf zone." *European Journal of Mechanics B/Fluids* (2011): 635-641.

van Dongeren, A., van Ormondt, M., Cohen, A., Roelvink, D., Haller, M., Catalan, P. "Nearshore bathymetry assimilation through assimilation of model computations and remote observations." *Coastal dynamics, vol 55* (2008): 1016-1027.

van Ormondt, M., van Dongeren, A., Briere, C., Sembiring, L., Winter, G., Lescinski, J., Swinkels, C.,. "Simulating storm impacts and coastal floodings along the Netherlands." *Coastal flood risk* (2012).

Wallace, M.,J., Dickinson, E., R. "Empirical Orthogonal Representation of time series in the frequency domain. Part I: theoretical considerations." *Journal of applied meteorology* (1972): 887-892.

Wengrove, M., E., Henriquez, M., de Schipper , M., Holman R., Stive, M.J.F.,. "Monitoring morphology of the sand engine lee side using Argus' cBathy." *Coastal Dynamics*. Bordeaux, 2013. 1893-1904.

Yoo, J. "Nonlinear bathymetry inversion based wave property estimation based on nearshore video imagery." Phd Thesis. 2007.

Appendix

A.1. cBathy at y = -280 m

In the first of the Appendix the hourly results of each cBathy hourly run during high tide are shown at the longshore location y= -280 and for the last 350 m onshore. In addition to the bathymetric predictions, the cross shore profiles of the estimated wave celerity profile and pixel intensity are also included in order to investigate if the depth overestimation due to the onset of breaking occurs also during other times. The value of celerity in each cross shore position is estimated as the average of the wave celerity returned by phase 1 for each tile and using only estimates with skill and lamda above the threshold values. Runs with very high uncertainty returned are not shown.

Each tile extends 20 m landward and seaward of the analysis point so that wave phase speed is estimated using pixel information from a 40 m cross shore range. Therefore, instead of correlating the bathymetric error with the gradient of pixel intensity just at the cross shore location of the analysis point, it is more appropriate to look at its evolution for the total size of the tile. For example, for assessing the estimates at x = 80 m, the values of intensity should be checked for x between 60-100 m.

For the majority of the figures, a sudden drop in the bathymetric predictions corresponds to an increasing gradient in the pixel intensity profile. Usually, this location is around 80 m, in accordance with the results for the 2 hourly runs that were closely examined. This local drop is apparent especially in Figures A.4, A.5, A.9. Although celerity profiles have gaps in all four figures, a local peak can be seen at Figures A.4 – A.5 manifesting that the reasons of depth overprediction are locally controlled. The gaps indicate that depth estimation in those tiles was based only on adjacent locations. Pixel intensity did not differ significantly between adjacent tiles of the same cross shore position, thus celerity estimation there has been affected by the increase of intensity similarly to the longshore location -280 m. For time periods with low waves when wave breaking started more onshore, the same drop in bathymetry and increase in intensity is observed but shifted landward (Figures A.10 – A.12), manifesting further that anomalies in bathymetry are related with the initiation of breaking.

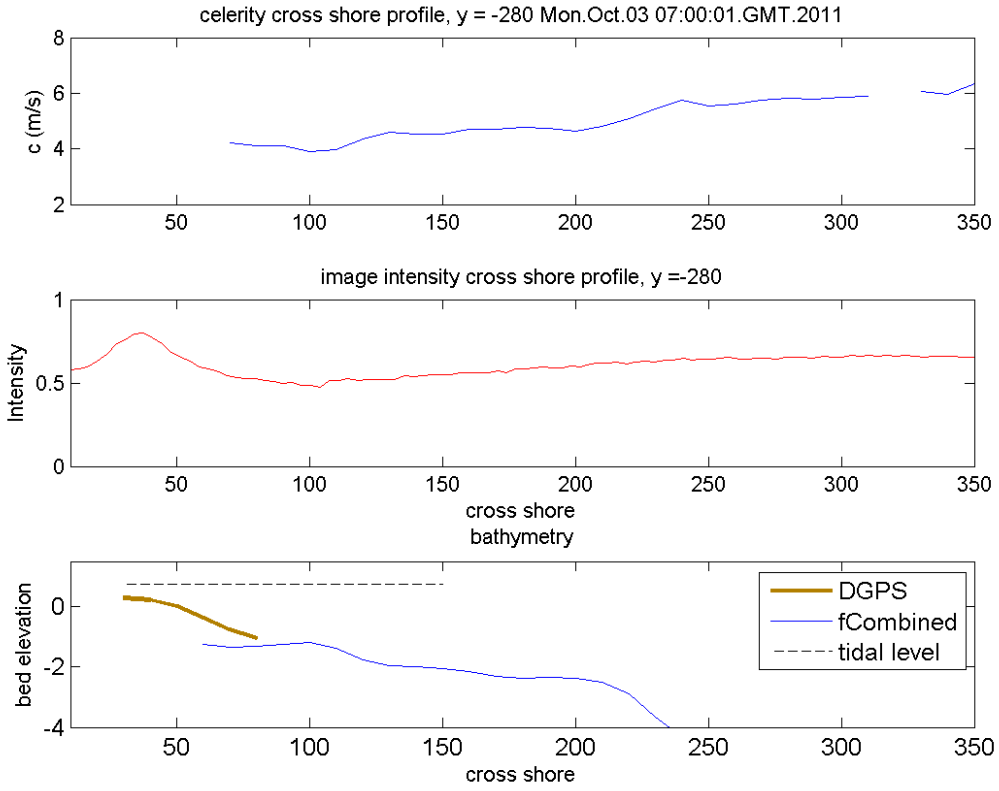

Figure A.1. cBathy, October 03, 07:00:00 GMT

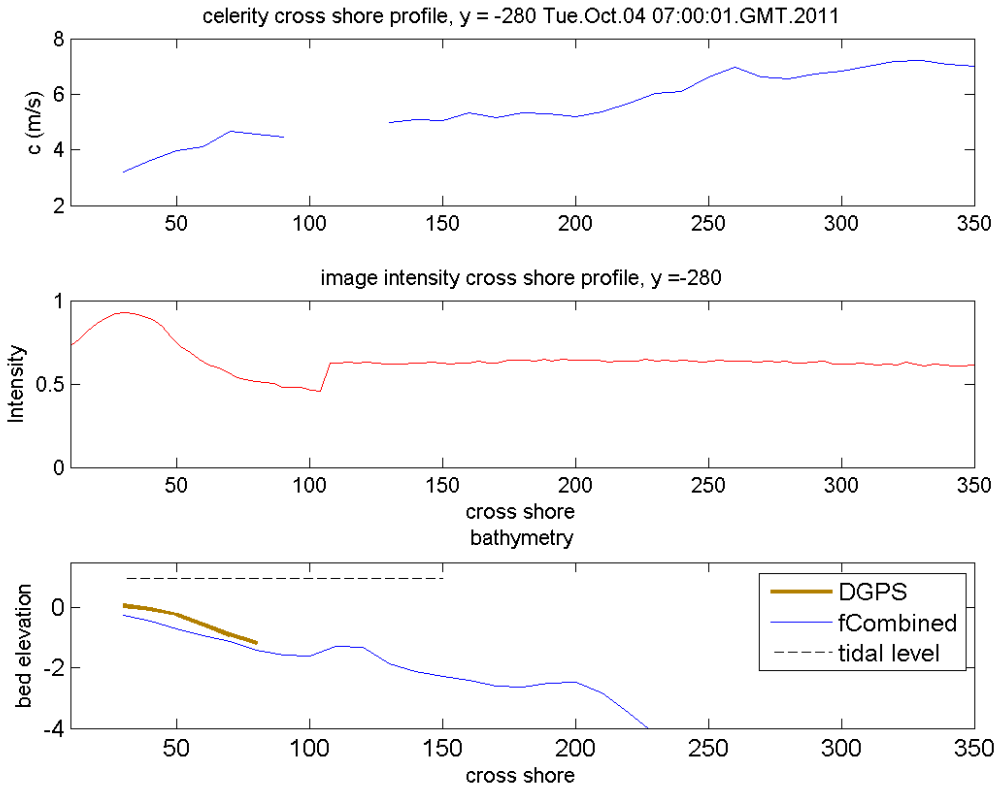

Figure A.2. cBathy, October 04, 07:00:00 GMT

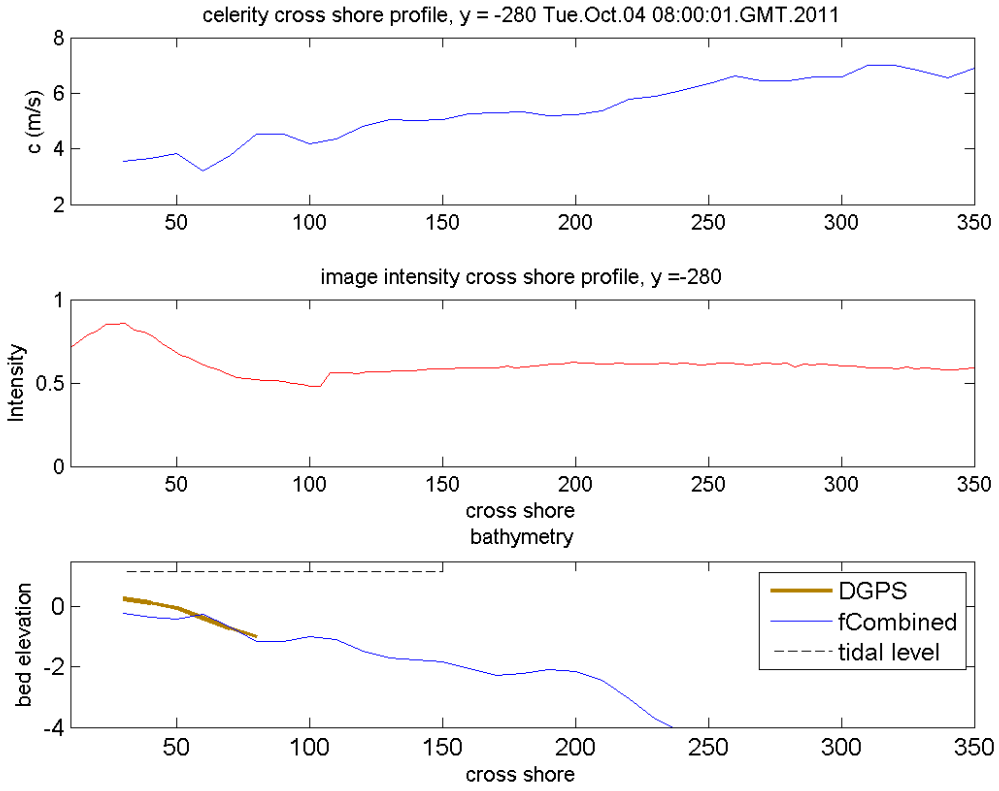

Figure A.3. cBathy, October 04, 08:00:00 GMT

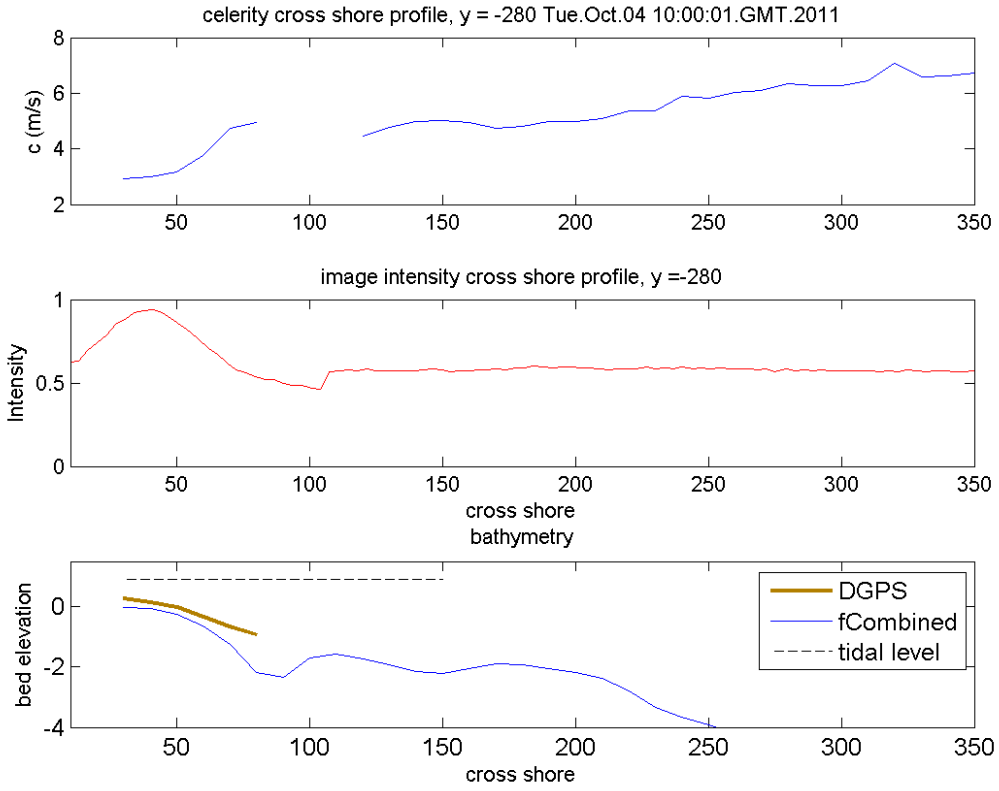

Figure A.4. cBathy, October 04, 10:00:00 GMT

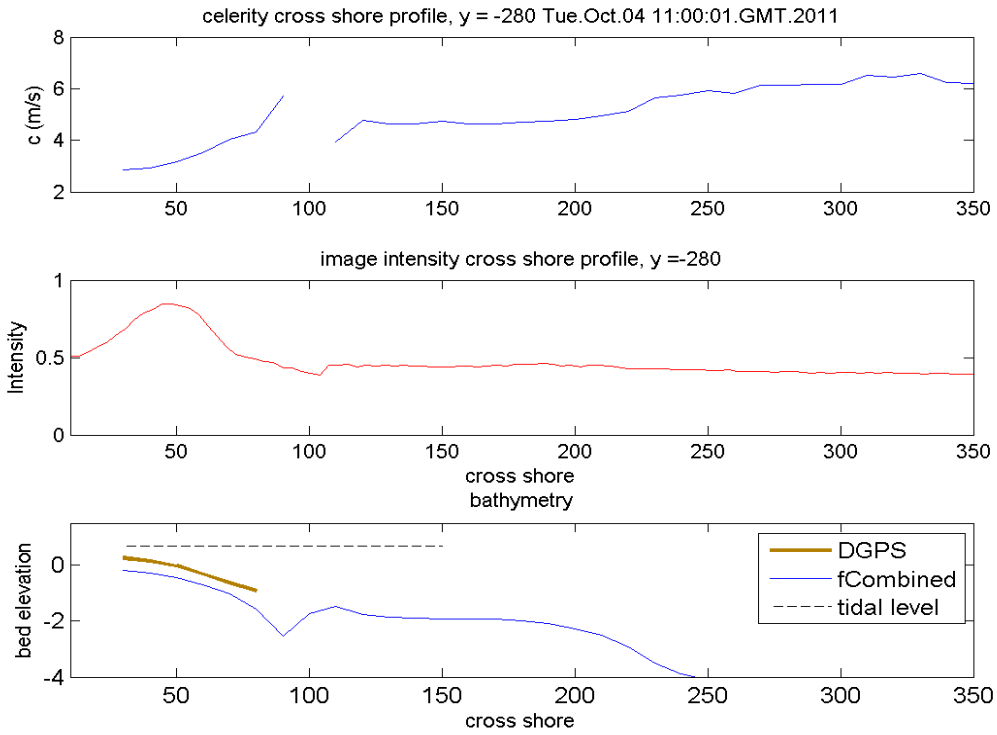

Figure A.5. cBathy, October 04, 11:00:00 GMT

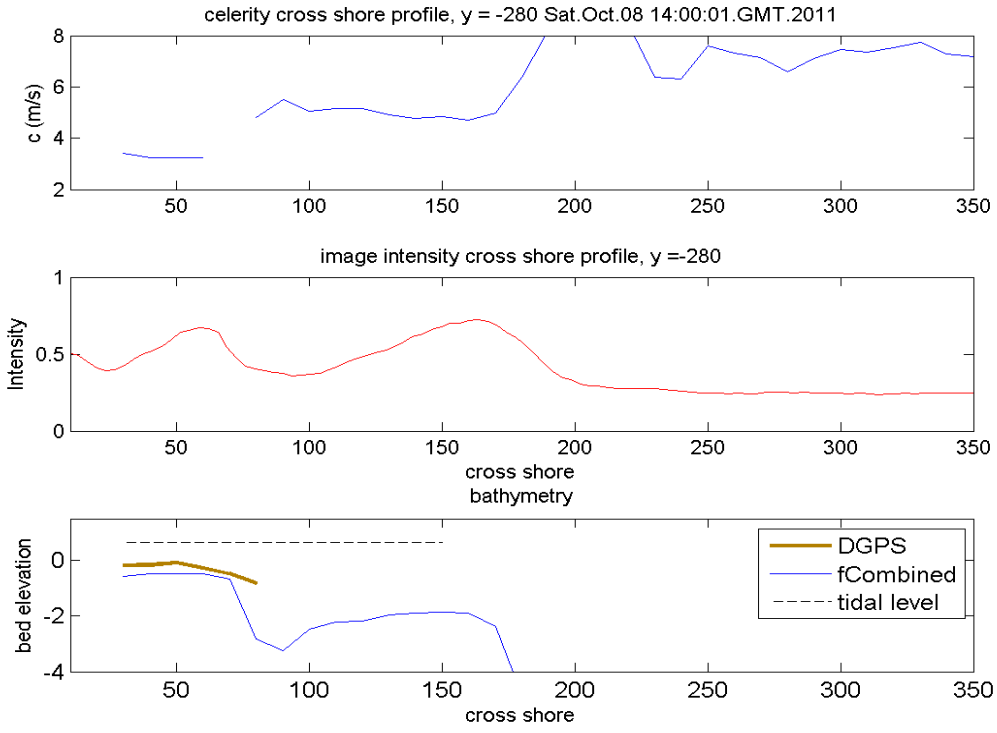

Figure A.6. cBathy, October 08, 14:00:00 GMT

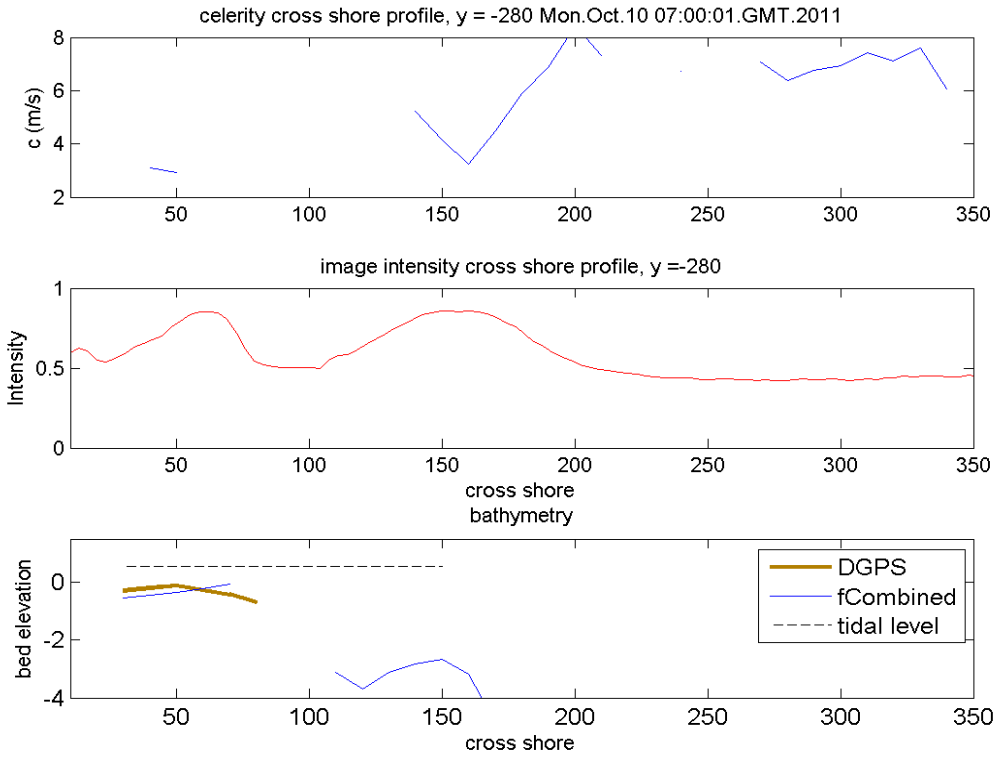

Figure A.7. cBathy, October 10, 07:00:00 GMT

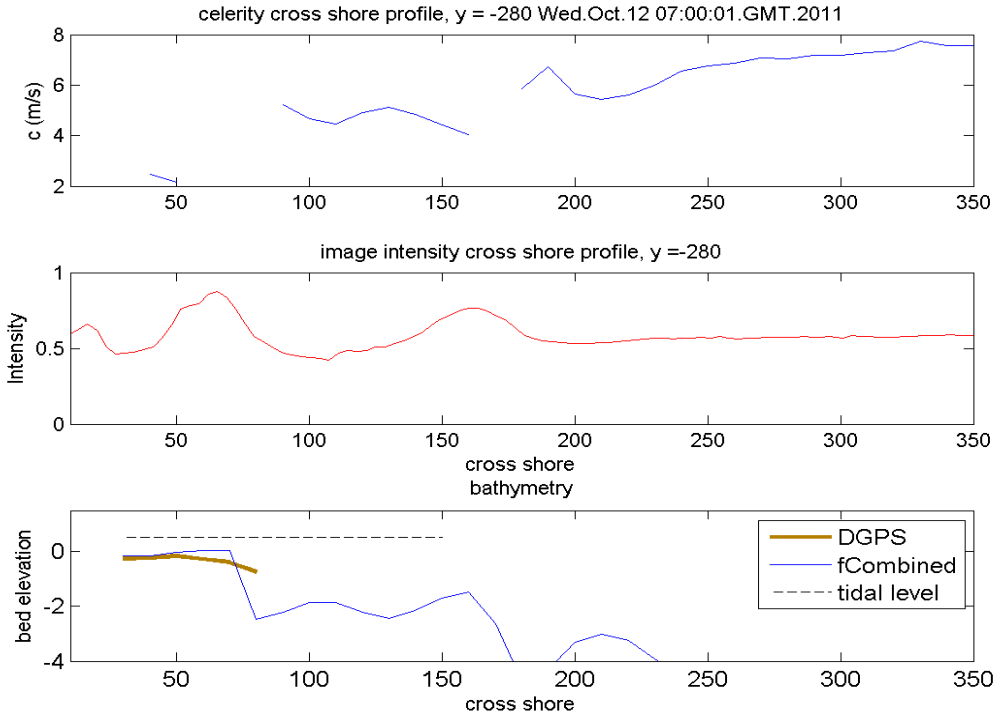

Figure A.8. cBathy, October 12, 07:00:00 GMT

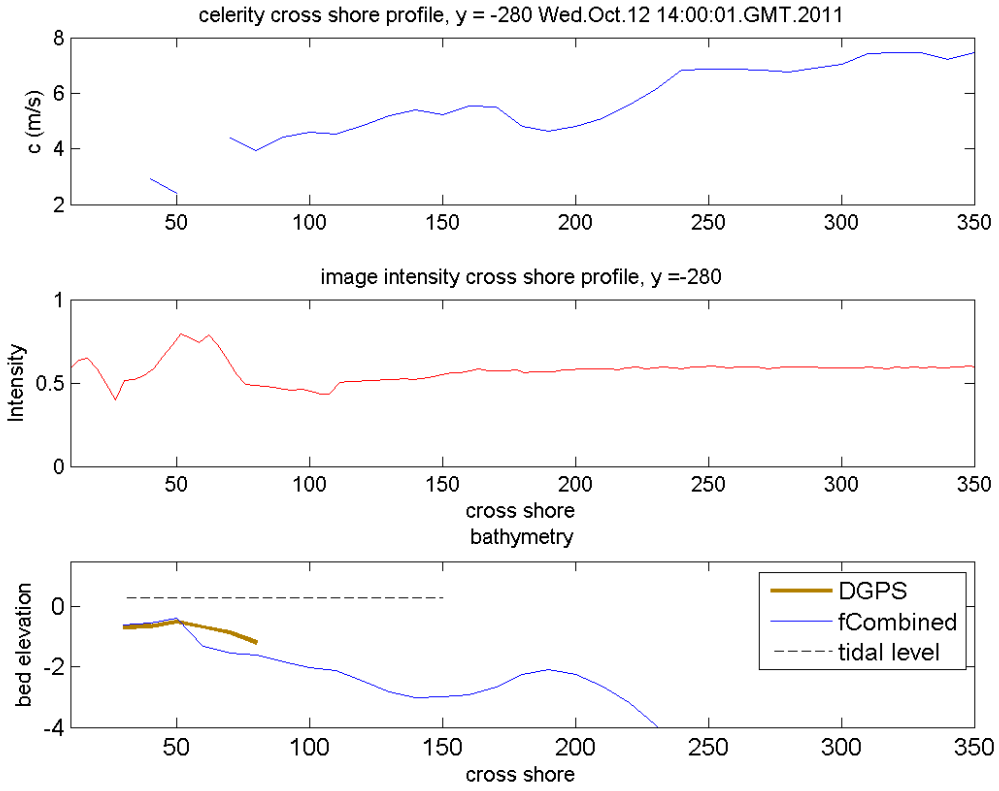

Figure A.9. cBathy, October 12, 14:00:00 GMT

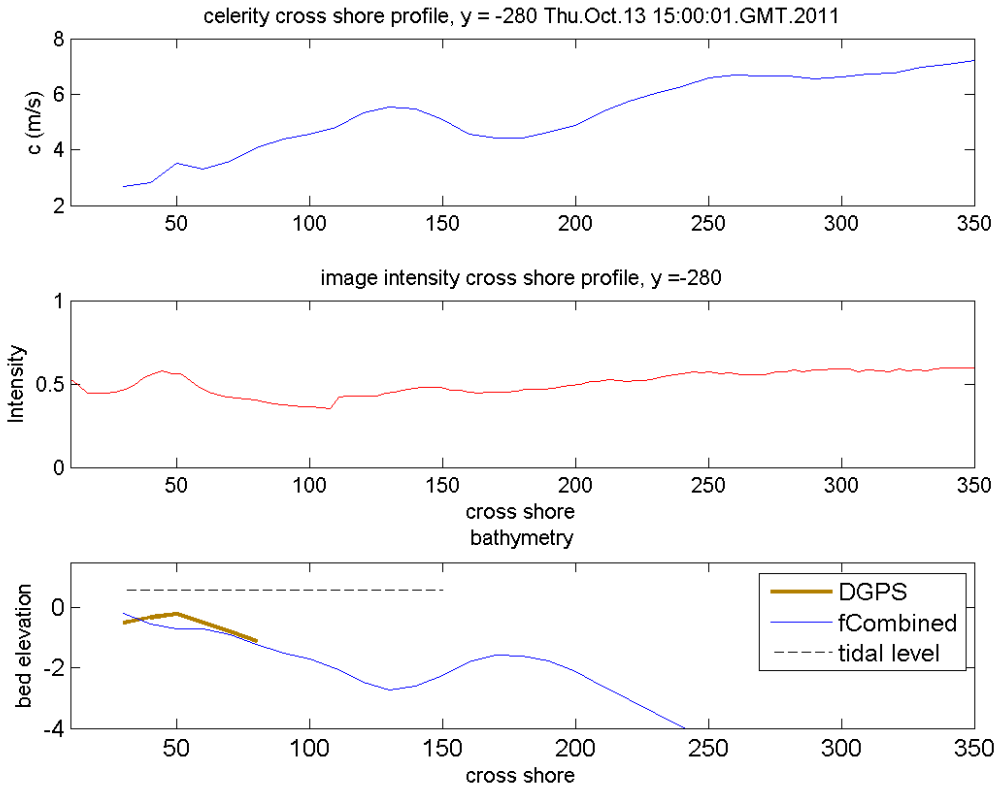

Figure A.10. cBathy, October 13, 15:00:00 GMT

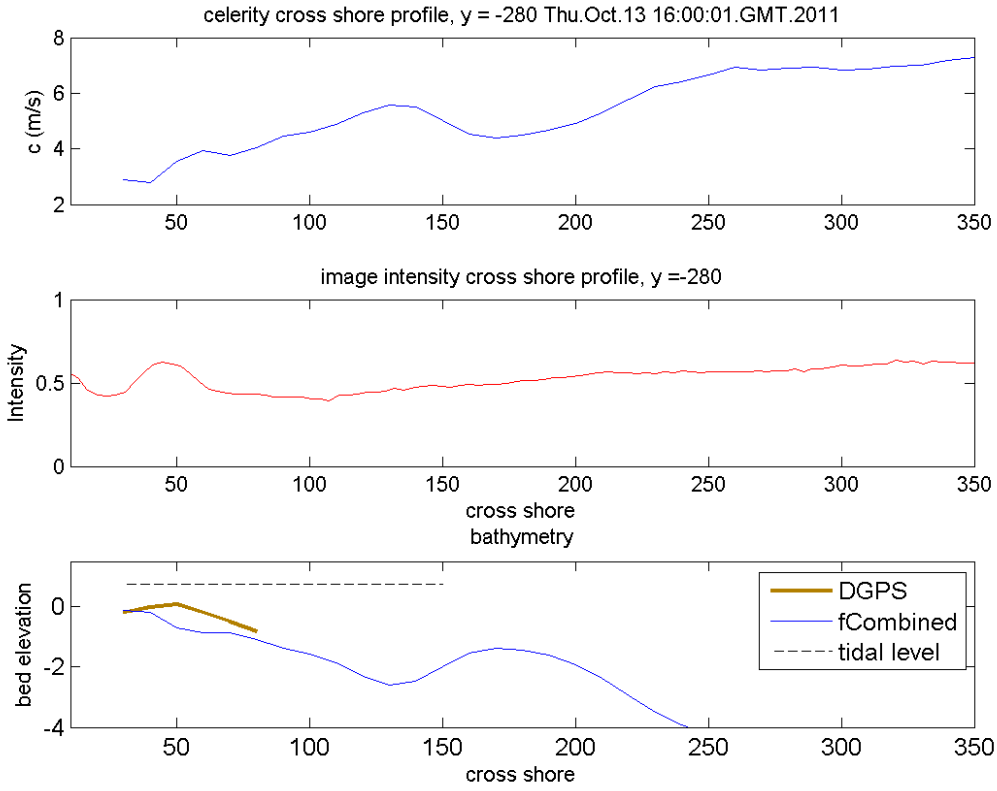

Figure A.11. cBathy, October 13, 16:00:00 GMT

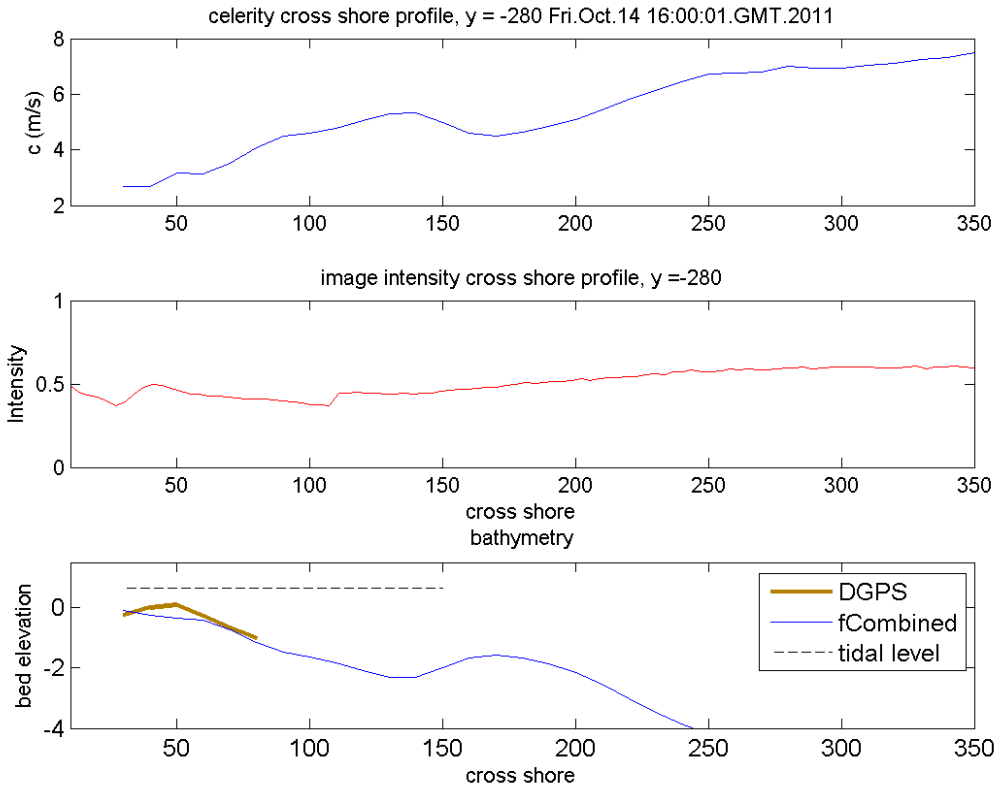

Figure A.12. cBathy October 14, 16:00:00 GMT

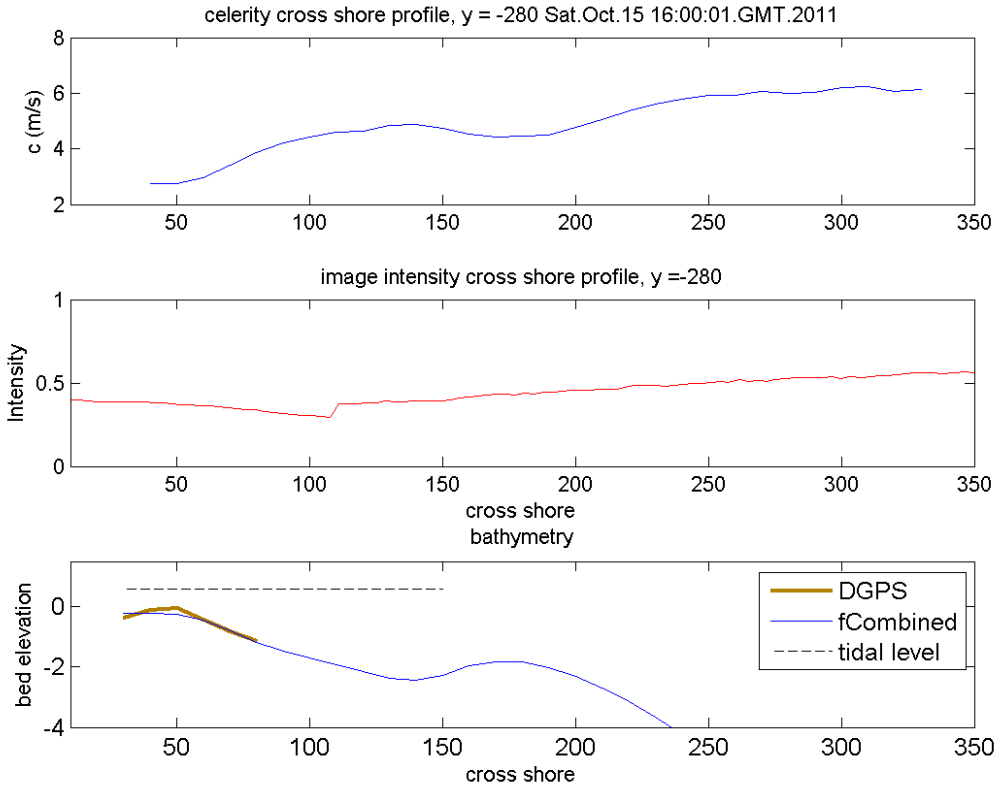

Figure A.13. cBathy, October 15, 16:00:00 GMT

A.2. cBathy at other longshore locations

In order to investigate if the anomalies in depth estimation around 80 m are related with the onset of breaking, the cBathy results of 4 October 09:00:00 GMT and 5 October 09:00:00 GMT are examined also for other longshore locations, y = -500 m, - 440 m, -360 m, -120 m. Similarly to A.1 profiles of celerity and pixel intensity are also plotted. Because surveyed bathymetric data were rather sparse for these two days, a bathymetry measured at 9 October is plotted against the cBathy results. The three days in between were quite stormy and thus the measured profile is used only as a reference.

At the 4th of October, 09:00:00 GMT, depth overprediction is apparent at all longshore locations (Figure A.14 - Figure A.16) around x = 80 m, except of Figure A.17 where it has been shifted more onshore. Peaks of the celerity profile are well pronounced at the same location for positions with no celerity gaps (Figure A.14 and Figure A.17) while the intensity of the pixels contained inside the corresponding tiles is also increased. The second day, the drop in the bathymetry is initiated around 120 m at the three first longshore positions (Figure A.18 - Figure A.20) except of the last position y = -120 m where the drop starts around x = 170 m and remains relatively constant for more than 100 m. Celerity appears again to obtain peaks at the same locations but no clear relationship with the intensity gradient can be observed so that the overprediction of celerity cannot safely be attributed to the onset of breaking. However, the tiles that lie at x = 100 m -120 m lie in cameras intersection only at y = -120 m. Thus, the problem related with the camera seam does not have an impact in the other locations inside the intertidal zone.

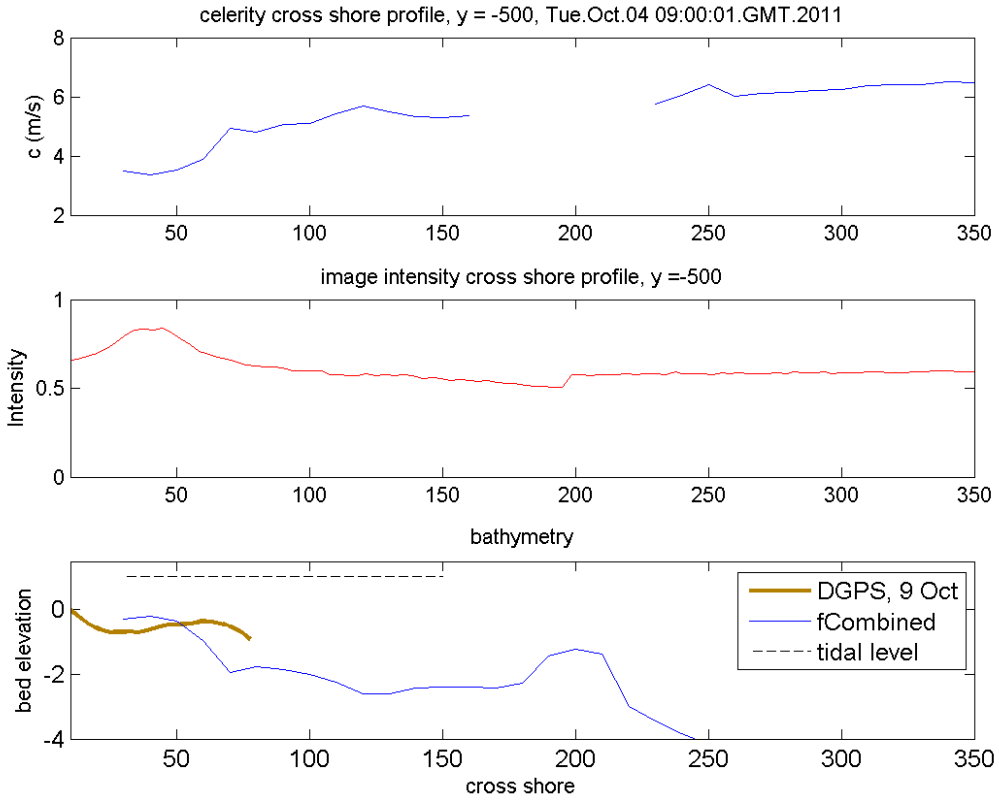

Figure A.14. cBathy, y = -500 m, 4 October 09:00:00 GMT.

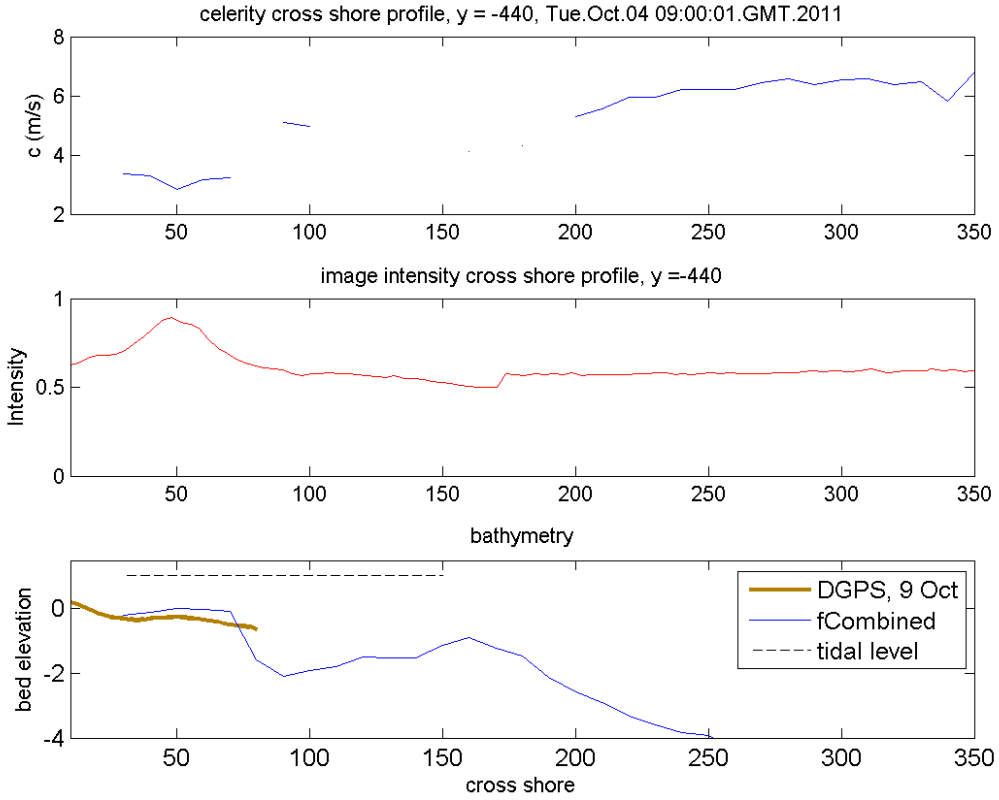

Figure A.15. cBathy, y = -440 m, 4 October 09:00:00 GMT.

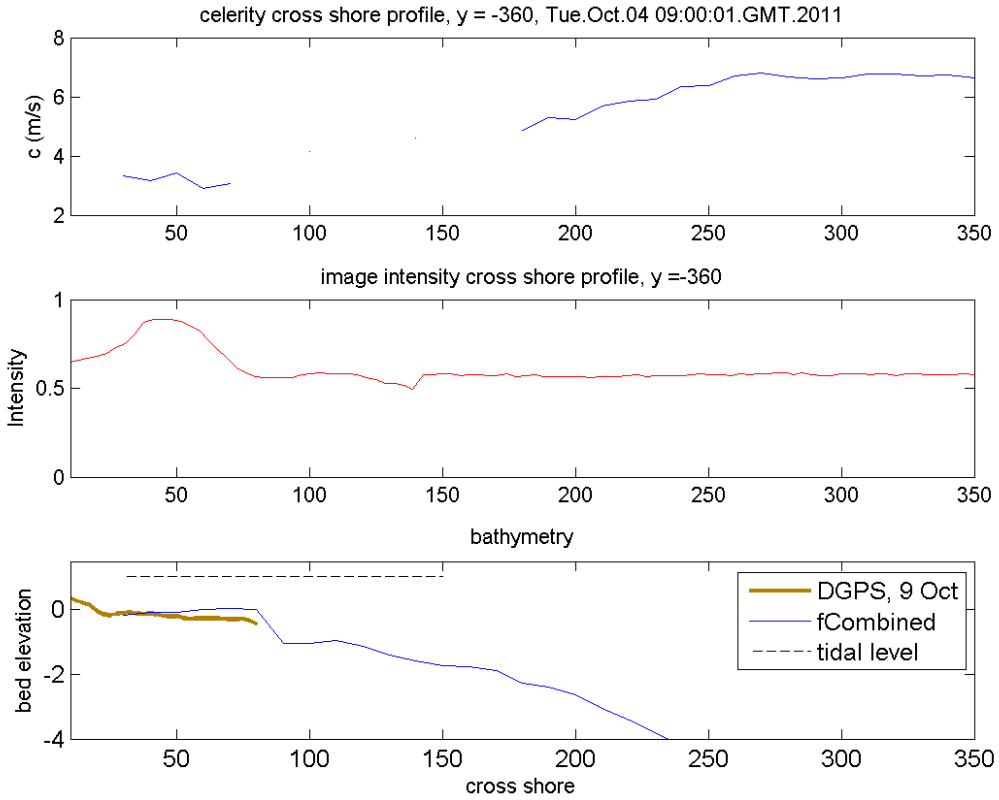

Figure A.16. cBathy, y = -360 m, 4 October 09:00:00 GMT.

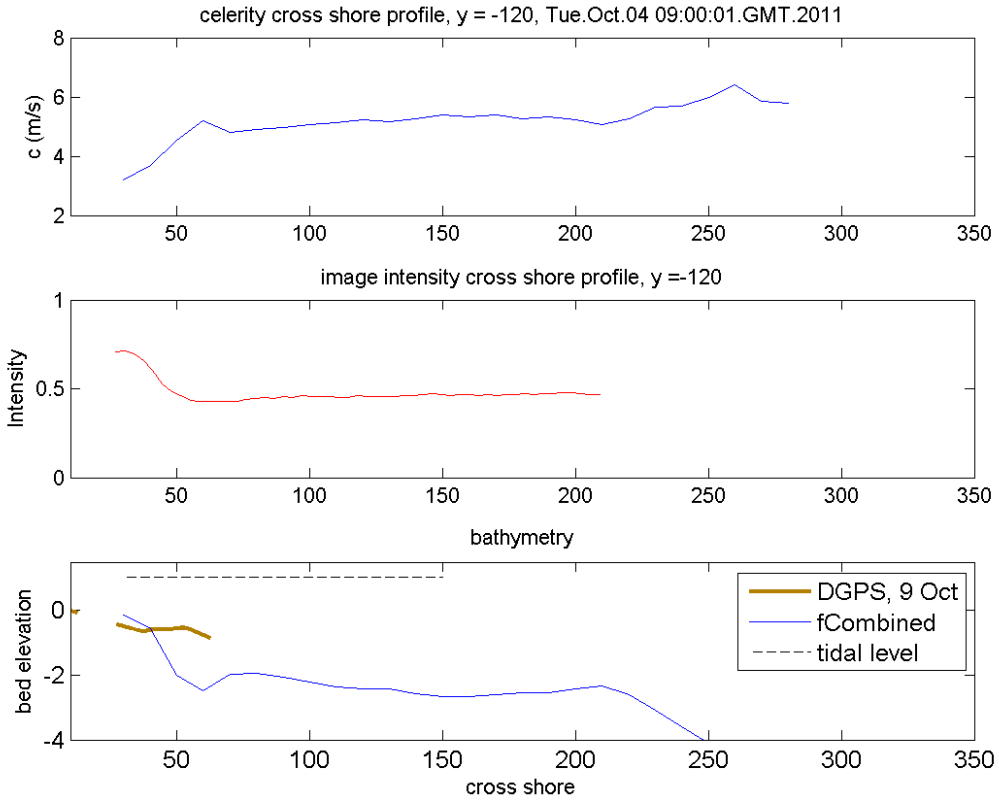

Figure A.17. cBathy, y = -120 m, 4 October 09:00:00 GMT.

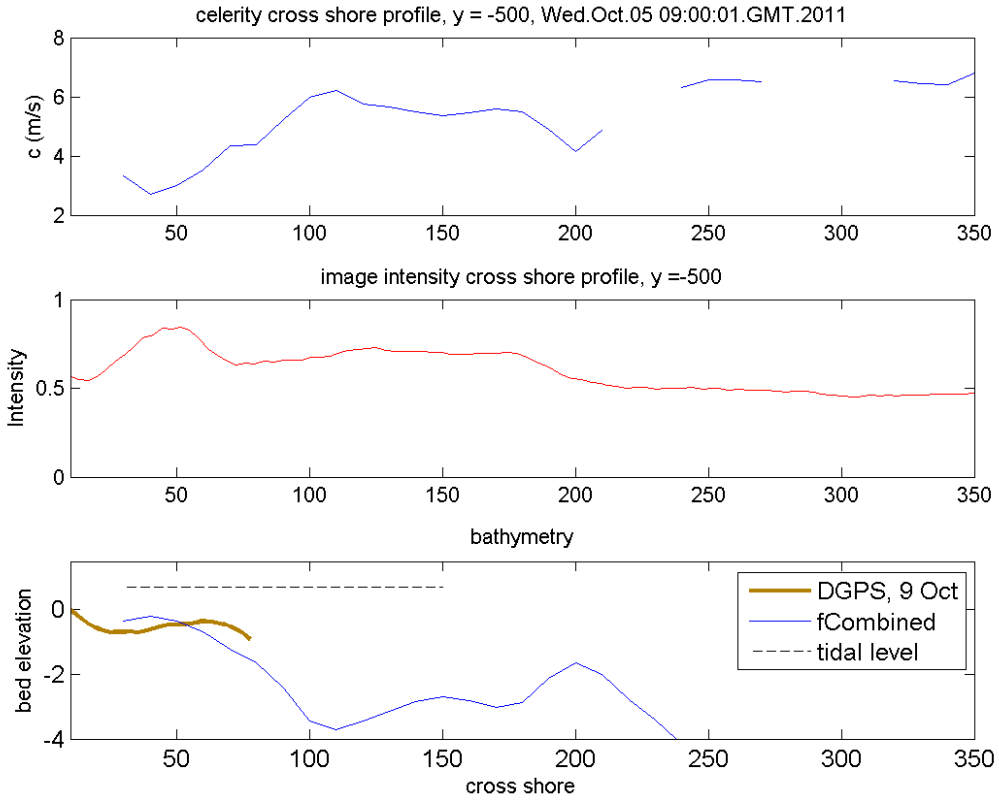

Figure A.18. cBathy, y = -500 m, 5 October 09:00:00 GMT.

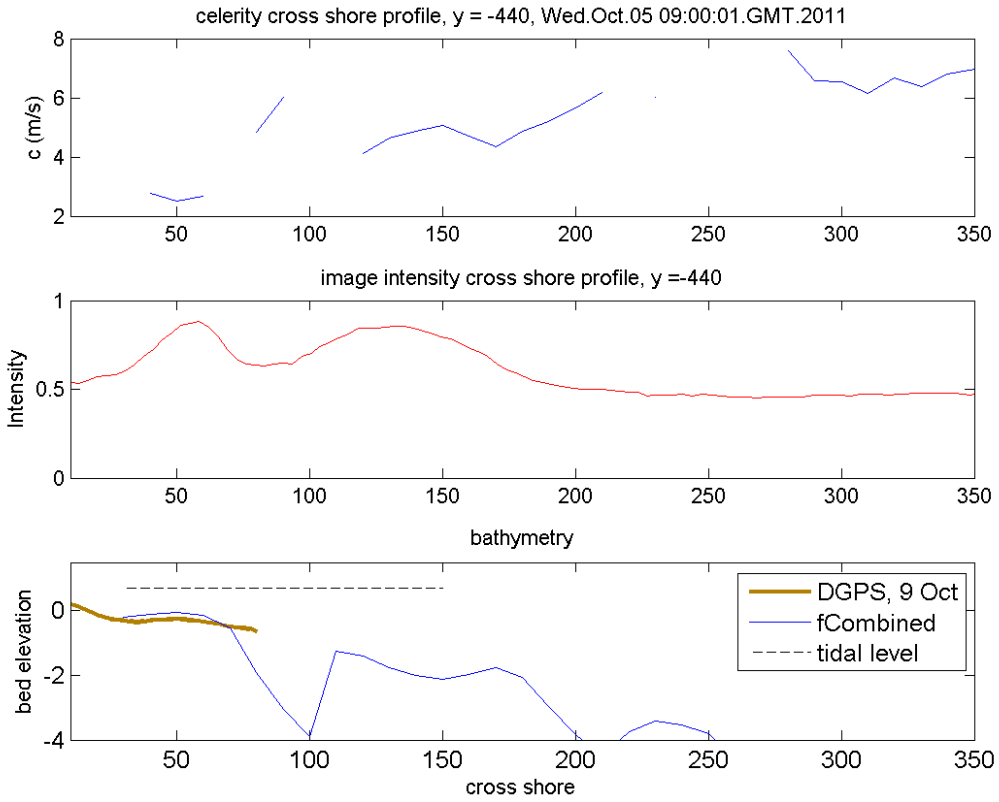

Figure A.19. cBathy, y = -440 m, 5 October 09:00:00 GMT.

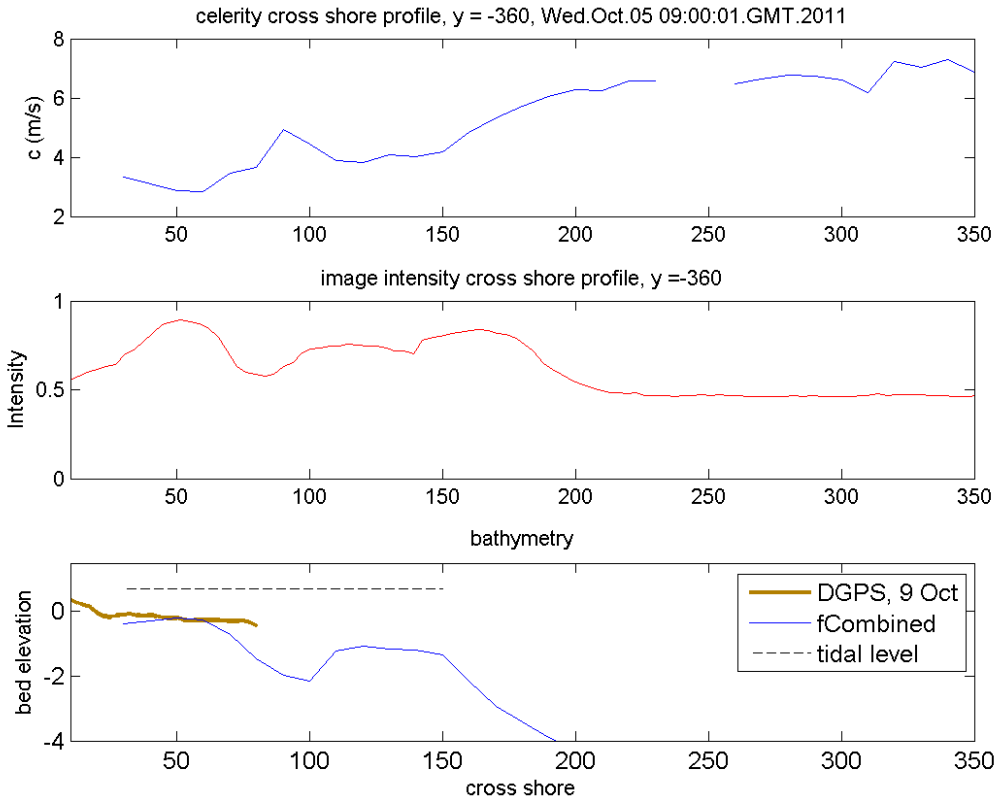

Figure A.20. cBathy, y = -360 m, 5 October 09:00:00 GMT.

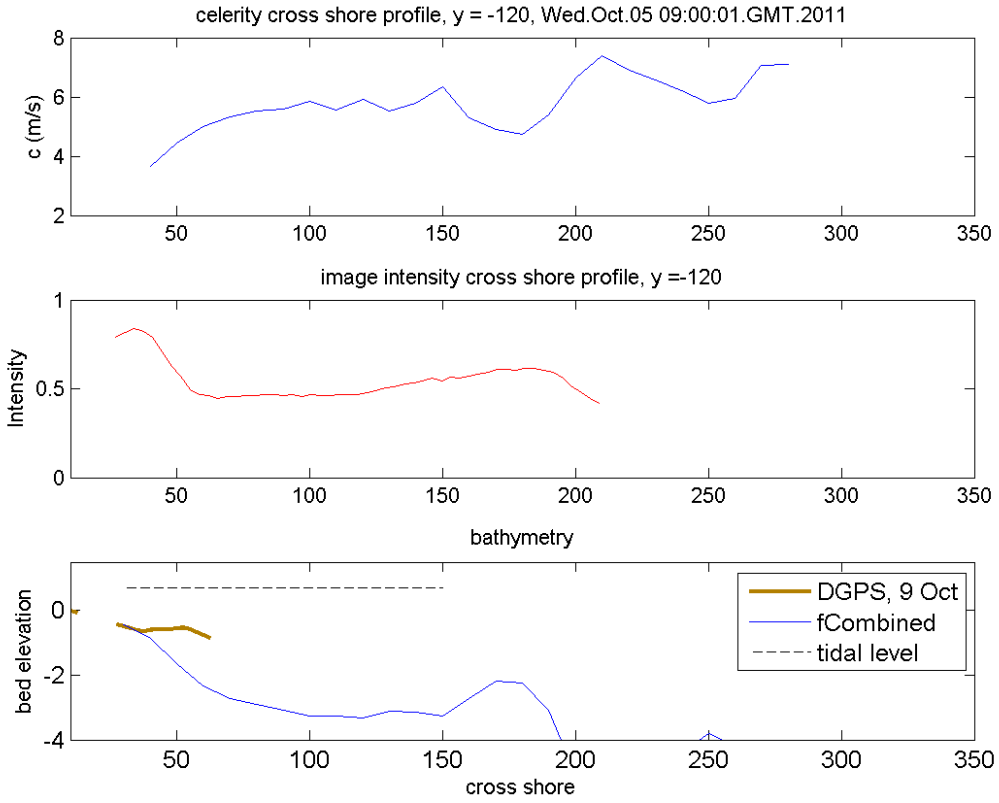

Figure A.21. cBathy, y = -120 m, 5 October 09:00:00 GMT.